Statistical Methods for the Interpretation of Recent Results in Neutrino Physics

von

Stefan Schoppmann

Diplomarbeit in Mathematik

vorgelegt der

Fakultät für Mathematik, Informatik und Naturwissenschaften der RWTH Aachen

im September 2012

angefertigt im

Institut für Statistik und Wirtschaftsmathematik
III. Physikalischen Institut B

bei

Univ.-Prof. Dr. rer. nat. Erhard Cramer
Univ.-Prof. Dr. rer. nat. Achim Stahl

communicated by Univ.-Prof. Dr. rer. nat. Erhard Cramer

Statistical Methods for the Interpretation of Recent Results in Neutrino Physics

Neutrino oscillations have become a well established phenomenon in particle physics during the past years. Recently the last unknown neutrino mixing angle has been measured to be non-zero. This has been done independently by experiments of two different concepts. In both cases special statistical methods are utilised to address the problem of small signal rates compared with large backgrounds. The analysis methods of the Double Chooz experiment, an experiment of the reactor concept, and the T2K experiment, an experiment of the accelerator concept, are investigated and underlying statistical concepts are prepared in a mathematically closed form. Furthermore, statistical methods for the combination of both results are developed. Special focus is set on methods to address the remaining, yet unknown, oscillation parameter δ_{CP} and the neutrino mass hierarchy.

Statistische Verfahren zur Interpretation aktueller Resultate aus der Neutrinophysik

Das Phänomen der Neutrinooszillation ist in den letzen Jahren zu einem fest etablierten Teilgebiet innerhalb der Teilchenphysik geworden. Kürzlich gelang es den letzten unbekannten Neutrinomischungswinkel als nicht verschwindend zu messen. Diese Messung wurde unabhänging mit verschiedenen experimentellen Konzepten durchgeführt. In beiden Experimenten wurden spezielle statistische Verfahren angewendet, um das Problem der geringen Signalrate im Vergleich zur Untergrundrate zu handhaben. Die Verfahren des Double Chooz Experiments, eines Reaktorexperiments, und des T2K Experiments, eines Beschleuningerexperiments, werden untersucht und die zugrunde liegenden statistischen Verfahren in mathematisch geschlossener Form aufbereitet. Weiterhin wird ein Verfahren zur Vereinigung beider Ergebnisse erarbeitet. Besonderes Augenmerk liegt dabei auf der Bestimmung des verbleibenden unbekannten Oszillationsparameters δ_{CP} und der Neutrinomassenhierarchie.

Contents

Chapter 1

Introduction

Although known for several years, neutrino oscillations have been subject of increased efforts until the present date [1; 2; 3; 4; 5; 6]. Due to the smallness of one of the three mixing angles, this last mixing angle θ_{13} was determined not before 2011 [7; 8]. Further experiments were able to measure this angle in 2012 [9; 10]. These experiments are expected to deliver further and more precise results in the future. With the determination of θ_{13} the possibility opens to infer on the charge-parity violation phase δ_{CP}. This parameter describes the different behaviour of neutrinos and antineutrinos in the context of neutrino oscillations. Furthermore, the neutrino mass hierarchy can be addressed. The question for the neutrino mass hierarchy is the question if two neutrino masses are very small compared to the third one or very large.

One idea for the investigation of these parameters is the combination of measurements from different experiment types. An accelerator experiment, when aiming for a θ_{13} measurement, always measures a combination of θ_{13}, δ_{CP} and the mass hierarchy; in contrast to this measures a reactor experiment θ_{13} directly. This can be utilised to render the combination of such two experiments sensitive to δ_{CP} or the mass hierarchy. Since both experiment types deal with rather small signals compared to their backgrounds, a thorough understanding of the analysis techniques and their correlations, especially the correlations between the experiments, are crucial for a significant inference.

In chapter 6, such a combination scenario will be investigated using the Double Chooz and the T2K experiment as concrete representatives of the respective experiment types. Chapter 3 introduces these experiments in a general matter. Both experiments employ special techniques to deal with the issue of large backgrounds which are investigated with special focus lying on the statistical methods in chapter 5 and resumed in the combination scenario. The related theory of these methods is the topic of chapter 4, while the theory necessary for the understanding of the combination idea and the phenomenon of neutrino oscillations is given in chapter 2. After developing a combination scenario a conclusion and outlook will be given in chapter 7.

Chapter 2

Theory of Neutrino Oscillations

This thesis deals with recent results from neutrino physics. Hence, the following chapter introduces the theory of neutrino oscillations.

2.1 The Neutrinos

The existence of neutrinos was postulated for the first time in the year 1933 when Wolfgang Pauli suggested the participation of an unknown particle in the β-decay in order to solve the measured violation of energy and angular momentum conservation [11, p. 119]. The suggested particle must be free of electrical charge and interacts only via the weak force and the force of gravity. In the year of 1956, the postulated particle was measured for the first time at the Savannah River Site nuclear power plant [12]. The particle was later called ν_e, the electron neutrino[1]. The measured cross-section of the discovered particle of $10^{-44}\,\mathrm{cm}^2$ [12, p. 104] and the mass of $< 2\,\mathrm{eV/c}^2$ [13, p. 555] were rather small. This explains the fact, why this particle was not recognised in the year of 1933 and confirms Pauli's postulation.

In the year 1962 the existence of a second type of neutrino, the muon neutrino ν_μ, was discovered at the **A**lternating **G**radient **S**ynchrotron (AGS) at the Brookhaven National Laboratory [14]. A third neutrino type, called tauon neutrino ν_τ, was discovered in 2001 at the Fermilab [15]. Data from the **L**arge **E**lectron-**P**ositron Collider (LEP) [13, p. 561] yield towards the existence of precisely the three discovered neutrino generations. By these results, neutrinos have the same number of generations as other types of elementary particles and confirm the standard model of elementary particles.

2.2 Neutrino Oscillations

While the discoveries of the three neutrino generations confirmed the standard model, several discoveries [1; 2; 3; 4; 5; 6] made an extension to the standard model necessary:

The effect of neutrino oscillation was theorised for the first time by Bruno Pontecorvo [16]. In 1957 he discussed the possibility of the transformation between neutrinos and antineutrinos. Today, neutrino oscillation is understood as the transformation of neutrinos of a certain flavour into neutrinos of another flavour [17], e.g. muon neutrinos into electron neutrinos. Within the framework of quantum mechanics, this transformation is possible due to the inequality of the

[1] More precise, not the electron neutrino ν_e, but the electron antineutrino $\bar{\nu}_e$ was discovered in 1956.

neutrino eigenstates of energy and the neutrino eigenstates of the weak force. Mathematically, a neutrino has to be seen as a vector in a vector space [18, pp. 111–125]. In this vector space, two operators of our interest exist. To each operator three eigenvectors or eigenstates exist. One operator is the Hamilton operator and if a neutrino is in an eigenstate to this operator, i.e. its state is represented by an eigenvector of the Hamilton operator, the neutrino has a certain mass. The second operator is the flavour operator. If a neutrino is in an eigenstate to this operator, the neutrino has a certain flavour. The eigenvectors of the afore-mentioned operators make up two distinct orthonormal bases of the underlying vector space. The three flavour eigenstates or eigenvectors are labeled as electron neutrino $|\nu_e\rangle$, muon neutrino $|\nu_\mu\rangle$ and tauon neutrino $|\nu_\tau\rangle$ and build the first basis. The three mass eigenstates are labeled with integers: $|\nu_1\rangle$, $|\nu_2\rangle$ and $|\nu_3\rangle$. They build the second basis [19, p. 255]. The vector which represents the neutrino in this space $|\nu_x\rangle$ can be represented as a linear combination of the three basis vectors of both bases [13, p. 165]:

$$|\nu_x\rangle = \sum_{j=1}^{3} \alpha_j |\nu_j\rangle, \text{ with } j \in \{1,2,3\} \text{ and } |\nu_x\rangle = \sum_{\alpha=1}^{3} \beta_\alpha |\nu_\alpha\rangle, \text{ with } \alpha \in \{e,\mu,\tau\}. \tag{2.1}$$

It is possible to change between the two bases by applying a change of basis matrix. This matrix is called **P**ontecorvo-**M**aki-**N**akagawa-**S**akata-Matrix (PMNS) and is denoted as the U_{PMNS} [20, p. 2]. For this change of basis, one considers an arbitrary neutrino $|\nu_x\rangle$ as represented by its coordinate vector

$$(\alpha_1, \alpha_2, \alpha_3)^{\mathrm{T}} \tag{2.2}$$

and finds the coordinate vector of this neutrino $|\nu_x\rangle$ in the changed basis as[2]

$$(\beta_e, \beta_\mu, \beta_\tau)^{\mathrm{T}} = U^{\dagger}_{PMNS} \times (\alpha_1, \alpha_2, \alpha_3)^{\mathrm{T}}. \tag{2.3}$$

The principals of quantum mechanics require a neutrino $|\nu_x\rangle$ to be in a certain flavour eigenstate when created, e.g. $|\nu_x\rangle = |\nu_e\rangle$, since it is created in a weak interaction [18, p. 113]. On the other hand, while the neutrino propergates through space (as it would from a source to a detector) the time evolution of the neutrino's quantum state is generated by the Hamiltonian according to the Schrödinger equation and thus the mass eigenstates are present [19, p. 255]. Thus, in analogy to equation 2.3 the initial neutrino with certain flavour is now to be considered in the basis of mass eigenstates, hence:

$$|\nu_x\rangle = |\nu_\alpha\rangle = \sum_{j=1}^{3} U^{*}_{\alpha j} |\nu_j\rangle, \text{ with } \alpha \in \{e,\mu,\tau\}. \tag{2.4}$$

The time evolution according to the Schrödinger equation reads as

$$|\nu_j(t)\rangle = |\nu_j(0)\rangle e^{-i(Et-pz)}, \text{ with } j \in \{1,2,3\} \tag{2.5}$$

were t denotes the time from the creation, E the energy of the neutrino, p the momentum and z the position along the z-axis, while the neutrino is assumed to travel along this axis.

[2] The usage of the inverse $U^{\dagger}_{PMNS} = U^{-1}_{PMNS}$ instead of the unitary matrix U_{PMNS} itself is definition.

Utilising equation 2.4 we get the time evolution of the initial neutrino[3] as [13, p. 165]

$$|\nu_\alpha(t)\rangle = \sum_{j=1}^{3} U^*_{\alpha j}|\nu_j(0)\rangle e^{-i(Et-pz)}, \text{ with } \alpha \in \{e,\mu,\tau\}. \tag{2.6}$$

In equation 2.6, assuming ultrarelativistic neutrinos, the time can be substituted by the travel distance L ($c = 1$). By additionally Taylor expanding the energy to leading order in this equation and dropping the phase factors[4], one gets the good approximation of

$$|\nu_\alpha(L)\rangle = \sum_{j=1}^{3} U^*_{\alpha j}|\nu_j(0)\rangle e^{-im_j^2 L/(2E)}, \text{ with } \alpha \in \{e,\mu,\tau\}. \tag{2.7}$$

Due to different mass eigenvalues m_j, $j \in \{1,2,3\}$ of the three mass eigenstates, the time evolution of the three mass eigenstates is slightly different [19, p. 255]. This means that the neutrino $|\nu_\alpha(L)\rangle$ is in general no longer in an eigenstate for $L > 0$. One can see this directly from equation 2.7: for $L > 0$ the ratio of the three coefficients $U^*_{\alpha 1}e^{-im_1^2 L/(2E)}$ / $U^*_{\alpha 2}e^{-im_2^2 L/(2E)}$ / $U^*_{\alpha 3}e^{-im_3^2 L/(2E)}$ is different from the initial ratio for $L = 0$ and hence $|\nu_j(L=0)\rangle \neq |\nu_j(L>0)\rangle$ in general holds[5].

We assumed that the neutrino travels from a source to a detector. The detection works via the weak force, thus the neutrino has to have a certain flavour in this reaction. Thus it has to be in a certain flavour eigenstate. The theory of quantum mechanics dictates that the neutrino takes on a certain flavour eigenstate e.g. $|\nu_\beta\rangle$ with a probability equal to the square of the projection of its current state, e.g. $|\nu_\alpha(L)\rangle$, onto the certain flavour eigenstate $|\nu_\beta\rangle$ [18, p. 117]. Hence, the probability can be expressed as

$$P(\nu_\alpha \to \nu_\beta)(L) = |\langle\nu_\beta|\nu_\alpha(L)\rangle|^2, \text{ with } \alpha,\beta \in \{e,\mu,\tau\}, \tag{2.8}$$

where $\langle\nu_\beta| = |\nu_\beta\rangle^\dagger$ denotes the complex conjugate of $|\nu_\beta\rangle$. The term $\langle\nu_\beta|\nu_\alpha(L)\rangle$ is thus to be understood as a bilinear mapping $\langle\nu_\beta|(|\nu_\alpha(L)\rangle)$, in which $|\nu_\alpha(L)\rangle$ is an element of the original vector space and $\langle\nu_\beta|$ denotes the element of the dual space corresponding unambiguously to $|\nu_\beta\rangle$ by the Riez representation theorem. Equation 2.8 can be understood as the probability to measure the initial neutrino $|\nu_\alpha\rangle$ after a travel distance L as a neutrino of type $|\nu_\beta\rangle$. Applying equations 2.4 and 2.7 and keeping in mind that $\langle\nu_\beta| = |\nu_\beta\rangle^\dagger$, equation 2.8 read as

$$P(\nu_\alpha \to \nu_\beta)(L) = \left|\sum_{j=1}^{3} U_{\alpha j}U^*_{\beta j}e^{-im_j^2 L/(2E)}\right|^2. \tag{2.9}$$

This probability undergoes periodical changes with the travel time and travel distance, respectively. Figure 2.2 shows some of these probability graphs for the case of the Double Chooz and the T2K experiments.

In order to compute this probability, the actual representation of the PMNS matrix becomes important. The common representation utilises the notion of Euler angles and reads

[3] To be precise, the neutrino is in general no longer in a flavour eigenstate for $L > 0$ (see later) and should better be referred to as $|\nu_x(L)\rangle$, but as equation 2.6 describes the time evolution of the vector $|\nu_\alpha\rangle = |\nu_\alpha(L=0)\rangle$ the usage of $|\nu_\alpha(L)\rangle$ is mathematically correct.

[4] These factors are irrelevant in the later derived oscillation equation.

[5] More precisely it even holds in general that $|\nu_j(L=0)\rangle \neq \epsilon|\nu_j(L>0)\rangle$, $\epsilon \in \mathbb{R}$, i.e. $|\nu_j(L=0)\rangle$ and $|\nu_j(L>0)\rangle$ are in general not linear dependent. Only from this additional inequality follows that the neutrino is no longer in the initial eigenspace.

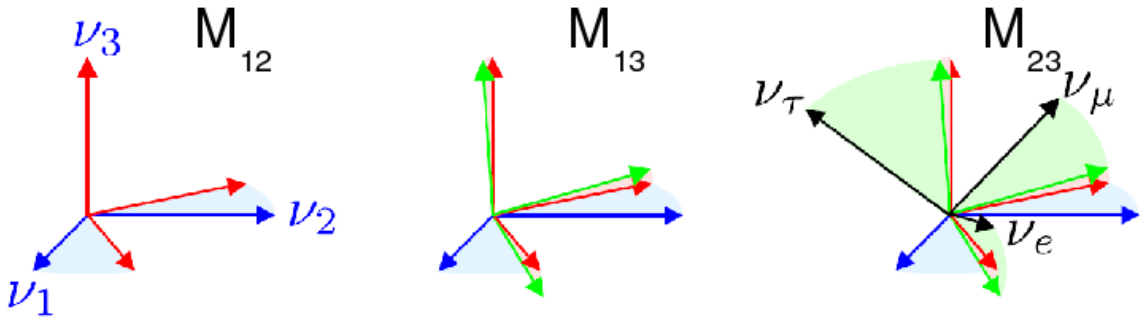

Figure 2.1: Change of basis between the basis of flavour eigenstates and the basis of mass eigenstates. The mixing angles are the Euler angles. The application of the submatrices in equation 2.10 corresponds to the figures from left to right. The angles are drawn approximately realistic. [21, p. 6]

[13, p. 179]

$$U_{PMNS} = \begin{pmatrix} c_{12}c_{13} & s_{12}c_{13} & s_{13}e^{-i\delta} \\ -s_{12}c_{23} - s_{13}s_{23}c_{12}e^{i\delta} & c_{12}c_{23} - s_{12}s_{13}s_{23}e^{i\delta} & s_{23}c_{13} \\ s_{12}s_{23} - s_{13}c_{12}c_{23}e^{i\delta} & -s_{23}c_{12} - s_{12}s_{13}c_{23}e^{i\delta} & c_{13}c_{23} \end{pmatrix} \times \begin{pmatrix} 1 & 0 & 0 \\ 0 & e^{i\alpha_1} & 0 \\ 0 & 0 & e^{i\alpha_2} \end{pmatrix}$$

$$= \begin{pmatrix} 1 & 0 & 0 \\ 0 & c_{23} & s_{23} \\ 0 & -s_{23} & c_{23} \end{pmatrix} \times \begin{pmatrix} c_{13} & 0 & s_{13}e^{-i\delta} \\ 0 & 1 & 0 \\ -s_{13}e^{i\delta} & 0 & c_{13} \end{pmatrix} \times \begin{pmatrix} c_{12} & s_{12} & 0 \\ -s_{12} & c_{12} & 0 \\ 0 & 0 & 1 \end{pmatrix} \times \begin{pmatrix} 1 & 0 & 0 \\ 0 & e^{i\alpha_1} & 0 \\ 0 & 0 & e^{i\alpha_2} \end{pmatrix}$$

$$\text{with } s_{kl} = \sin(\theta_{kl}) \text{ and } c_{mn} = \cos(\theta_{mn}). \tag{2.10}$$

The variables θ_{kl} represent the Euler angles as seen in figure 2.1 and $\delta = \delta_{CP}$ is the CP-violating phase. This accounts for different oscillation probabilities between neutrinos and antineutrinos [22, p. 36]. Its influence on the change of basis matrix can be seen in the mixture of flavour and mass eigenstates in figure 2.4. The variables α_j, $j \in \{1, 2\}$ are the Majorana phases and are only of importance if neutrinos are equal to antineutrinos [13, p. 179]. In our context these phases can be neglected since they are on the main diagonal of the PMNS matrix. With this representation and equation 2.9 together with the unitarity of the PMNS matrix one can compute the vacuum oscillation probabilities in leading order as [23, p. 97]

$$\begin{aligned} P(\bar{\nu}_e \to \bar{\nu}_e) = 1 &- 4\sin^2(\theta_{13})\cos^2(\theta_{13})\sin^2\left(\frac{\Delta m^2_{31} L}{4E}\right) \\ &- \cos^4(\theta_{13})\sin^2(2\theta_{12})\sin^2\left(\frac{\Delta m^2_{21} L}{4E}\right) \\ &+ 2\sin^2(\theta_{13})\cos^2(\theta_{13})\sin^2(\theta_{12})\left(\cos\left(\frac{\Delta m^2_{31} L}{2E} - \frac{\Delta m^2_{21} L}{2E}\right) - \cos\left(\frac{\Delta m^2_{31} L}{2E}\right)\right) \end{aligned} \tag{2.11}$$

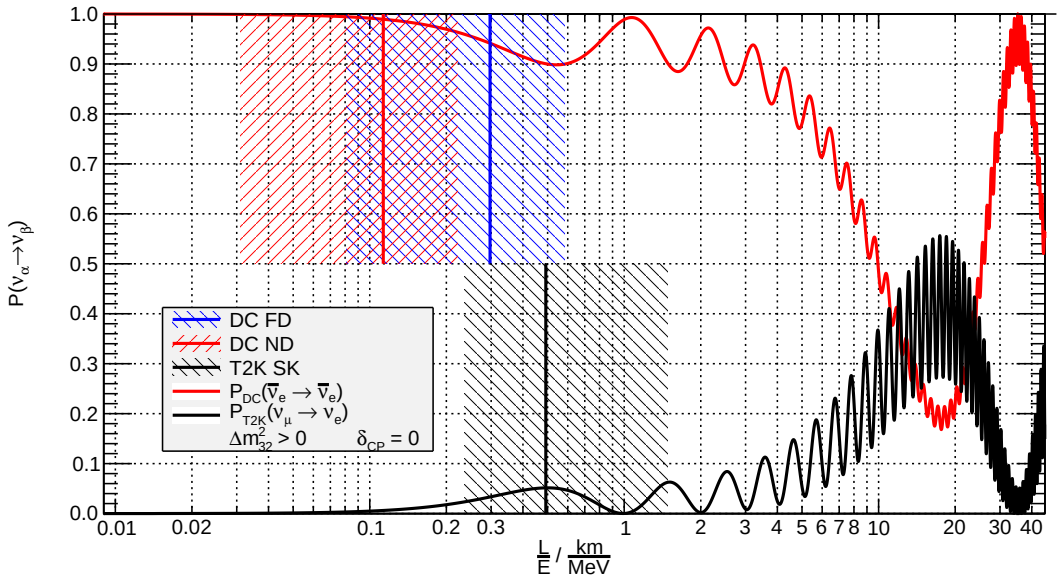

Figure 2.2: Vacuum oscillation probability functions of the Double Chooz and the T2K experiment. The survival probability of electron antineutrinos $P(\bar{\nu}_e \to \bar{\nu}_e)$ (red) is plotted along with the appearance probability of electron neutrinos $P(\nu_\mu \to \nu_e)$ (black). The experimentally accessible parts of these graphs are highlighted for the DC-far (blue), DC-near (red) and T2K-SK (black) detectors. The $\frac{L}{E}$ with highest expected number of events is denoted by a solid line in the same colour[6]. The T2K-ND280 detector is out of range at $4.7 \cdot 10^{-4} \frac{km}{MeV}$. The following values are assumed: $sin^2(2\theta_{13}) = 0.1$, $sin^2(2\theta_{12}) = 0.8$, $sin^2(2\theta_{23}) = 1.0$, $\Delta m^2_{21} = 7 \cdot 10^{-5}\ eV^2$, $\Delta m^2_{31} = \Delta m^2_{32} = 2.3 \cdot 10^{-3}\ eV^2$ and $\delta_{CP} = 0$.

for a reactor experiment and [22, p. 40]

$$
\begin{aligned}
P(\nu_\mu \to \nu_e) = {} & \sin^2(\theta_{23}) \sin^2(2\theta_{13}) \sin^2\left(\frac{\Delta m^2_{31} L}{4E}\right) \\
& + 2 \sin(\theta_{23}) \sin(2\theta_{13}) \sin(2\theta_{12}) \cos(\theta_{23}) \cos(\theta_{13}) \\
& \cdot \sin\left(\frac{\Delta m^2_{31} L}{4E}\right) \sin\left(\frac{\Delta m^2_{21} L}{4E}\right) \cos\left(\frac{\Delta m^2_{31} L}{4E} + \delta_{CP}\right) \\
& + \cos^2(\theta_{23}) \cos^2(\theta_{13}) \sin^2(2\theta_{12}) \sin^2\left(\frac{\Delta m^2_{21} L}{4E}\right)
\end{aligned}
\tag{2.12}
$$

for an accelerator experiment. The abbreviation

$$
\Delta m^2_{jk} := m^2_j - m^2_k \tag{2.13}
$$

has been used in these equations. The graphs of both functions are given in figure 2.2. The equations yield that the position of the minima/maxima in the graphs of figure 2.2 are

[6] For T2K the neutrino flux is peaked very narrow around 0.6 GeV such that most of the events are expected close to the solid line [7, p. 5]. For Double Chooz the neutrino spectrum is wider and events are expected throughout the entire shaded areas [8, p. 6].

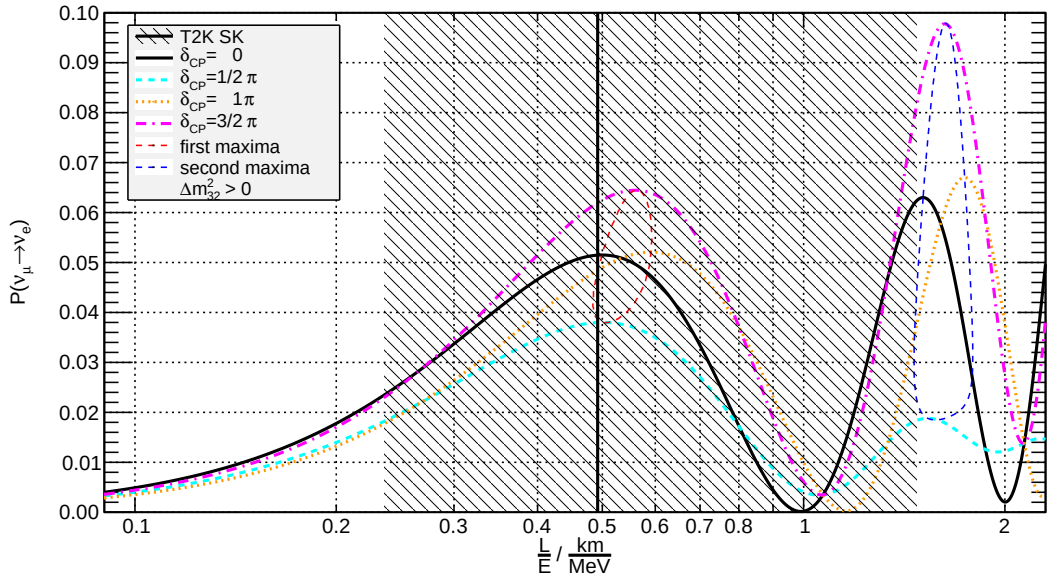

(a)

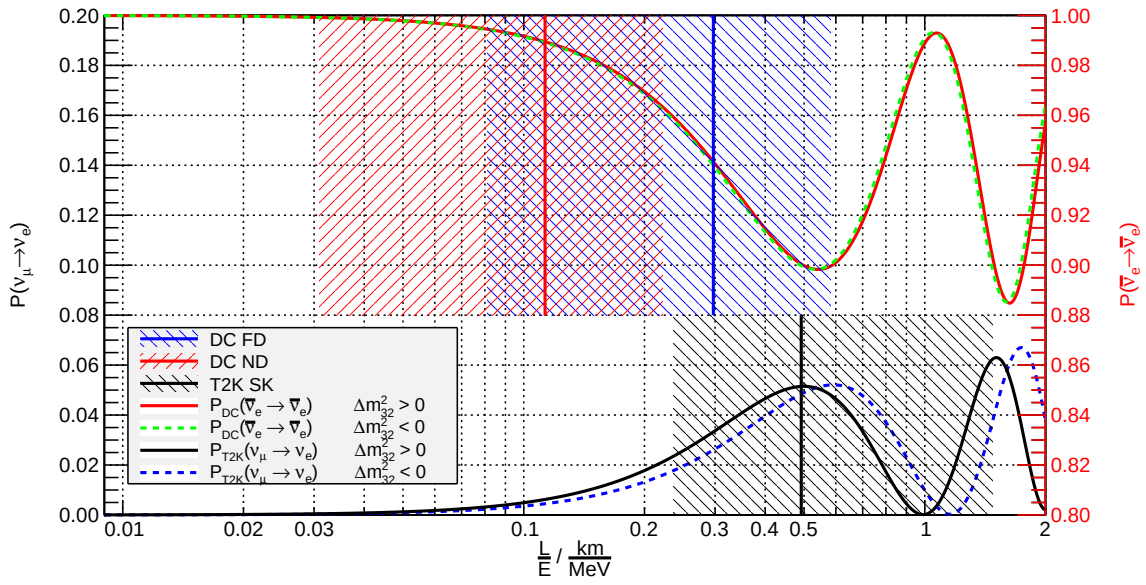

(b)

Figure 2.3: Influence of CP-violation and the neutrino mass hierarchy on the vacuum oscillation probability functions of the Double Chooz and the T2K experiments. Both figures are detailed views of figure 2.2 (See there for explanation). (a) Influence of δ_{CP} on the appearance probability. Graphs for $\delta_{CP} = 0$ (solid black), $\frac{1}{2}\pi$ (dashed cyan), π (dotted orange) and $\frac{3}{2}\pi$ (dotted-dashed magenta) are added. The coordinates of the first (second) maximum are connected by a small dashed red (blue) graph. (b) Influence of Δm^2_{32} on the appearance probability. Added are graphs for inverted mass hierarchy ($\Delta m^2_{32} = -2.3 \cdot 10^{-3}\ eV$) for $P(\bar{\nu}_e \to \bar{\nu}_e)$ (dashed green) and $P(\nu_\mu \to \nu_e)$ (dashed blue).

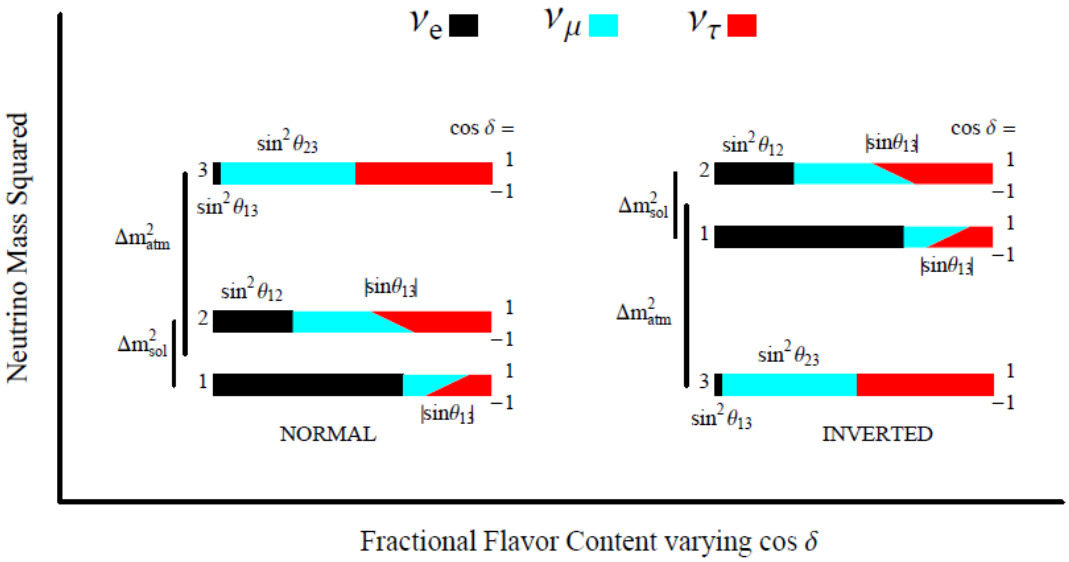

Figure 2.4: View of the two neutrino mass hierarchies and the effect of CP-violation on the mixing between flavour and mass eigenstates. The bottom of the bars correspond to $\cos(\delta_{CP}) = -1$ the top to $+1$. Fixed in this plot are the mixing angles: $\sin^2(\theta_{12}) = 0.30$, $\sin^2(\theta_{13}) = 0.03$ and $\sin^2(\theta_{23}) = 0.50$. One can see that the variation in the flavour admixture is in the order of $\sin(\theta_{13})$. [24, p. 3]

determined by the mass differences, while the amplitude is determined by the mixing angles. In this figure, the smaller oscillation with higher frequency is due to θ_{13}, the other due to θ_{12}. One should recognise that equation 2.11 is not dependent on δ_{CP} while 2.12 is dependent. Due to this dependency, the T2K experiment can only measure a combination of θ_{13} and δ_{CP}. This is illustrated in figure 2.3a, since for a fixed ratio of distance and energy $\frac{L}{E}$ it is possible to shift all graphs in figure 2.3a by tuning the value of $\sin^2(2\theta_{13})$ such that they have their common intersection point at this ratio $\frac{L}{E}$. Hence, T2K cannot directly infer on the value of δ_{CP}.

A further dependency of the oscillation probability is due to the mass hierarchy of the neutrinos. Up to the present date, it was only possible to measure two differences of neutrino masses. As a consequence, two possible hierarchies for the neutrino masses exist [24]. In the normal mass hierarchy scenario $m_1 < m_2 < m_3$ holds, in the inverted mass hierarchy scenario $m_3 < m_1 < m_2$ holds. This can be seen in figure 2.4. Although the form of equations 2.11 and 2.12 is unaffected by this, the values of the probabilities are affected, since the values of the mass differences are affected. Hence, each probability graph splits up in two graphs as shown in figure 2.3b. The influence for the Double Chooz experiment is negligible, but an additional dependency on the mass hierarchy exists for the T2K experiment.

Since the experiments are not located in vacuum, matter effects have to be considered. The effect on equation 2.11 is negligible in the Double Chooz experiment due to the short

distance of 1.05 km, but equation 2.12 gets modified to [22, p. 45]

$$
\begin{aligned}
P(\nu_\mu \to \nu_e) = \sin^2(\theta_{23}) \sin^2(2\theta_{13}) \frac{\sin^2\left(\frac{\Delta m^2_{31} L}{4E} - aL\right)}{\left(\frac{\Delta m^2_{31} L}{4E} - aL\right)^2} \left(\frac{\Delta m^2_{31} L}{4E}\right)^2 \\
+ \sin(2\theta_{23}) \sin(2\theta_{13}) \sin(2\theta_{12}) \frac{\sin\left(\frac{\Delta m^2_{31} L}{4E} - aL\right)}{\left(\frac{\Delta m^2_{31} L}{4E} - aL\right)} \\
\cdot \frac{\Delta m^2_{31} L}{4E} \frac{\sin(aL)}{aL} \frac{\Delta m^2_{21} L}{4E} \cos\left(\frac{\Delta m^2_{31} L}{4E} + \delta_{CP}\right) \\
+ \cos^2(\theta_{23}) \sin^2(2\theta_{12}) \frac{\sin^2(aL)}{(aL)^2} \left(\frac{\Delta m^2_{21} L}{4E}\right)^2 .
\end{aligned}
\tag{2.14}
$$

Here, a describes the effect of the interaction between the neutrinos and the matter. It is in the order of $10^{-3}\,\mathrm{km}^{-1}$ [22, p. 45].

Chapter 3

Overview of the Experiments

In this thesis, results from two experiments will be analysed. This chapter focuses on their experimental setup and their function principals. In general, a neutrino oscillation experiment works by comparing neutrino fluxes in different distances from a neutrino source. At least one source and two flux measurements are required. The difference between the fluxes can have two reasons: first, the fluxes differ due to the different distances from the source(s). The flux decreases inversely proportional to the square of the distance from the source, since the neutrinos distribute in a spherical segment away from the source and a ball surface increases proportionally with the square of the radius of the ball. The (average) distance from the sources to the far detector(s) is called the baseline of the experiment. Secondly, the flux difference can be due to neutrino oscillations. This effect is in general much smaller than the first.

Two measurement principles exist. Appearance experiments measure the appearance of neutrinos of different flavour than the initial flavour. Disappearance experiments measure the disappearance of neutrinos of the same flavour as the initial flavour. Depending on their actual setup some experiments can measure both effects.

Furthermore, neutrino oscillation experiments separate in different types according to their sources. The early experiments measured solar and atmospheric neutrinos while the recent neutrino experiments focus more on reactor and accelerator generated neutrinos.

3.1 The Double Chooz Experiment

The **D**ouble **C**hooz (DC) experiment [25] is a reactor experiment. It aims for the measurement of the survival probability of electron antineutrinos and thereby for the measurement of the lepton mixing angle θ_{13}, a parameter of the lepton mixing matrix U_{PMNS} as given in equation 2.10. By its measurement principle it is characterised as a pure disappearance experiment.

The Double Chooz experiment consists of two detectors measuring the neutrino flux from two nuclear reactors. The near detector is currently under construction and will have an approximate distance of 400 m to the reactor cores, the far detector has a distance of approximately 1050 m to the cores. The exact geometry can be seen in figure 3.1. In the two detector setup, the near detector provides a first measurement of the neutrino flux. This is taken as the unoscillated reference flux. The far detector then measures a second flux in a greater distance to the cores. This flux is called the oscillated neutrino flux. Assuming that the neutrino flux is isotropic, a prediction of the flux in the far detector can be made by

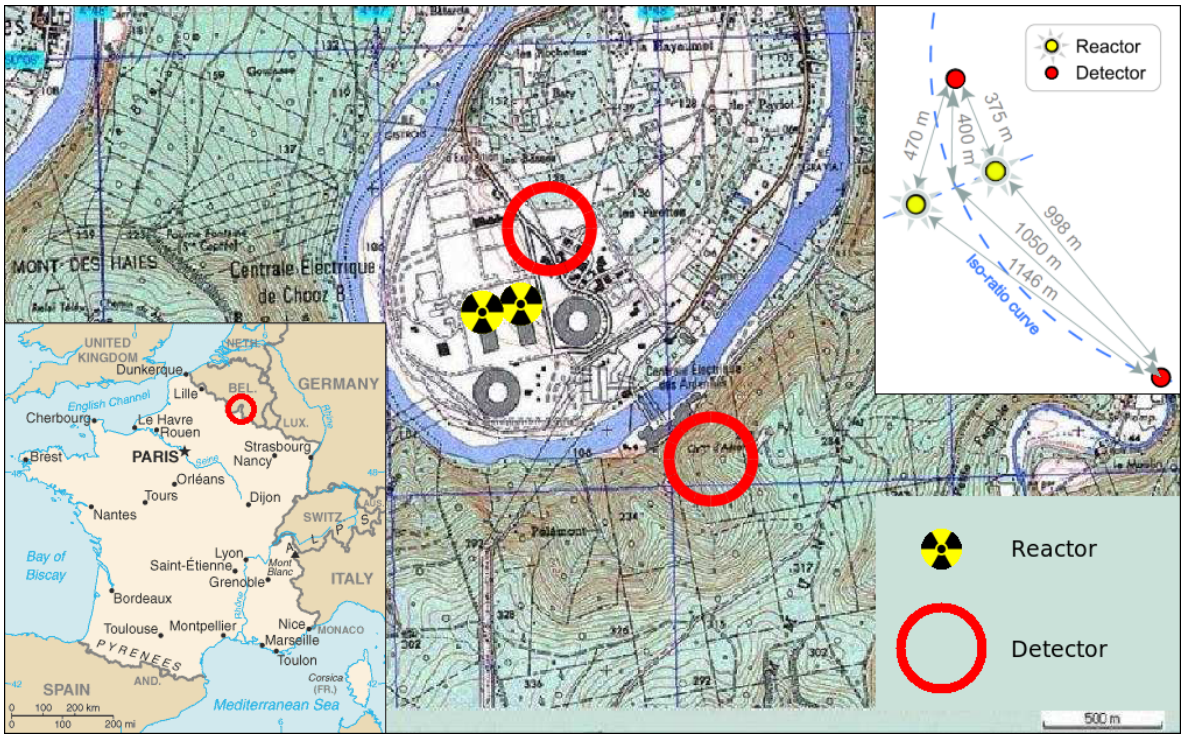

Figure 3.1: Geographical setup of the Double Chooz experiment: The large map shows the nuclear power plant site [25, p. 5]. The small map in the lower left corner shows the location of the experiment within Central Europe [26]. The small map in the upper right corner shows the precise distances of the reactors and detectors [27, p. 18].

extrapolating the measured flux of the near detector. The difference in the ratio between the measured far detector flux and its unoscillated prediction is due to neutrino oscillations and can be transformed in a value for θ_{13} by equation 2.11. In the current one detector setup, the prediction of the neutrino flux in the far detector has to be done by measuring the thermal output of the two reactors and converting it into the primary neutrino flux.

3.1.1 The Reactors

The source of the neutrinos are the two nuclear reactors CHOOZ-B1 and CHOOZ-B2. They belong to the Chooz nuclear power plant (Centrale nucléaire de Chooz) of the french electric utility company EDF (**É**lectricité **d**e **F**rance). The plant is located in France near the town of Chooz next to the Belgian border. The reactors are pressure water reactors of the type N4 and have an electrical power output of 2·1500 MW [28, p. 23]. In the one detector setup the thermal output of the reactors is used to predict the neutrino flux from the reactors. This flux calculation has large uncertainties due to changing reactor components and power output regulations. The evolution of the reactor components can be seen in figure 3.2. The evolution is caused by fission of certain isotopes on the one hand, and enrichment of certain isotopes, e.g. by neutron capture and subsequent nuclear transformation, on the other hand [28, p. 17]. Unlike other fission products, neutrinos can escape the reactor building due to their small cross section and can be measured in a detector outside the building.

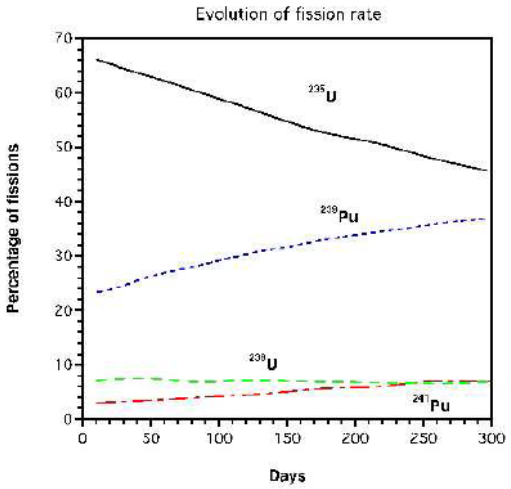

Figure 3.2: Evolution of the four dominating components of the Chooz reactors during a typical reactor cycle. [28, p. 19]

3.1.2 The Detectors

The Double Chooz detectors are liquid scintillator detectors. The far detector is located in the cavern of the dismantled CHOOZ-A reactor in the surrounding rock of the nuclear plant (cf. figure 3.1). It has an overburden of 300 m.w.e. (**m**eter **w**ater **e**quivalent) rock [25, p. 4]. The near detector is built in a new cavern next to the reactors and will have an overburden of 120 m.w.e. [29, p. 4]. The two detectors are designed equal in order to reduce systematic uncertainties between the two neutrino flux measurements. As shown in figure 3.3a, the main detector component is cylindrical, has a height and diameter of approximately 7 m and consists of several volumes enclosing each other. The detector components are in detail [25, pp. 63–67]:

► **Inner Detector:** The **I**nner **D**etector (ID) consists of the three cylindrical inner volumes of the detector. They are separated by transparent acrylic. To the outside volume, the ID is optically separated by a steel tank. On the inside of this steel tank 390 **P**hoto**m**ultiplier **t**ubes (PMT) are installed. Details can be found elsewhere [30]. They are all oriented towards the same central volume. In figure 3.3c these PMTs are displayed in red and blue. The three volumes are from the inside to the outside:

- **Neutrino Target:** The **N**eutrino **T**arget (NT) is filled with liquid scintillator and has a volume of 10.2 m^2. In this volume the detection reaction for the neutrinos shall take place. The scintillator is loaded with Gadolinium, which is necessary for the neutrino detection. The details of this will be described in section 3.1.3. The scintillator is responsible for the conversation of the neutrino energy into light visible for the PMTs. Wavelength shifters are mixed with the scintillator to shift the light to a wavelength for which the acrylic becomes transparent. Details on the scintillator components can be found elsewhere [31].
- **γ-Catcher:** The γ-**C**atcher (GC) encloses the NT volume. It is a hollow cylinder of 21.5 m^2 volume. It is filled with a similar mixture of liquid scintillator as the NT but without Gadolinium. In the case of a neutrino detection reaction near to the boundary of the NT, it has the purpose to convert escaping photons of this reaction into visible

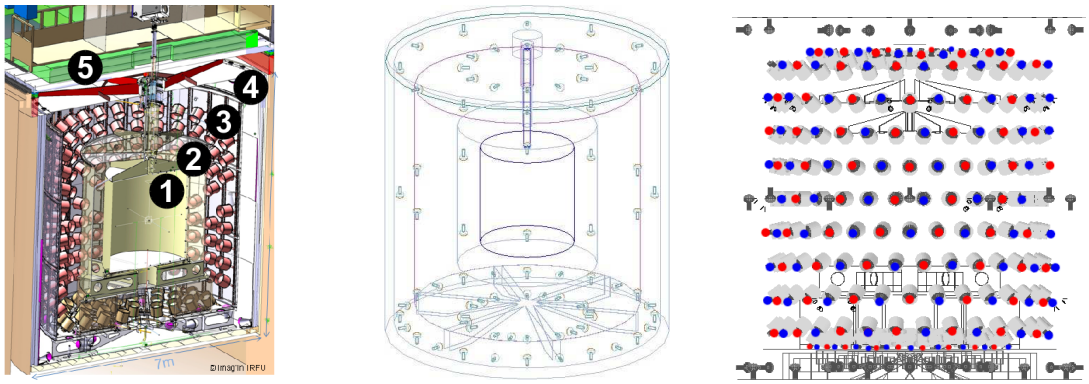

(a) (b) (c)

Figure 3.3: Sketch of the Double Chooz detectors: (a) Sectional drawing of the detector. (1)-(3) Inner Detector (with (1) Target, (2) γ-Catcher and (3) Buffer), (4) Inner Veto and (5) Outer Veto. The Inner Veto PMTs are not drawn correctly with respect to position and orientation. [33] (b) Arrangement of the Inner Veto PMTs in 5 rings. The PMTs are drawn correctly. [25, p. 87] (c) Arrangement of the Inner Detector PMTs (red and blue) and the Inner Veto PMTs (grey). All PMTs are drawn correctly. [34, p. 48]

light. Details on the exact composition of the scintillator can be found in reference [31].

• **Buffer:** The Buffer is the outer hollow cylinder of the Inner Detector enclosing the γ-Catcher. It has a volume of $100\,\mathrm{m}^2$ and is filled with non scintillating mineral oil. It accommodates the PMTs. Since the mineral oil is non scintillating, only the central region of the ID produces light. By this, neutrino detection reactions only take place in a volume in-between all PMTs and hence observed by all PMTs.

► **Inner Veto:** The **I**nner **V**eto (IV) volume encloses the ID. It is optically separated from the ID by a steel tank and is of hollow cylindrical geometry. It is filled with liquid scintillator and on the inside of the outer wall 78 PMTs are installed. The PMTs are oriented parallel to the walls as pictured in figure 3.3b. Most of the PMTs observe different volumes of the IV since the central steel tanks prevents the PMTs from observing the whole IV volume. The IV has the purpose to detect particles other than neutrinos coming from the outside into the detector. Many of these particles are able to mimic neutrinos and hence need to be rejected as background events. The IV is enclosed by a 17 cm thick steel shield in order to reduce the flux from atmospheric muons in the detector.

► **Outer Veto:** The **O**uter **V**eto consists of two double layers of plastic scintillator stripes mounted on the floor and 5 m above on the ceiling, respectively, of the laboratory [32, p. 4]. The lower layer is mounted directly above the steel shield and is visible in green in figure 3.3a. The OV outreaches the cylindrical part of the detector. By this, it is possible to detect atmospheric muons penetrating into the surrounding rock of the detector. Such muons can produce secondary particles which can then laterally enter the detector. More details on the OV can be found elsewhere [32].

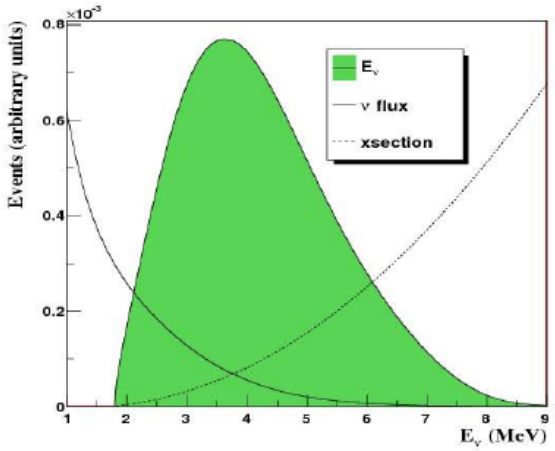

Figure 3.4: Expected neutrino energy spectrum in the Double Chooz detector compared with the neutrino flux and inverse β decay cross section. [35, p. 10]

3.1.3 The Neutrino Detection

In the last section, the detectors of the Double Chooz experiment have been described. In the central volume, the Neutrino Target, neutrinos are detected by the reaction of inverse β decay [25, p. 10]:

$$\bar{\nu}_e + p^+ \rightarrow e^+ + n \tag{3.1}$$

In this reaction, an electron antineutrino $\bar{\nu}_e$ hits a proton of the scintillator and converts into a positron and a neutron. The positron annihilates with an electron of the scintillator and deposits in the consequence $2 \cdot 511\,\text{keV}$ rest energy [13, p. 515] and kinetic energy from the initial neutrino in the scintillator [25, p. 10]. The neutrino energy can be computed from the corresponding positron energy via the equation [28, p. 18]

$$E_{\bar{\nu}_e} = E_{e^+} + (m_n - m_p) + O(E_{\bar{\nu}_e}/m_n). \tag{3.2}$$

Here, the positron energy is denoted as E_{e^+}, the neutrino energy is denoted as $E_{\bar{\nu}_e}$ and the masses of the proton and neutron are denoted as m_n and m_p, respectively. The energy spectrum of the positrons as seen in figure 5.1 is by equation 3.2 similar to the predicted neutrino energy spectrum in figure 3.4. The signal due to the positron annihilation is called the prompt signal. The neutron in reaction 3.1 produces a second signal, called the delayed signal, when it is captured by a Gadolinium nucleus. The nucleus gets excited by the capture and emits during its deexcitation a couple of photons with an approximate energy of 8 MeV [28, p. 69]. The neutron needs to thermalise, i.e. to decelerate to thermal energies, before the cross section for neutron capture on Gadolinium becomes so high that the capture actually takes place. This causes a delay between the prompt and the delayed signal of a few microseconds and is the characteristic signal of an inverse β-decay. Thus, for the selection of neutrino events in the detector, a cut on the prompt signal and delayed signal energy as well as the signal delay is used.

Atmospheric muons are able to enter the detector and fissure carbon atoms, which are a major component of the scintillator. Thus spallation products get generated in the detector by a large fraction of the entering muons. Some of these spallation products can mimic

inverse β decays, which leads to fake signals. These backgrounds can be rejected by inventing a veto time after each muon event in the Inner Veto in which no inverse β decay signals are accepted as valid. More selection criteria are invented in order to reject different types of other backgrounds. Details on the exact physics selection can be found elsewhere [8, p. 4].

3.1.4 Simulation and Reconstruction Software of the Double Chooz Experiment

The Double Chooz experiment uses for the analysis of its data and the simulation of the experiment a tailor-made software written in C++. The **D**ouble Chooz **O**ffline **G**roup **S**oftware (DOGS) is based on the particle physics analysis framework ROOT [36; 37], which is itself written in C++. The simulation package of the DOGS, which is responsible for the physics simulation in the detector, is the Generic Liquid-scintillator Anti-Neutrino Detector "**G**eneric**L**AND" **G**eant**4** **sim**ulation (GLG4sim) and is a Geant4 [38] application based on KGL4sim [39], the simulation software of the KamLAND experiment [3]. Aside of this simulation software, the DOGS simulates the electronics behaviour of the detector using its own electronic simulation package **R**ead**o**ut **S**imulation **S**oftware (RoSS). After being processed by GLG4sim and RoSS, the simulated events are in the exact same format as the real data. Both data types are then processed by the **C**ommon **T**runk (CT) which is responsible for the event reconstruction and low level event analysis. By this, the properties of the measured neutrino events can directly be compared with the full detector simulation of the measurement.

3.2 The T2K Experiment

The **T**okai-**to**-**K**amioka (T2K) experiment [40] is an accelerator neutrino experiment located in Japan. It is primarily designed for the study of oscillations between muon neutrinos and electron neutrinos; hence it is mainly an appearance experiment. For this studies, a muon neutrino beam is produced at the **J**apan **P**roton **A**ccelerator **R**esearch **C**omplex (J-PARC) located in Tokai and sent to the **S**uper-**K**amiokande (SK) detector located in Kamioka. The trajectory of the beam across Japan can be seen in figure 3.5. The SK detector is the far detector of the experiment. The near detector (ND280) is located on the J-PARC site 280 m behind the target, the point where the primary beam is converted into secondary particles which later decay and form the neutrino beam. The T2K experiment has a baseline of 295 km [40, p. 10]. The neutrino beam is not directly focused onto the far detector but in an angle of 2.5 ° to it [40, p. 10]. By this, T2K is characterised as an off-axis beam experiment. This technique is used to gain a cleaner muon neutrino beam which a sharper peak energy. The peak energy is adjusted to 0.6 GeV [40, p. 3], since at this energy the oscillation effect becomes maximal with respect to the baseline by equation 2.12. This can be seen in figures 2.2 and 2.3.

3.2.1 The Neutrino Beam

The T2K neutrino beam is produced at J-PARC using as primary particles protons from a MW-class proton synchrotron. The setup of the beam is given in figure 3.6. At first, an H^- beam is accelerated to 400 MeV by a linear collider (called LINAC in figure 3.6a). It is then charge-striped into an H^+ beam and in steps further accelerated. The final proton beam has a kinetic energy of 30 GeV. It is extracted from the main ring synchrotron (called 50 GeV PS

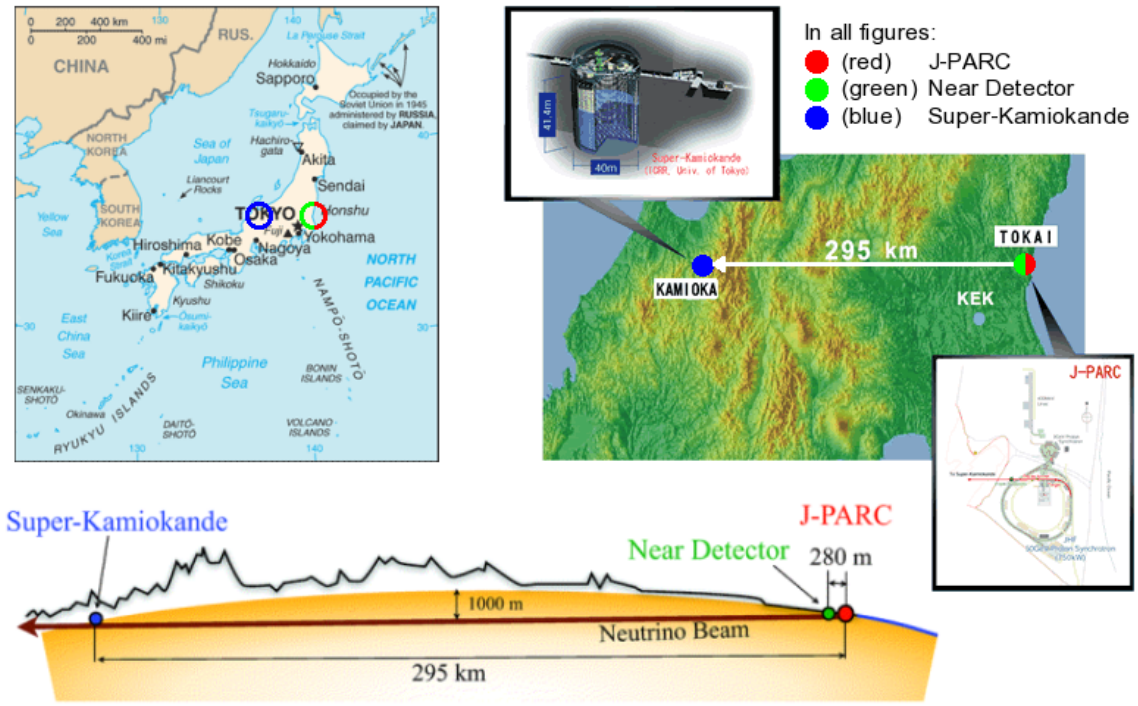

Figure 3.5: Geographical setup of the T2K experiment: on a political map of Japan (upper left figure) [26], on a physical map of Japan (upper right figure) [41] and in a schematic view of the neutrino beam through the main island of Japan (lower figure) [40, p. 3].

in figure 3.6a and Main Ring in figure 3.6b, respectively) in a fast extraction mode. By this, a spill of eight proton bunches is sent to SK. Due to this time structure, various backgrounds can be discriminated [40, p. 4]. The setup of the beamline after the extraction can be seen in figure 3.6b. After the extraction the proton beam is directed towards SK and focused on the target. In the graphite target, the protons interact with the graphite and produce a secondary beam of mainly pions and kaons. The secondary beam is focused by three magnetic horns and the pions and kaons decay in the following decay tunnel. This beamline part is depicted in figure 3.6c. The decaying particles form the tertiary neutrino beam, since the decay of a pion produces with 99.99 % a muon neutrino [13, p. 31]. The decay of a kaon produces with 5.07 % an electron neutrino, though. This is a major background for the appearance signal. The electron neutrino contamination of the muon neutrino beam is tracked by the near detector. Aside of neutrinos, leptons are produced in the decay tunnel as counterparts to the neutrinos. The leptons are stopped in a beam dump behind the decay tunnel.

3.2.2 The Detectors

The T2K experiment uses two different detector concepts for its far and its near detector.
– **Near Detector:** The **n**ear **d**etector (ND) itself consists of two detector parts. One is installed in on-axis direction and monitors the beam properties. The second detector is installed off-axis on the direct connection line between target and far detector [40, pp. 11–22]. A view of the near detector complex can be found in figure 3.7a. In this figure, the upper

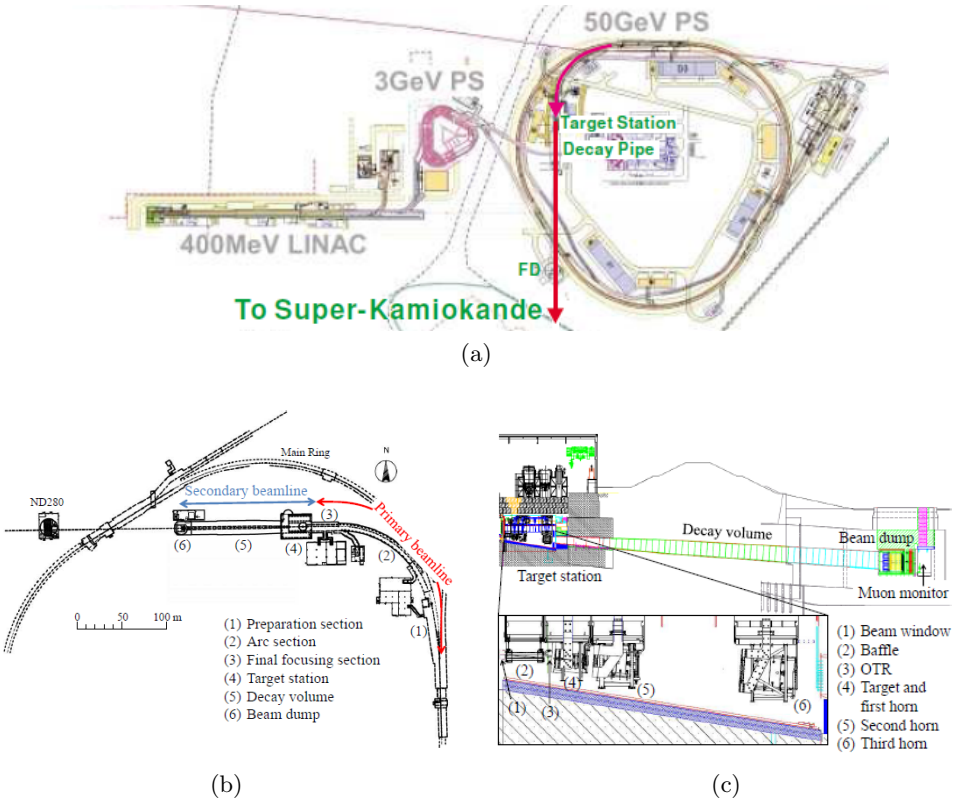

Figure 3.6: Sketch of J-PARC beamline: (a) Overview on the whole accelerator beamline at J-PARC [42, p. 8]. (b) Detailed view of the final segments of the J-PARC beamline including the near detector site [40, p. 5]. (c) Detailed view of the secondary beamline [40, p. 7].

part is the off-axis detector called ND280, because it has a distance from the target of 280 m. The lower part is the on-axis detector called INGRID.

► **ND280:** The off-axis detector is drawn in an explosion sketch in figure 3.7b. It consits of several subdetectors. They are separated by their position in the inner detectors and the outer detectors.

• **Inner Detectors:** The inner detectors are the π^0 **d**etector (P0D) and following in downstream direction (with respect to the neutrino beam) a setup of two **f**ine **g**rained **d**etectors (FGD) being interlaced with three **t**ime **p**rojection **c**hambers (TPC). The P0D tracks muon neutrinos which produce a uncharged pion. It works via a series of fine grids of perpendicular scintillator stripes interlaved with brass, lead and water planes. The TPCs are capable of identifying charged particles by their energy deposition and the curvature of their tracks due to the magnetic field in the detector. The magnetic field is generated by the former **U**nderground **A**rea **1** (UA1) magnet[1], which encloses the TPCs. The FGDs provide target mass for the neutrino interactions being measured with the TPCs. Moreover, the FGDs themselves can measure tracks of charged particles coming from the neutrino interactions points via scintillator bars. These are oriented in perpendicular directions and in several planes.

[1] This magnet is recycled from the 1981–1993 UA1 CERN experiment [43].

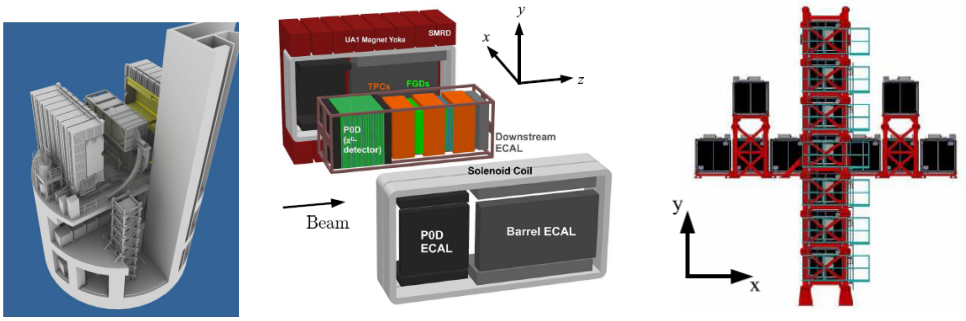

(a) (b) (c)

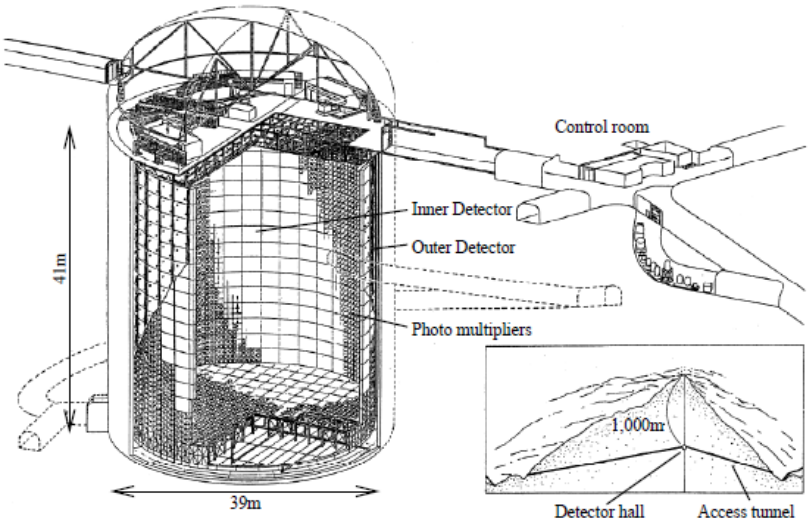

(d)

Figure 3.7: Sketch of the T2K detectors: (a) Overview on the near detector site with the off-axis detector in the upper picture and the partly covered on-axis detector beneath [40, p. 11]. (b) Explosion sketch of the off-axis near detector [40, p. 15]. (c) Front view of the on-axis near detector [40, p. 13]. (d) Sketch of the far detector [42, p. 13].

• **Outer Detectors:** Enclosing the three inner detectors, several **e**lectromagnetic **cal**orimeters (ECal) measure the energy of escaping particles. The ECals are sampling calorimeter, being built of plastic scintillator bars and lead absorber sheets. They separate into P0D-ECal and Barrel-ECal/Downstream-ECal according to the inner subdetectors they complement. Their position can again be seen in figure 3.7b. The last of the outer subdetectors is the **s**ide **m**uon **r**ange **d**etector (SMRD). It consist of scintillator stripes being installed in-between the steel plates of the return yoke of the magnet. They measure tracks and momenta of escaping muons. These muons cannot be captured in the ECals. Furthermore, the SMRD is used as a veto detector against atmospheric muons and can detect events in the walls and the yoke being induced by the outer parts of the beam. By the functional interaction of all the subdetectors, the primary composition of the neutrino beam can be probed

in a sufficient manner.

► **INGRID:** The lower part in figure 3.7a shows the on-axis near detector. It is called **i**nteractive **n**eutrino **grid** (INGRID) and shown again in figure 3.7c. It consists of 16 segments of interlaced iron and perpendicular oriented scintillator planes. The modules are arranged in a cross of seven modules in horizontal and seven modules in vertical direction. The centre of the beam coincides with the centre of the cross. By the design of INGRID, the position of the beam centre can be sufficiently measured. From this information, the off-axis angle, i.e. the angle between the neutrino beam direction and the connection line from SK to the target, can be computed and corrections in the expected neutrino flux and energy can be made on a daily basis. As seen in figure 3.7c, two additional modules are installed outside the original cross geometry. They are used for probing the axial symmetry of the neutrino beam.

– **Far Detector:** The far detector of the T2K experiment is the **S**uper-**K**amiokande (SK) detector located in the Kamioka mine. It is a water Cherenkov detector of 50 kton and equipped with approximately 13000 PMTs. It has a cylindrical geometry and its **i**nner **d**etector (ID) volume is 33.8 m in diameter and 36.2 m in height. 11129 inward-facing PMTs are mounted on the inside of the outer boundary of the ID. Optically separated is the **o**uter **d**etector (OD). It is a hollow cylinder which is in lateral direction and in axis direction 2 m thick. On the inside of its inner boundary, 1885 outward-facing PMTs are mounted. The OD is used as a veto against atmospheric muons and other types of backgrounds. A detailed report on the SK detector can be found elsewhere [44].

3.2.3 The Neutrino Detection

The idea of the T2K experiment is to measure the appearance of electron neutrinos in an initial muon neutrino beam. This measurement is done in two steps:

In the off-axis near detector, the measurement of muon neutrino interactions like

$$\nu_\mu + B \rightarrow \mu + B' + n\pi \tag{3.3}$$

is performed to gain the number of muon neutrino events in the initial beam. Here B and B' represent Baryons and $n \in \mathbb{N}$ counts the number of produced pions. By this, an expectation for the number of events in the far detector is achieved. For a valid event in this measurement, it is required that no veto signals are present. Moreover, only the most energetic track in the FGDs which enters the downstream TPC is selected. This track has to correspond to a negative charged particle and its energy loss must be compatible to a muon. Additionally, the upstream TPC may not contain a track to reject trajectories starting outside the detector. More details on the selection can be found elsewhere [7, p. 5]

Knowing this number, a search for electron neutrinos is performed in the far detector. Since the neutrino beam can make signals in the OD of the far detector, which would lead to a veto, the precise bunching information and time from the neutrino beam spill is transferred to the far detector to trigger the measurement. In the far detector, neutrinos are measured by Cherenkov light which is generated in water when a neutrino participates in a **c**harged **c**urrent **q**uasi **e**lastic (CCQE) interaction. In this interaction the corresponding lepton to the initial neutrino is produced. If the kinetic energy of the newly generated lepton is so high that it travels through the water of the detector faster than light would, a cone of light is produced similar to the supersonic cone of a plane in air. The SK far detector is able to measure the energy of the particle by the energy dependent opening angle of the cone. Moreover, it is

able to distinguish between electrons and muons by their cone geometries. The cone of an electron is fuzzier than the cone of a muon because an electron produces an electromagnetic shower on its way through the water. The cone of an electron can hence be seen as the sum of several single cones giving a fuzzy overall cone. A valid electron neutrino event in the SK far detector is defined by seven cuts:

The reconstructed vertex of the CCQE interaction must be within the fiducial volume, within the trigger window and must be fully contained in it. It must have an electron like single ring. The ring corresponds to the Cherenkov cone projected onto the surface of the detector where the PMTs are mounted. The visible energy must be above 100 MeV and no delayed electrons must be in the detector. The misidentification of π^0 mesons as electrons is suppressed by artificially forcing the reconstruction of a second cone and discriminating events with a thereby reconstructed invariant mass of more than 105 MeV. This rejects π^0 which decay in two photons giving two cones with an invariant mass of 135 MeV [13, p. 623]. A last cut rejects the electrons from the kaon background in the secondary beam component by requiring the energy of the electrons to be below 1250 MeV. Details on the selection in the far detector can be found elsewhere [7, pp. 5–6].

3.2.4 Simulation and Reconstruction Software of the T2K Experiment

The T2K experiment uses different software packages for the entire simulation process. The simulation of proton interactions in the target is done by FLUKA [45], the horn simulation and secondary beamline simulation is done by GEANT3 [46]. The interactions in the ND280 detector is done redundantly by GENIE [47] and NEUT [48]. Both packages are GEANT4 [38] based. The interactions in SK are done by the established GEANT3 based software of the former SK collaboration. The event selection is done by a tailor-made C++ program utilising the common ROOT [36; 37] packages.

Chapter 4

Statistical Methods in Neutrino Physics

In this chapter, statistical methods which are repeatedly used throughout the following analyses are explained in a general manner. This includes function fitting methods, correlated random draws and the calculation of confidence sets.

4.1 Function Fitting

It is often the case that one wishes to describe certain numbers measured in several classes by an analytical function, which then expresses the predicted number as a function of the classes. For example the classes could be the energy of the measured neutrinos and the numbers are the numbers of neutrinos in each class. The function then describes the expected number of neutrinos in each class as a function of energy. The classes are often called bins in physics. The optimal function is found by minimising a goodness-of-fit statistic. This statistic is a generalisation of Pearson's χ^2 goodness-of-fit test statistic [49, p. 168]

$$\chi^2_P := \sum_{k=1}^{n} \frac{(O_k - E_k)^2}{E_k}, \tag{4.1}$$

where χ^2_P is Pearson's test statistic which asymptotically approaches a χ^2 distribution. The number of classes in which the statistic is evaluated is n (in the upper example this is the number of energy bins), O_k is the observed frequency in the k^{th} class and E_k is the expected frequency in the k^{th} class. This expectation is dependent on the function

$$E_{\overrightarrow{\alpha}} : \mathbb{N} \to \mathbb{R}; k \mapsto E_k = E(k, \overrightarrow{\alpha}), \tag{4.2}$$

which shall be fitted. This function is not only a function of the class number k but also of additional parameters $\overrightarrow{\alpha}$ which are varied during the minimisation such that the value of χ^2_P in equation 4.1 becomes minimal. Thus the fitting of $E_{\overrightarrow{\alpha}}$ coincides with the optimisation of $\overrightarrow{\alpha}$.

The statistic used in physics is not exactly Pearson's χ^2 statistic, but a modification of this statistic that accounts for the uncertainties in the measurement. The used statistic is

called Neyman's χ^2 statistic and reads as [50, p. 438]:

$$\chi^2_N := \sum_{k=1}^{n} \frac{(O_k - E_k)^2}{O_k}. \tag{4.3}$$

A pathological case in Neyman's χ^2 can occur when the number of measured events in a certain class O_k is zero. To prevent the denominator to become zero in such cases, a modified version of Neyman's χ^2 statistic is widely used [51, p. 386]:

$$\chi^{2*}_N := \sum_{k=1}^{n} \frac{(O_k - E_k)^2}{\max(O_k, 1)}. \tag{4.4}$$

However, in this thesis the case of zero events is never encountered and thus Neyman's χ^2 always refers to χ^2_N given in equation 4.3.

A way to motivate Neyman's χ^2 statistic is the idea that the number of events in the k^{th} class X_k is a random variable distributed according to a Poisson distribution with parameter λ. This assumption is common for counting experiments [51, p. 386]. Taking O_k as the estimator for λ and keeping in mind that

$$\mathrm{E}[X_k] = \mathrm{Var}[X_k] \tag{4.5}$$

holds for a Poisson distribution, the variance of the Poisson distribution becomes O_k. This is the O_k in the denominator of equation 4.3. It is then generally assumed that the Poisson distribution can be approximated by a binomial distributions which itself is assumed to be approximable by a Gaussian distributions $N(O_K, O_K)$. Writing this as $N(m_k, \sigma_k^2)$ one can show that minimisation of χ^2_N coincides with a maximisation of the goodness-of-fit likelihood assuming Gaussian uncertainties. The likelihood function is given as [52, p. 440]

$$\mathcal{L} = \prod_{i=1}^{N} f^{X_k}(x_k|\overrightarrow{\alpha}), \tag{4.6}$$

where $f^{X_k}(x_k|\overrightarrow{\alpha})$ is the density of a random variable X_k and all X_k with $1 \leq k \leq n$ are independently and identically distributed. The parameters of the density function are collected in $\overrightarrow{\alpha}$. Now, if the densities $f(x_k|\overrightarrow{\alpha})$ are Gaussian density functions with parameters (m_k, σ_k^2) from

$$\mathcal{L} = \prod_{k=1}^{n} \left[\frac{1}{\sigma_k\sqrt{2\pi}}\right] \exp\left[-\sum_{k=1}^{n} \frac{(x_k - m_k)^2}{2\sigma_k^2}\right] \tag{4.7}$$

$$\Rightarrow \log\mathcal{L} = -\frac{1}{2}\sum_{k=1}^{n} \frac{(x_k - m_k)^2}{\sigma_k^2} - \frac{1}{2}\sum_{k=1}^{n} \log(\sigma_k^2) - \frac{1}{2} n \log(2\pi)$$

$$\Rightarrow \log\mathcal{L} = -\frac{1}{2}\chi^2_N - \frac{1}{2}\sum_{k=1}^{n} \log(\sigma_k^2) - \frac{1}{2} n \log(2\pi) \tag{4.8}$$

$$\Rightarrow \frac{\partial \log\mathcal{L}}{\partial m_k} = 0 \Leftrightarrow \frac{\partial \chi^2_N}{\partial m_k} = 0 \quad \forall\ 1 \leq k \leq n \tag{4.9}$$

follows that finding the maximum value of $\mathcal{L}$ coincides with minimising Neyman's χ^2 statistic, since the logarithm is a strictly monotone function [52, p. 442] [53, p. 125].

In practice, often advantage is taken of the addition theorem for Gaussian distributions [52, p. 150]. It is assumed that each effect, which causes the number of events in a class to fluctuate, causes this number to fluctuate according to a Gaussian distribution. The variances according to each effect are evaluated and due to the addition theorem added to the overall variance. This is then used as the denominator in equation 4.3, justified by the upper explanation.

In the case of vanishing denominator, e.g. $O_k = 0$, it is, apart from equation 4.4, in principle also possible to use

$$\chi^2_{N*} := \sum_{\{k|O_k>0\}} \frac{(O_k - E_k)^2}{O_k} \tag{4.10}$$

as χ^2 statistic. This is disfavoured with respect to 4.4, because the value of χ^2_N is often interpreted in terms of goodness-of-fit. When using 4.10, information about the goodness-of-fit in the "empty" ($O_k = 0$) classes is effectively ignored. Since the case of $O_k = 0$ is only likely to happen for a Poissonian density function (zero events counted in a class) and not for a Gaussian density function ($\sigma_k^2 = 0$ gives no proper distribution) 4.4 uses in this case the variance of the next greater possible outcome of a Poisson distribution ($O_k = 1$) as lower bound for the denominator.

For the minimisation of Neyman's χ^2 statistic in practice, a subroutine of the ROOT framework [36] called Minuit [54] is used. In the Minuit program itself, several minimisation routines are implemented. The default method is called MIGRAD and is a implementation of Fletcher's switching variant [55] of the original Davidon-Fletcher-Powell algorithm [56], a quasi-Newtonian minimisation algorithm. This method is used unless a different method is stated in this thesis.

4.2 The MultiSim Method

At several points in the following analyses it is necessary to derive a distribution for a certain random variable, which is dependent on several other random variables. These are called the (random) parameters of the first random variable. These random parameters can possibly be correlated to each other. The computation of the dependent random distribution is normally done by the so called **multi**ple **sim**ulation (MultiSim) method. The method belongs to the family of **M**onte **C**arlo (MC) methods [57]. The idea of this method is to perform a random draw on the value of each parameter according to its random distribution. The value of the dependent random variable is then calculated using the current realisation of the random parameters. Then a new set of random parameters is randomly drawn according to their respective distribution and the new value of the dependent random variable is again computed. This is repeated until a sufficiently smooth random distribution of the dependent variable is gained.

In the default implementation of this method, the first step is to determine the distributions of the random parameters. The analytical form of the distributions is in principle not needed in the MultiSim method, thus a repeated measurement of the parameters until one gains a smooth distribution is sufficient. Nevertheless, in the most cases it is assumed that the random parameters are distributed according to a Gaussian distribution.

In the case of uncorrelated random parameters the first step is a random draw from a standard normal distribution for each parameter. The outcome of the i^{th} random draw is

multiplied with the variance of the i^{th} random parameter and added to the i^{th} mean. If the thereby gained value of the parameter is outside a physical boundary, the value is reset into the physically allowed region. Finally, the value of the dependent random variable is calculated from the current realisations of the parameters.

In the case of correlated random parameters, the first steps coincide with the above method. Then the outcomes are arranged in a vector. The vector is then matrix multiplied with the covariance matrix of the correlated parameters. In practise, Cholesky's decomposition [58, p. 524]

$$D = L^T L \tag{4.11}$$

of the covariance matrix D is determined and the gained triangular matrix L is multiplied with the vector x of drawn deviations.

$$Lx = y \tag{4.12}$$

The gained vector y includes now the correlated random shifts to the means (central values). Cholesky's decomposition is applicable since covariance matrices are for not linear dependent variables of the symmetric positive definite type [59, pp. 234–235].

Since, the analytical form of the random parameter distributions were not of interest for the MultiSim method, this method works in principle for arbitrary random distributions.

4.3 Random Draws and Physical Boundaries

It is often the case that within a simulation method like the one in section 4.2 draws of a random variable according to a probability distribution function are performed. Often this is done assuming a Gaussian distribution or other symmetric distributions with the real numbers as support. Not seldom, a theoretical reason restricts the physically allowed region of the parameter to a proper subset of the real numbers. In this case, two common methods exist to handle the case of an unphysical random draw outcome: the outcome is resetted into the physical region by accounting every unphysical outcome as an outcome to be exactly at the physical boundary or the outcome is dumped. By doing so, the Gaussian **p**robability **d**ensity **f**unction (pdf) is implicitly modified. This is illustrated in figure 4.1a. The physically allowed region in this example is the set of the non-negative real numbers. The original unmodified distribution is plotted in green. The dumping method modifies this pdf to the orange one. Due to normalisation this graph is above the original green graph. The distribution of the resetting method is plotted in blue. Here the number zero has an explicit probability and the distribution is therefore a compound of a probability density function for $x \neq 0$ and a **p**robability **m**ass **f**unction[1] (pmf) for $x = 0$. Both methods have the disadvantage that the means of both modified distributions do not coincide with the modes of these functions. For the unmodified function, the mode coinsides with its mean. The mode is not affected by the modification of the original function, but the mean is affected. This is visualised in figure 4.1a in which the dashed lines show the means of the functions of same colour. As the mean is the value that is measured in an experiment, the modification introduces a bias with respect to the true value (which coincides with the green dashed line). The resetting method has the additional disadvantage of a discontinuous point within the physically allowed region. The discontinuity is located at the physical boundary (cf. blue graph in figure 4.1a at $x = 0$). By

[1] The compound pdf/pmf could technically be restored to a pure pdf by the utilisation of Dirac's δ function.

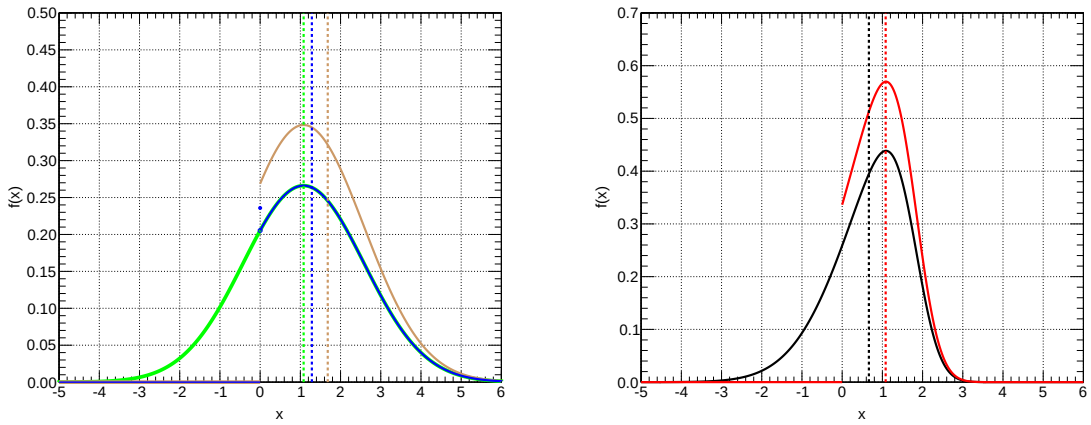

(a) (b)

Figure 4.1: Random draws at physical boundaries. (a) shows the original pdf (green) and the default methods of truncating this pdf at the physical boundary (orange) and the mixed pdf/pmf of the resetting method (blue) as described in the text. (b) shows the pdf of the truncated tuned O'Hagan-Leonhard skew Gaussian distribution (red) as explained in the text. For comparison, the not truncated distribution with the same parameter set is plotted (black). In both figures, the corresponding means of the pdfs/pmfs are denoted by dashed vertical lines of the same colour as the pdfs/pmfs.

shifting the distribution until the mean again coincides with the true value, the bias issue can be solved. Nevertheless, the issue of not coinciding mode and mean remains.

It is possible to regain a physically meaningful distribution, i.e. with coinciding mode and mean, without a bias and without discontinuities in the physical allowed region, by introducing a skewness to the truncated Gaussian distribution. The pdf of O'Hagan's and Leonard's skew Gaussian distribution of the parameters (ξ, ω, α) is given as [60]

$$f^X(x) = \frac{2}{\omega}\phi\left(\frac{x-\xi}{\omega}\right)\Phi\left(\alpha\frac{x-\xi}{\omega}\right), \tag{4.13}$$

where ϕ and Φ are the pdf and **c**ummulative **d**ensity **f**unction (cdf) of the standard normal distribution, respectively. If the shape α is set to zero, a Gaussian pdf with mean ξ and variance ω^2 is regained. The truncated orange pdf in figure 4.1a can now be tuned by the shape parameter α until the mean coincides with the mode. During this, the mode is fixed to the true value. The resulting distribution is shown in figure 4.1b in red. The scale parameter ω can be tuned such that the variance of the skew distribution coincides with the original variance of the original not truncated Gaussian distribution. By this procedure an unbiased realistic physically meaningful distribution can be rendered.

4.4 Confidence Sets

When performing a measurement, it is of general interest to not only give a maximum likelihood point estimator for the measured variable. It is also of essential importance to provide a

set which covers the true value of the measurand with a certain probability. This is especially important as the latter gives essentially a statement on the reliability of the former.

4.4.1 The χ^2 Approach

A common method for the construction of such point estimates and confidence sets is based on the χ^2 function used in section 4.1. Let our parameter of interest be one of the components of $\overrightarrow{\alpha}$ in equation 4.6 called $\widetilde{\alpha}$. Neyman's χ^2 function is minimised by solving equation 4.9 and the value $\widetilde{\alpha}_{best}$, which minimises χ^2_N is taken as point estimate for $\widetilde{\alpha}$. Now, the χ^2_N statistic is taken as function of the only parameter $\widetilde{\alpha}$. For finding the confidence set that covers the true value of $\widetilde{\alpha}$ with $0 \leq \gamma \leq 1$ probability, the γ quantile of the χ^2 distribution with 1 degree of freedom is evaluated. This is denoted with $\chi^2_{1;\gamma}$ in the following. Next, the values for $\widetilde{\alpha}$ are computed for which

$$\chi^2_N(\widetilde{\alpha}) - \chi^2_N(\widetilde{\alpha}_{best}) = \chi^2_{1;\gamma} \tag{4.14}$$

holds. Let us denote the values of $\widetilde{\alpha}$ that satisfy equation 4.14 with $\widetilde{\alpha}_{\gamma;\star}$, where $\star \in \{\ominus;\oplus\}$ and $\ominus$ denotes the smaller value of $\widetilde{\alpha}$ satisfying equation 4.14 and $\oplus$ denotes the larger value doing so. As χ^2_N could have some skewness it might be that

$$\Delta\widetilde{\alpha}_{\gamma;\ominus} := \widetilde{\alpha}_{best} - \widetilde{\alpha}_{\gamma;\ominus} \neq \widetilde{\alpha}_{\gamma;\oplus} - \widetilde{\alpha}_{best} =: \Delta\widetilde{\alpha}_{\gamma;\oplus}. \tag{4.15}$$

As a conservative variant, the γ confidence set is given as the interval

$$[\widetilde{\alpha}_{best} - \max_{\star\in\{\ominus;\oplus\}} \{\Delta\widetilde{\alpha}_{\gamma;\star}\}; \widetilde{\alpha}_{best} + \max_{\star\in\{\ominus;\oplus\}} \{\Delta\widetilde{\alpha}_{\gamma;\star}\}] \tag{4.16}$$

or more often stated as

$$\widetilde{\alpha}_{best} \pm \max_{\star\in\{\ominus;\oplus\}} \{\Delta\widetilde{\alpha}_{\gamma;\star}\}. \tag{4.17}$$

This is often referred to as a symmetric uncertainty. If it is plausible that inequality 4.15 is true due to a physical reason and not due to a statistical fluctuation, the asymmetric interval

$$[\widetilde{\alpha}_{\gamma;\ominus}; \widetilde{\alpha}_{\gamma;\oplus}] \tag{4.18}$$

is taken as the confidence set. This is again more often stated as

$$(\widetilde{\alpha}_{best})^{+\Delta\widetilde{\alpha}_{\gamma;\oplus}}_{-\Delta\widetilde{\alpha}_{\gamma;\ominus}}. \tag{4.19}$$

It is common practice in physics to derive a point estimate and an uncertainty for a measured parameter with the χ^2 approach and to state either 4.17 or 4.19 for $\gamma = 68\%$ confidence[2].

This approach relies on the assumption that the relevant uncertainties are distributed according to a Gaussian distribution, since in this case maximum likelihood estimation and minimum χ^2 estimation coincide as proven in section 4.1.

[2]This number is motivated by the fact that $68\% = P(-1 < x < 1)$ for x being a realisation of a standard normal distributed random variable.

4.4.2 The Confidence Belt Approach

A more sophisticated way of gaining the confidence set is given by the confidence belt approach. This approach is often favoured when the interval in 4.18 includes unphysical values. The confidence belt approach aims for the construction of an interval that covers the true value ζ_{true} of a physical parameter ζ with a given probability. In general, ζ is a parameter of a theoretical model that gives a prediction on the value of the measurand x. It is also possible that ζ itself is the measurand. However, with every measurement of x a (direct or indirect) measurement of ζ is performed. Thus, ζ is also called measurand in the following, although strictly speaking only x can be measured directly. The probability of coverage is known as **c**onfidence **l**evel (C.L.) in physics and will be denoted as $1-\alpha$ in the following. A confidence interval is defined as follows [52, p. 490]:

Let

$$\overrightarrow{X} = (X_1, ..., X_n),\ n \in \mathbb{N} \tag{4.20}$$

be the random vector of n draws of the random variable X. Let the probability distribution of X be dependent on a parameter ζ. The true value ζ_{true} of ζ must not be known for this. Let further be

$$\underline{L}(\overrightarrow{X}) \leq \overline{L}(\overrightarrow{X}) \tag{4.21}$$

two statistics of $\overrightarrow{X}$. These statistics are implicitly dependent on ζ as X is dependent on ζ. If it holds that

$$P(\underline{L}(\overrightarrow{X}) \leq \zeta \leq \overline{L}(\overrightarrow{X})) \geq 1-\alpha \tag{4.22}$$

the interval

$$[\underline{L}(\overrightarrow{X}); \overline{L}(\overrightarrow{X})] = [\underline{L}(\overrightarrow{X}(\zeta)); \overline{L}(\overrightarrow{X}(\zeta))] \tag{4.23}$$

is called a confidence interval of the $1-\alpha$ confidence level. Note that in equation 4.22 the parameter ζ is fixed, so 4.22 expresses the probability that the interval 4.23 covers the parameter ζ. For a continuous random variable X equation 4.22 can be replaced by

$$P(\underline{L}(\overrightarrow{X}) \leq \zeta \leq \overline{L}(\overrightarrow{X})) = 1-\alpha. \tag{4.24}$$

Intervals satisfying equation 4.24 are said to have correct coverage. Intervals satisfying only equation 4.22 are said to overcover. By finding other pairs of statistics satisfying equation 4.22 other confidence intervals to the same confidence level can be found resulting in an ambiguity. Common confidence intervals are the one-sided confidence intervals

$$[\underline{L}_u(\overrightarrow{X}); \infty] \text{ and } [-\infty; \overline{L}_l(\overrightarrow{X})] \tag{4.25}$$

where equation 4.22 is modified to either

$$P(\underline{L}_u(\overrightarrow{X}) \leq \zeta) \geq 1-\alpha \text{ or } P(\zeta \leq \overline{L}_l(\overrightarrow{X})) \geq 1-\alpha \tag{4.26}$$

and the central confidence interval

$$[\underline{L}_c(\overrightarrow{X}); \overline{L}_c(\overrightarrow{X})] \tag{4.27}$$

where additionally to equation 4.22 the equation

$$P(\zeta \leq \underline{L}_c(\overrightarrow{X})) = P(\overline{L}_c(\overrightarrow{X}) \leq \zeta) \tag{4.28}$$

holds. In any case, it is desireable to find the smallest confidence interval for which equation 4.22 or its modifications hold, i.e. the interval with correct coverage.

In the confidence belt approach, an interval as described above is constructed in two steps [53, pp. 105–107]. In the first step, an interval $c(\zeta_{assu})$ is constructed such that

$$P\left(\zeta_{meas} \in c(\zeta_{assu})\right) = 1 - \alpha. \tag{4.29}$$

This is done for each possible value ζ_{assu} of ζ_{true}. Thus, ζ_{assu} is the assumed true value. ζ_{meas} denotes the outcome of the experiment that wants to measure ζ_{true}; hence ζ_{meas} can be understood as the estimate of ζ_{true}. Under the assumption that $\zeta_{assu} = \zeta_{true}$ and by construction, $c(\zeta_{assu})$ is an interval such that the probability that the estimator ζ_{meas} is realised within $c(\zeta_{assu})$ equals $1 - \alpha$. This is different from equation 4.24 where the interval 4.23 was the random variable. Here the estimator is the random variable.

The construction of $c(\zeta_{assu})$ is done by assuming a value for ζ_{true} and fixing this value in the first place. Let us denote the fixed value as ζ_{assu} as already done before. Under the assumption that ζ_{assu} is the true value of ζ, i.e. assuming $\zeta_{assu} = \zeta_{true}$, the probability density function of ζ_{meas} is computed by a MultiSim. The inputs of the MultiSim are the constants and parameters relevant in the experiment that wants to measure ζ_{true} and their uncertainties. The outputs of the MultiSim is the pdf of ζ_{meas}, i.e. the pdf of the possible measurement results of the considered experiment under the assumption that ζ_{assu} is the true value of ζ. The pdf reflects in principle the fluctuation in the result of the measurement due to the imperfections of the experiment. For an absolute precise experiment the support of the pdf would be the set containing only ζ_{assu}. From the pdf, the interval $c(\zeta_{assu})$ is determined such that equation 4.29 is satisfied. The gained interval is drawn as horizontal line with ordinate ζ_{assu} into a graph like figure 4.2. If ζ_{assu} was fixed for instance to 5, then the interval would be drawn at the ordinate $\zeta_{assu} = 5$.

In principle, this has to be repeated for every value of ζ_{assu}. In practice, this is done only for some values. Normally, the chosen values for ζ_{assu} are equidistantly distributed over the region around the maximum likelihood point estimate ζ_{meas} of the real experiment. After having constructed all intervals, a belt is rendered which could look similar to figure 4.2.

In a second step, the value ζ_{meas} of the measurand that was measured by the real experiment is considered. The final confidence set C is the set of all values of ζ_{assu} whose corresponding intervals constructed in the first step contain ζ_{meas}:

$$C(\zeta_{meas}) := \cup\{\zeta_{assu} | \zeta_{meas} \in c(\zeta_{assu})\}. \tag{4.30}$$

Note that $C(\zeta_{meas})$ is an interval satisfying equation 4.24 while the $c(\zeta_{assu})$ satisfy equation 4.29.

Graphically the final confidence set can be determined as the projection of the intersection set of the belt in figure 4.2 and the dashed line in figure 4.2 onto the ordinate.

It can be proven by elementary set theory that if 4.29 is satisfied for all ζ_{assu} also equation 4.24 is satisfied. For this, the following definition and lemma are needed:

Definition: (4.31)

Let $T \subset A \times B$ be a relation on two arbitrary sets A, B. Let $(a, b) \in A \times B$. Let aTb denote the common relation notation, i.e. $aTb := (a, b) \in T$. The slice through T at $a_0 \in A$ is defined as

$${}_{a_0}T := \{b \in B | a_0 T b\} \tag{4.32}$$

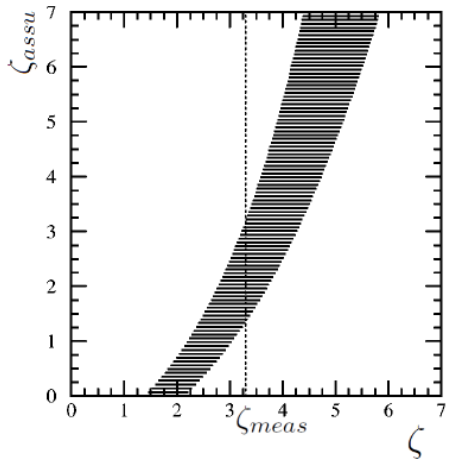

Figure 4.2: Example of a constructed confidence belt. The ordinate shows the assumed values for the measurand. The abscissa shows the measured values of the measurand. For each assumed value of the measurand the horizontal line at this value represents the $1-\alpha$ confidence interval constructed for this value as described in the text. The vertical dashed line is located at the value of the measurand that was measured in the real experiment. [61, p. 3875]

and the slice through T at $b_0 \in B$ is defined as

$$T_{b_0} := \{a \in A | aTb_0\} \tag{4.33}$$

■

Preliminary Lemma: (4.34)

With definition 4.31 it holds that

$$b_0 \in {}_{a_0}T \Leftrightarrow a_0 \in T_{b_0}. \tag{4.35}$$

PROOF:

$$b_0 \in {}_{a_0}T \Leftrightarrow b_0 \in \{b \in B | a_0Tb\} \Leftrightarrow a_0Tb_0 \Leftrightarrow a_0 \in \{a \in A | aTb_0\} \Leftrightarrow a_0 \in T_{b_0} \tag{4.36}$$

□

Theorem: (4.37)

Let $C(\zeta_{meas}) \neq \emptyset$. In the confidence belt approach it holds for all ζ_{meas} that

$$P(\zeta_{meas} \in c(\zeta_{assu})) = 1-\alpha \;\forall\; \zeta_{assu} \Leftrightarrow P(\zeta_{assu} \in C(\zeta_{meas})) = 1-\alpha \tag{4.38}$$

is satisfied.
PROOF:

Define the relation T by

$$(\zeta_{meas}, \zeta_{assu}) \in T :\Leftrightarrow \exists\ \zeta_{meas} \text{ such that } \zeta_{assu} \in C(\zeta_{meas}) \tag{4.39}$$

Let ${}_{a_0}T = C(\zeta_{meas})$ be the final confidence set. Thereby $a_0 = \zeta_{meas}$. Let further be $T_{b_0} = c(\zeta_{assu})$ and thereby $b_0 = \zeta_{assu}$. Now, from 4.34 it follows that

$$\zeta_{assu} \in C(\zeta_{meas}) \Leftrightarrow \zeta_{meas} \in c(\zeta_{assu}) \tag{4.40}$$

If $C(\zeta_{meas}) \neq \emptyset$, at least one ζ_{assu} exist which satisfies the left hand side of equivalence 4.40. Now it holds (cf. equation 4.29) that

$$1 - \alpha = P(\zeta_{meas} \in c(\zeta_{assu})) \qquad \forall \zeta_{assu} \tag{4.41}$$

by construction of $c(\zeta_{assu})$. Thus, by equivalence 4.40 it follows that

$$1 - \alpha = P(\zeta_{assu} \in C(\zeta_{meas})). \tag{4.42}$$

Since ζ_{meas} was arbitrary equation 4.42 holds for all ζ_{meas}.

□

Recalling that here $C(\zeta_{meas})$ is the random variable, it holds that the final confidence interval $C(\zeta_{meas})$ covers the true value of ζ with the desired confidence level $1 - \alpha$. Thus, by the last construction step the desired confidence interval for the true parameter is gained, while in the first step only intervals which include the outcome of the experiment with probability $1 - \alpha$ where constructed.

To get a higher precision in the final confidence set construction, the method of finding all intervals containing ζ_{meas} is changed. Instead, an interpolation function between the upper bounds of all intervals $\bar{l}(\zeta)$ and an interpolation function between the lower bounds of all intervals $\underline{l}(\zeta)$ is computed and the final confidence set is defined as

$$[\bar{l}(\zeta_{meas}); \underline{l}(\zeta_{meas})]. \tag{4.43}$$

Typically a linear spline is used for the interpolation. In principle it is possible that the interpolation is not a function. This is the case if the values of the upper (lower) bounds are not increasing with the measurand due to a random fluctuation in the simulation. In this case $\bar{l}$ and $\underline{l}$ can be understood as proper relations. Then $\bar{l}(\zeta_{meas})$ ($\underline{l}(\zeta_{meas})$) is the set of all values being in relation with ζ_{meas} by relation $\bar{l}$ ($\underline{l}$). The final confidence interval is then given as

$$C_{pol} := [\min \bar{l}(\zeta_{meas}); \max \underline{l}(\zeta_{meas})]. \tag{4.44}$$

This interval always contains the set constructed in equation 4.30. Hence, the coverage of the constructed interval is a bit larger than the aimed confidence level, but C_{pol} still satisfies equation 4.22.

It is possible to replace the measurand by a different variable which is dependent on the measurand. The equations in this subsection can for such case remain in their stated form.

4.4.2.1 The ordering principle of Feldman-Cousins

As described in subsection 4.4.2, an ambiguity in choosing a confidence interval for a given confidence level exists, since several intervals can cover the true value of the measurand with the same probability. This ambiguity still exists, even when the minimality of the confidence interval in equation 4.24 is requested[3]. The ordering principle of **F**eldman-**C**ousins (FC) [61] is a popular algorithm in neutrino physics that provides for every given confidence level precisely one confidence set. In contrast to the confidence intervals stated in subsection 4.4.2, the FC confidence interval accounts for the existence of physical boundaries of the measurand. It provides always a none empty final set even if the measurand is in an unphysical region. It decides between a central and limit confidence interval depending on the realisation of the measurand. As we later see, it has these advantages for the price of incorrect coverage.

4.4.2.1.1 Construction Like the classical confidence interval construction, the FC confidence interval construction starts with the probability density function of the estimator for an assumed true value ζ_{assu} of the measurand. Although the original method of FC is developed for statistical probability density functions only, the method is also applicable if systematic uncertainties are incorporated in the density function [62]. In contrast to the classical confidence intervals, the density function is not directly used but is modified to the rank function. The rank function R is given as

$$R(\zeta(x)|\zeta_{assu}) := \frac{p(\zeta(x)|\zeta_{assu})}{\sup_{\widetilde{\zeta}\in Z_{p.a.}} p\left(\zeta(x)\left|\widetilde{\zeta}\right.\right)} \tag{4.45}$$

where ζ_{assu} is the (assumed) true value of the physical parameter that gives a prediction on the value of the measurand, x is the realisation of the measurand, $\zeta(x)$ is the physical parameter corresponding to x, $p(\bullet|\zeta_{assu})$ is the probability density function of ζ and $Z_{p.a.}$ is the set of all **p**hysically **a**llowed values of the parameter, i.e. $\zeta_{assu} \in Z_{p.a.}$ is required by physical reasons. The value of $\widetilde{\zeta}$ that maximises the denominator in equation 4.45 is denoted by $\zeta_{best} = \zeta_{best}(\zeta(x))$. Thus equation 4.45 can be rewritten as

$$R(\zeta(x)|\zeta_{assu}) := \frac{p(\zeta(x)|\zeta_{assu})}{p(\zeta(x)|\zeta_{best}(\zeta(x)))} \tag{4.46}$$

Again, ζ is also called measurand although only x can be measured directly. In the notation of subsection 4.4.2 the intervals of the first step can be computed as the intervals $c_{FC}(\zeta_{assu})$ that satisfy

$$P(\zeta \in c_{FC}(\zeta_{assu})) \geq 1-\alpha \tag{4.47}$$

and

$$\inf_{\zeta\in c_{FC}(\zeta_{assu})} R(\zeta(x)|\zeta_{assu}) \geq \sup_{\zeta\notin c_{FC}(\zeta_{assu})} R(\zeta(x)|\zeta_{assu}). \tag{4.48}$$

This means that the interval consists of the union of all points for with the rank function anticipates their highest values such that the probability of this union equals $1-\alpha$ or greater with respect to the pdf $p(\bullet|\zeta_{assu})$.

[3] There are several minimal confidence intervals, but not the minimal confidence interval. Nevertheless, the minimal central/upper/lower confidence intervals exist.

The final confidence interval is then again computed as the union of all assumed true values ζ_{assu} whose associated intervals contain the measured value ζ_{meas} of the real experiment:

$$C^*_{FC}(\zeta_{meas}(x)) := \cup\{\zeta_{assu}|\zeta_{meas} \in c_{FC}(\zeta_{assu})\} \tag{4.49}$$

If $\text{dist}(C^*_{FC}(\zeta_{meas}); Z^{\complement}_{p.a.}) = 0$, i.e. if the confidence interval reaches the unphysical region, a one-sided confidence interval is rendered by setting

$$C_{FC}(\zeta_{meas}) = C^*_{FC}(\zeta_{meas}) \cup \{\zeta \in Z^{\complement}_{p.a.}|\zeta \leq \inf Z_{p.a.}\} \tag{4.50a}$$

or by setting

$$C_{FC}(\zeta_{meas}) = C^*_{FC}(\zeta_{meas}) \cup \{\zeta \in Z^{\complement}_{p.a.}|\zeta \geq \sup Z_{p.a.}\} \tag{4.50b}$$

depending on which physical boundary is encountered; otherwise

$$C_{FC}(\zeta_{meas}) = C^*_{FC}(\zeta_{meas}). \tag{4.50c}$$

The remarks on the numerical computation of the final confidence interval made at the end of subsection 4.4.2 are applicable to the FC confidence intervals as well.

In principle, the construction of a FC confidence interval is also applicable for more than one parameter. The equations remain the same, only ζ_{assu} has to be replaced by a tuple $(\zeta^{(1)}_{assu}, ..., \zeta^{(n)}_{assu})$, $n \in \mathbb{N}$. The final confidence set is an n-dimensional set, though.

4.4.2.1.2 Physical Meaningful Confidence Intervals The ordering principle of Feldman Cousins is designed to solve the common problem of gaining an empty confidence interval if the measured value of the measurand lies in or close to an unphysical region. This is in figure 4.2 the case for a measured value of 1.4 or less. Due to equation 4.46 a FC confidence belt extends further to $\pm\infty$ than a classical belt and shall provide a non-empty final confidence interval.

While it has already been shown that the ordering principle of FC does not provide non-empty confidence sets in general [63] it seem that it has yet not been proven that the ordering principle of FC always succeeds in providing a non-empty interval under very weak assumptions. This proof shall be given here.

Definition: (4.51)

We use the notation of this subsection. If $p(\zeta|\zeta_{assu}) = 0 \; \forall \zeta_{assu} \in Z_{p.a.}$ we define

$$0 = R(\zeta|\zeta_{assu}) = \frac{p(\zeta|\zeta_{assu})}{p(\zeta|\zeta_{best}(\zeta))} = \frac{0}{0} \tag{4.52}$$

■

This definition coincides with intuition: the value ζ has a priori zero probability and hence should never be in any confidence set.

Definition: (4.53)

We define the set of all possible outcomes of ζ_{meas} as $\mathbb{D}$.

■

Theorem: (4.54)

We use the notation of this subsection. If

$$\forall\ \zeta_{meas} \in \mathbb{D}\ \ \exists\ \zeta \in Z_{p.a.} : \zeta_{meas} \in \text{supp}(p(\bullet|\zeta)) \tag{4.55}$$

holds, then it also holds that

$$C_{FC}(\zeta_{meas}(x)) \neq \emptyset \quad \forall\ \zeta_{meas} \in \mathbb{D} \tag{4.56}$$

and that

$$\zeta_{best}(\zeta_{meas}) \in C_{FC}(\zeta_{meas}) \quad \forall\ \zeta_{meas} \in \mathbb{D}. \tag{4.57}$$

PROOF:

$$\begin{aligned} & C_{FC}(\zeta_{meas}(x)) \neq \emptyset \quad \forall\ \zeta_{meas} \in \mathbb{D} \\ \Leftrightarrow & \forall\ \zeta_{meas} \in \mathbb{D}\ \exists\ \zeta_{assu} \in Z_{p.a.} : R(\zeta_{meas}|\zeta_{assu}) \geq R(\zeta|\zeta_{assu}) \quad \forall \zeta \in \mathbb{D} \end{aligned} \tag{4.58}$$

Claim: $\zeta_{assu} = \zeta_{best}(\zeta_{meas})$
To show:

$$\begin{aligned} & R(\zeta_{meas}|\zeta_{best}(\zeta_{meas})) \geq R(\zeta|\zeta_{best}(\zeta_{meas})) \quad \forall \zeta \in \mathbb{D} \\ \Leftrightarrow\ & \frac{p(\zeta_{meas}|\zeta_{best}(\zeta_{meas}))}{p(\zeta_{meas}|\zeta_{best}(\zeta_{meas}))} \geq \frac{p(\zeta|\zeta_{best}(\zeta_{meas}))}{p(\zeta|\zeta_{best}(\zeta))} \quad \forall \zeta \in \mathbb{D} && (4.59) \\ \underset{(4.55)}{\Leftrightarrow}\ & 1 \geq \frac{p(\zeta|\zeta_{best}(\zeta_{meas}))}{p(\zeta|\zeta_{best}(\zeta))} \quad \forall \zeta \in \mathbb{D} && (4.60) \end{aligned}$$

But $p(\zeta|\zeta') \leq p(\zeta|\zeta_{best}(\zeta))\ \forall \zeta \in \mathbb{D}, \zeta' \in Z_{p.a.}$ holds by definition of ζ_{best} (cf. equations 4.45 and 4.46). Hence

$$\zeta_{meas} \in c_{FC}(\zeta_{assu} = \zeta_{best}(\zeta_{meas})) \tag{4.61}$$

and by equation 4.49 it follows that

$$\zeta_{best}(\zeta_{meas}) \in C_{FC}(\zeta_{meas}) \neq \emptyset. \tag{4.62}$$

□

Without assumption 4.55 it might be possible that $p(\zeta_{meas}|\zeta) = 0\ \forall \zeta \in Z_{p.a.}$ and by definition 4.51 $R(\zeta_{meas}|\zeta_{best}(\zeta_{meas})) = 0$.

Corollary: (4.63)

For the common case of Gaussian and Poisson distributions, the FC approach always gives a non-empty confidence set.
PROOF:
Both distribution have maximal support, thus theorem 4.54 is applicable.

□

The last result can also be shown directly from the probability density functions. This is done in appendix A.

For a physical meaningful confidence interval, it is essential that the final confidence region always includes the measured value of the measurand. For an unphysical measured value of the measurand it is additionally important that the final confidence region includes the (nearest) physical boundary. Under slightly stronger assumptions compared to theorem 4.54 this properties can be proven for the ordering principle of Feldman-Cousins:

Lemma: (4.64)

We use the notation of this subsection. W.l.o.g. the physical allowed set $Z_{p.a.}$ has a lower boundary. Let $\inf Z_{p.a.} =: \zeta_{bound}$. Let further

$$\forall\, \zeta_{meas} \in \mathbb{D} \;\; \exists\, \zeta \in Z_{p.a.} : \zeta_{meas} \in \mathrm{supp}(p(\bullet|\zeta)) \tag{4.65}$$

and let

$$\zeta_{best}(\zeta) = \zeta_{bound} \;\forall \zeta \notin Z_{p.a.} \tag{4.66}$$
$$\zeta_{best}(\zeta) = \zeta \qquad \forall \zeta \in Z_{p.a.} \tag{4.67}$$

hold. Then

$$\zeta_{meas} \in C_{FC}(\zeta_{meas}) \;\forall \zeta_{meas} \in \mathbb{D} \tag{4.68}$$
$$\zeta_{bound} \in C_{FC}(\zeta_{meas}) \;\forall \zeta_{meas} \notin Z_{p.a.} \tag{4.69}$$

hold.
PROOF:
Due to 4.65 theorem 4.54 holds and by this proposition 4.57 holds. Now claim 4.69 follows directly from 4.57 when looking at 4.66. Additionally, claim 4.68 follows for all $\zeta_{meas} \in Z_{p.a.}$ directly from 4.57 when looking at 4.67. It is still to show that 4.68 holds for all $\zeta_{meas} \notin Z_{p.a.}$: Since 4.69 has already been proven, it holds that $\mathrm{dist}(C_{FC}(\zeta_{meas}); Z_{p.a.}^{\complement}) = 0$. Hence, construction step 4.50a is performed and claim 4.68 holds in general.

□

The abstract assumptions of lemma 4.64 can be expressed in a more convenient way:

Corollary: (4.70)

Let $p(\bullet|\zeta_{assu})$ be the probability density function of ζ such that

$$\mathrm{supp}(p(\bullet|\zeta_{assu})) = \mathbb{D} \qquad \forall \zeta_{assu} \in Z_{p.a.} \tag{4.71}$$
$$\sup_{\zeta \in \mathbb{D}} p(\zeta|\zeta_{assu}) = \text{const.} \qquad \forall \zeta_{assu} \in Z_{p.a.} \tag{4.72}$$
$$\sup_{\zeta \in \mathbb{D}} p(\zeta|\zeta_{assu}) = p(\zeta_{assu}|\zeta_{assu}) \;\forall \zeta_{assu} \in Z_{p.a.} \tag{4.73}$$

$$p(\zeta|\zeta_{assu}) \text{ strictly monotonically increasing for } \zeta \leq \zeta_{assu} \tag{4.74}$$
$$p(\zeta|\zeta_{assu}) \text{ strictly monotonically decreasing for } \zeta \geq \zeta_{assu} \tag{4.75}$$

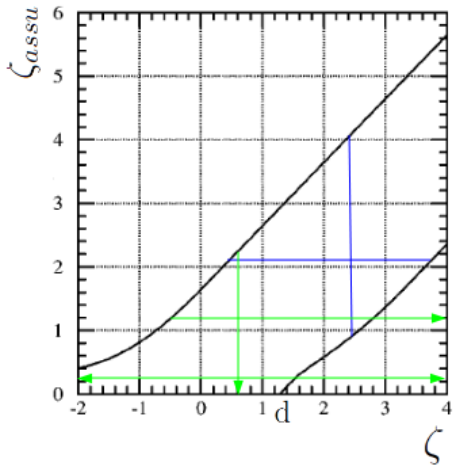

Figure 4.3: Example of an FC confidence belt. The ordinate shows the assumed values for the measurand. The abscissa shows the measured values of the measurand. The confidence intervals denoted by blue solid lines have by construction the same probability. The green confidence intervals have in general pairwise different probabilities as explained in the text below. [61, p. 3885]

Then 4.68 and 4.69 also hold.
PROOF:
From 4.71 follows 4.65. From 4.72 and 4.73 follow 4.67. From 4.74 and 4.75, respectively, follow 4.66 since for $|\zeta - \zeta_{assu}| \to 0$ follows $p(\zeta|\zeta_{assu}) \to \sup\{p(\zeta|\zeta_{assu})\,|\zeta \in \mathbb{D}\}$ for $\inf Z_{p.a.} \neq -\infty$ and $\sup Z_{p.a.} \neq +\infty$, respectively. Thus, lemma 4.64 is applicable.

□

If 4.72 does not hold, it is possible that $p(\zeta'|\zeta') > p(\zeta|\zeta') > p(\zeta|\zeta)$ for some $\zeta, \zeta' \in Z_{p.a.}$ and hence $\zeta_{best}(\zeta) \neq \zeta$. Thus 4.67 does not hold.

By corollary 4.70 it holds that the ordering principle of Feldman-Cousins has the desired properties 4.68 and 4.69 for a normal distribution $N(\zeta_{assu}, \sigma^2)$ if σ is independent on ζ_{assu}. Otherwise it might be possible that these properties, especially for small confidence levels, do not hold.

In the Gaussian regime, instead of using the probability ratio for the rank function, it is often more convenient to use the difference in the χ^2_N between ζ_{assu} and ζ_{best} [61, p. 3885]. This is justified by equation 4.8 and will be used in the following chapters.

4.4.2.1.3 Coverage An issue arises when the final FC interval includes a physical boundary. Apparently this issue has been unrecognised in literature and shall thus be explained here.

According to the design of the FC interval, an upper limit is provided by the algorithm in the above mentioned case (cf. equation 4.50). Consider a FC confidence belt as drawn in figure 4.3. It is computed according to the FC ordering principle, thus

$$P(\zeta_{meas} \in c_{FC}(\zeta_{assu})) = 1 - \alpha \qquad \forall\ \zeta_{assu} \in Z_{p.a.}. \tag{4.76}$$

If $\zeta_{meas} \leq d$, this belt shall provide an one-sided confidence interval $C_{FC}(\zeta_{meas})$ with

$$P(\zeta_{assu} \in C_{FC}(\zeta_{meas})) \stackrel{!}{=} 1 - \alpha. \tag{4.77}$$

As a reminder, $C_{FC}(\zeta_{meas})$ denotes the final "vertical" confidence set. By construction

$$C_{FC}(\zeta_{meas}) = (-\infty; \zeta^*_{assu}] \tag{4.78}$$

for some $\zeta^*_{assu} = \zeta^*_{assu}(\zeta_{meas}) \in Z_{p.a.}$ if equation 4.50a was used. Thus,

$$P(\zeta_{assu} \in C_{FC}(\zeta_{meas})) = P(\zeta_{meas} \in c_{FC}(\zeta_{assu}) \cup \{\zeta | \zeta \geq \sup c_{FC}(\zeta_{assu})\}) > 1 - \alpha \tag{4.79}$$

according to theorem 4.37 when one uses definition 4.50a in the definition of relation 4.39 which is then used in the proof of theorem 4.37. An analogue statement is true when equation 4.50b instead of equation 4.50a was used in the construction of $C_{FC}(\zeta_{meas})$.

In figure 4.3 the vertical green arrow represents the set on the left hand side of equation 4.79 and the horizontal green arrows represent the union on the right hand side. The issue arises essentially from the fact that in equations 4.50a and 4.50b the relation necessary in lemma 4.34 gets infiltrated. If one would generalise the FC belt in the unphysical region, i.e. $\zeta_{assu} \in Z_{p.a.}$ is no longer required, intervals with correct coverage would be gained, but these intervals would include unphysical values. However, the FC approach does provide valid confidence sets with respect to equation 4.22 as it only overcovers, but not undercovers in the case of an one-sided interval.

The effect remains in a higher dimensional parameter space when at least one physical boundary is reached. However, in the Double Chooz and T2K analyses this case is not encountered for the discussed confidence levels.

Chapter 5

Oscillation Analyses

The analysis in case of a neutrino oscillation experiment is normally performed by comparing the measured number of neutrino events in the far detector with the expected number of neutrino events in the far detector. The expectation is usually based on the near detector information. Hence, a neutrino oscillation experiment is in principle a counting experiment. As the energy of the neutrinos can often be determined in the experiments, the possibility to count neutrinos in distinct classes of certain energy, called bins, is given. Since the expectation on the number of neutrino events in each bin is dependent on the oscillation parameters, the aim of the oscillation analysis can then be understood as optimising the values of the oscillation parameters such that the difference between the expectation and the measurement becomes minimal over all bins. Since some of the oscillation parameters have already been determined with sufficient precision by other experiments, it is common to fix some or all of the previously determined parameters in order to reduce the number of free variables in the optimisation. In this optimisation, uncertainties in the paramaters being used in the prediction have to be considered. Additionally, when using more than one bin, correlations between the number of events in each bin have to be taken into account.

5.1 The Analysis of the Double Chooz Experiment

The Double Chooz analysis uses 18 variable sized energy bins to measure the deficit of electron antineutrinos. As described in more detail in section 3.1, in the Double Chooz experiment the expectation of an energy dependent neutrino flux in one far detector is compared with the neutrino flux actually measured in the far detector. The expectation is currently not computed from the data of a near detector, but from thermal data of the two reactors, which are the sources of the neutrinos. The measured energy spectrum of the prompt events along with the expected contributions of signal and background events to this spectrum can be seen in figure 5.1. The best point estimate of the neutrino mixing angle of $\sin^2(2\theta_{13}) = 0.086$ [8] is determined as the particular value which minimises a certain χ^2 goodness-of-fit statistic. The utilised method for the minimisation is explained in section 4.1. Two goodness-of-fit statistics are used in the Double Chooz analysis for comparison. The first statistic is known as the

covariance approach and is given as [64, p. 6]

$$\chi^2_{covar} = \left(N_i^{meas} - \sum_{r=1}^{R} N_i^{\nu,r} \right) \times \left(M_{ij}^{reactor} + M_{ij}^{detector} + M_{ij}^{stat} + \sum_{b=1}^{B} M_{ij}^{b} \right)^{-1} \times \left(N_j^{meas} - \sum_{r=1}^{R} N_j^{\nu,r} \right)^{\mathrm{T}} . \tag{5.1}$$

Herein, $1 < i < 18$ is the index of the energy bins, N_i^{meas} is the number of measured neutrino candidates in the i^{th} energy bin, r denotes the index in the enumeration of all R nuclear fuel sources of neutrinos of both reactors (cf. subsection 3.1.1), $N_i^{\nu,r}$ denotes the number of neutrino events expected in the i^{th} energy bin due to source r and $1 < j < 18$ is another index of the energy bins. As N_i and N_j, respectively, are 18 dimensional vectors, the M_{ij} (with all different superscripts) are 18×18 dimensional matrices, with $b \in B$ being an index numbering all sources of backgrounds. This goodness-of-fit statistic is a generalisation of Neyman's χ^2 goodness-of-fit test statistic given in equation 4.3. The sum in equation 4.3 is implicitly contained in the matrix product in equation 5.1 and the term $\frac{1}{O_k}$ in equation 4.3 is generalised in equation 5.1 by the inverse sum of the matrices. This will be explained in detail in the following subsections. However, the general idea is that the matrices represent different sources of statistical fluctuations in the frequencies in each bin. Each fluctuation is assumed to be Gaussian distributed and the entries in the matrices are then given as the variances (main diagonal) and covariances (off diagonal) of this particular Gaussian distributions.

The second χ^2 goodness-of-fit statistic in the Double Chooz analysis is known as pulls approach and is given as [64, p. 6]

$$\begin{aligned}\chi^2_{pulls} = &\left(N_i^{meas} - \left(\sum_{r=1}^{R} N_i^{\nu,r} + \sum_{b=1}^{B} N_i^{b}(P_b) \right) \right) \times \left(M_{ij}^{reactors} + M_{ij}^{stat} \right)^{-1} \\ &\times \left(N_j^{meas} - \left(\sum_{r=1}^{R} N_j^{\nu,r} + \sum_{b=1}^{B} N_j^{b}(P_b) \right) \right)^{\mathrm{T}} \\ &+ \sum_{b=1}^{B} \frac{(P_b)^2}{\sigma_b^2} \\ &+ \left(P_\alpha - P_\alpha^{CenVal} \right) \times \left(M_{\alpha\beta}^{detector*} \right)^{-1} \times \left(P_\beta - P_\beta^{CenVal} \right)^{\mathrm{T}} .\end{aligned} \tag{5.2}$$

In this equation, the nomenclature of equation 5.1 is kept. Additionally, N_i^b represents the number of expected events of background b in the measurement. In the pulls approach, the numbers N_i^b are dependent on pulls P_b (e.g. the rate of background events of type b) which themselves are present in the χ^2_{pulls} statistic as penalty terms. These pulls are fitted simultaneously with the mixing angle in order to compute the minimal χ^2_{pulls}. The pulls are assumed as random variables and to be Gaussian distributed with mean P_b and variance σ_b^2. The variance is present as denominator in the according penalty term.

The last term in equation 5.2 consists of pulls P_α of the parameters of the later explained energy scale correction function. The P_α^{CenVal} refer to the central values of this parameters or the pre-fitting-values. $M_{ij}^{detector*}$ is a different detector covariance matrix as in equation

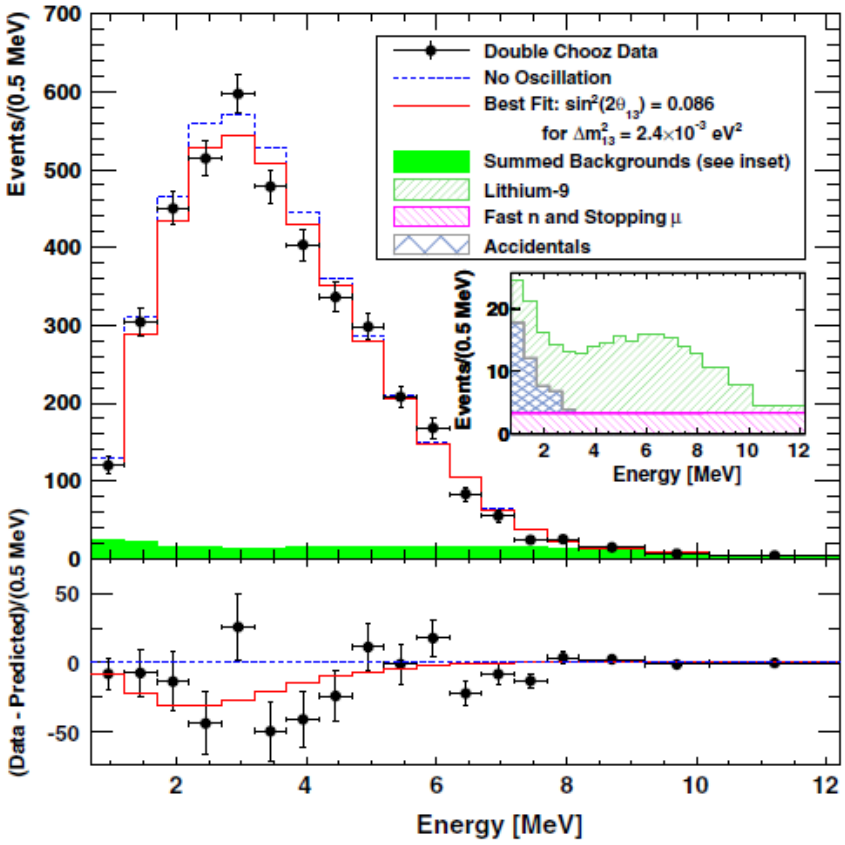

Figure 5.1: Top: Measured prompt energy spectrum of the Double Chooz experiment. Apart from the data points the expected contributions to these data points from the signal and the backgrounds are plotted. The post fitting values for signal and backgrounds are used. Additionally the expected spectrum for no oscillation is given. Inset: Detailed view of the backgrounds in the top figure as stacked diagram. Bottom: Difference between data/no oscillation and additionally between signal expectation/no oscillation. [8, p. 6]

5.1, as it now contains the covariances with respect to the parameters of the energy correction function.

It is provable that the two χ^2 statistics give the same point estimator for θ_{13} as done in [65, p. 12].

Apart from getting a point estimate on $\sin^2(2\theta_{13})$, the χ^2 statistics are used for the construction of a first confidence interval as described in subsection 4.4.1. The result of this method is $\sin^2(2\theta_{13}) = 0.086 \pm 0.071$. The range of the interval is broken up into a statistical and a systematical contribution. This is done by repeating the analysis with the data sample enlarged by the factor of 100. The thereby rendered interval of $\sin^2(2\theta_{13}) = 0.086 \pm 0.030$ is assumed to be only caused by systematic effects. The final result is thus stated as [8]

$$\sin^2(2\theta_{13}) = 0.086 \pm 0.041(stat.) \pm 0.030(sys.). \tag{5.3}$$

The evaluation of the pulls approach statistic yields [64, p. 38] $\sin^2(2\theta_{13}) = 0.085 \pm 0.050$.

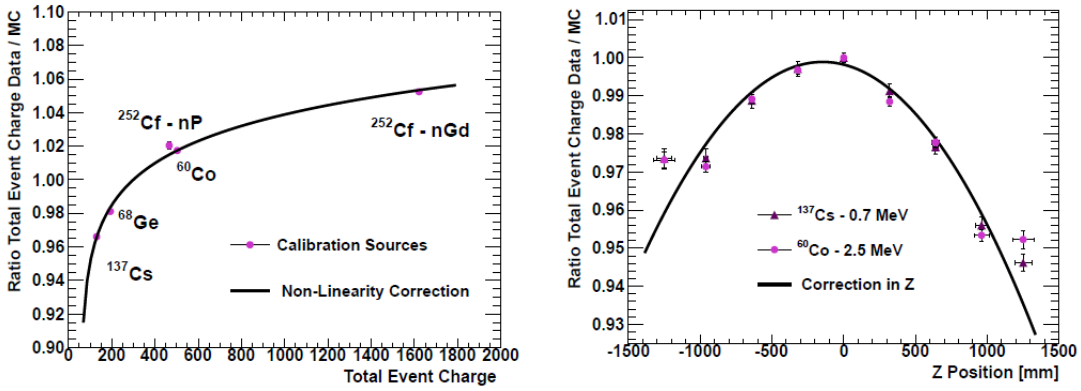

(a) (b)

Figure 5.2: The two applied energy correction functions. In figure (a) the fitted correction function along with the data points is drawn. While on the ordinate the ratio of measured to simulated energy is given, the abscissa shows the total event charge which is a prestage of the true energy in the analysis. The calibration sources are labeled by their chemical symbol. For neutron emitters, the type of capture is denoted by nH for Hydrogen capture and nGd for Gadolinium capture [64, p. 8]. In figure (b) the correction function and data points of the position dependent measurement is given. The ordinate is similar to (a). The abscissa shows the axial distance to the centre line of the cylindrical detector volume. [64, p. 9]

5.1.1 Detector Covariance Matrix

The detector covariance matrix accounts for discrepancies in the energy scale of the detector. Due to an incomplete optical simulation of the detector, discrepancies between the expected energy depositions and the measured energy depositions of several events occur. This is measured by inserting radioactive sources with a known energy spectrum into the detector and comparing the measured spectra with the simulated ones. Several sources with different energies are inserted at several positions. Instead of fine tuning the parameters of the simulation, an empirical correction function with respect to the true energy and a second correction function with respect to the position are applied. The function correcting the energy dependent discrepancies is [66, p. 11]

$$cor_E(E) = 0.0287 \cdot ln(E - 56.1478) + 0.8423, \tag{5.4}$$

where the energy E is expressed in **p**hoto**e**lectrons (PE). The function correcting for the discrepancies due to the position of the events is [66, p. 6]

$$cor_z(z) = 0.9982 - 9.5148 \cdot 10^{-6} \cdot z - 3.2598 \cdot 10^{-8} \cdot z^2. \tag{5.5}$$

In this function, z refers to the vertical distance from the centre of the cylindrical detector volume and is given in millimeters. The functional forms are motivated by the origin of the discrepancies which are essentially not simulated reflexions, but are empirical. The graphs of these functions can be seen in figure 5.2. The numbers in the functions are gained by performing a χ^2 minimisation according to equation 4.3. The Minuit program is again used for the fit as described in 4.1. The used variances are also drawn at each data point in figure

5.2. Along with the numbers, uncertainties of the parameters and correlations between the parameters are provided. The parameters of the two functions are assumed uncorrelated since the first correction accounts for energy dependent effects and the second correction accounts for position dependent effects. The covariance matrix of the two fits is thus a 6×6 block diagonal matrix and reads as [64, p. 10]

$$\widetilde{M}_{Par}^{Det} = \begin{pmatrix} 2.56 \cdot 10^{-6} & -0.02 & -1.98 \cdot 10^{-5} & & & \\ & 1.02 \cdot 10^{2} & 0.10 & & & \\ & & 1.10 \cdot 10^{-4} & & & \\ & & & 8.40 \cdot 10^{-7} & -2.65 \cdot 10^{-11} & -1.29 \cdot 10^{-12} \\ & & & & 1.86 \cdot 10^{-12} & 4.17 \cdot 10^{-16} \\ & & & & & 4.85 \cdot 10^{-18} \end{pmatrix} \tag{5.6}$$

This matrix is modified in order to not underestimate the uncertainties of the parameters. This is done by evaluating the value of the minimised χ^2 goodness-of-fit statistic and dividing it by its **n**umber of **d**egrees of **f**reedom (n.d.f.). The resulting number is called the reduced χ^2 and denoted as χ^2/n.d.f.. This gives for the first correction function a value of χ^2_E/n.d.f. $= 4.0$ and for the second function a value of χ^2_z/n.d.f. $= 4.9$. It is now possible to renormalise the reduced χ^2 value of both fits to precisely one by multiplying all the variances in the denominators of 4.3 by χ^2_E/n.d.f. and χ^2_z/n.d.f., respectively. A χ^2/n.d.f. of precisely one is assumed to indicate best estimated uncertainties[1]. This renormalisation also causes the entries of matrix 5.6 to be multiplied by 4.0 and 4.9, respectively. The matrix is further modified by removing all correlations between parameters and thus keeping only diagonal elements. This modification is motivated by a result [67] showing that correlations between fit parameters of an empirical fit function are unphysical and lead to spurious correlations in the later evaluated detector covariance matrix [64, p. 10]. This is visualised in figure 5.3. For this figure, the MultiSim method (cf. section 4.2) is applied to the parameters in equation 5.4 and 5.5, respectively. In the procedure, a Gaussian distribution is assumed. This procedure is done in equidistant energy (z-axis position) steps in figure 5.3a (5.3b). At each point, the derived distribution of the correction function values is plotted in grey in figure 5.3a and 5.3b. The correlations in matrix 5.6 lead to a discrepancy between the dashed black line connecting the central values of the random distributions and the fitted functions. This effect is larger for the energy dependent correction functions and thus only visible in figure 5.3a. Since the MultiSim method will later be used in the generation of the proper detector covariance matrix, the correlations in matrix 5.6 are removed by hand such that the connection line of the means coincides with the fitted function.

A last modification is made to the block of the position dependent correction function only. In figure 5.2b two data points of **co**balt (Co) and two data points of **c**ea**s**um (Cs) have large residuals. The four data points are taken at the very edge of the target volume. To cover these residuals, the variances are again increased such that the new Gaussian spread of the correction function covers this residuals. The necessary factor to achieve this is 40.

[1] This is motivated by the fact that the mean of a χ^2 distribution equals the number of degrees of freedom.

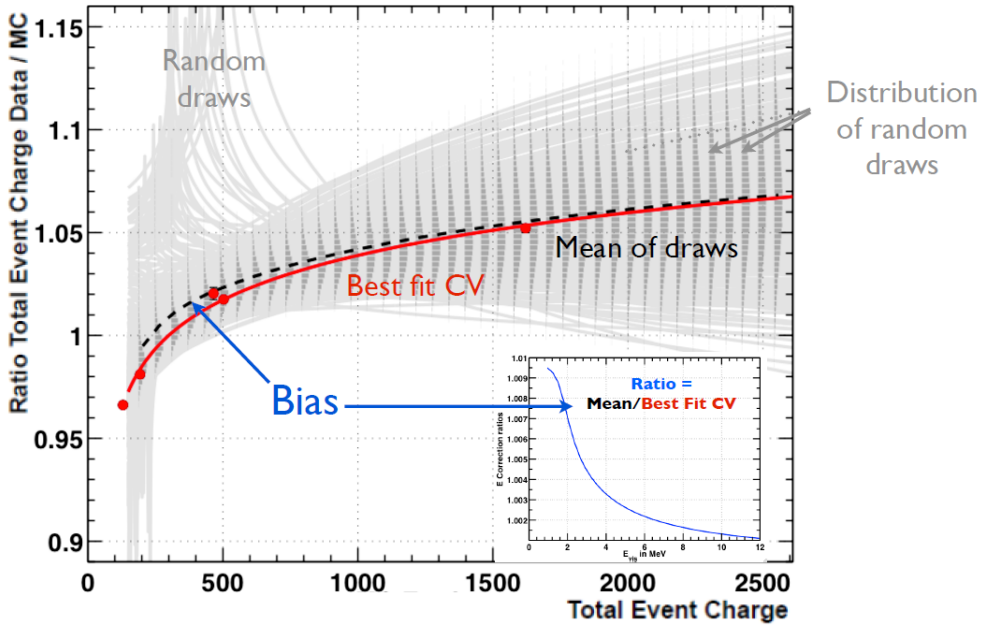

(a)

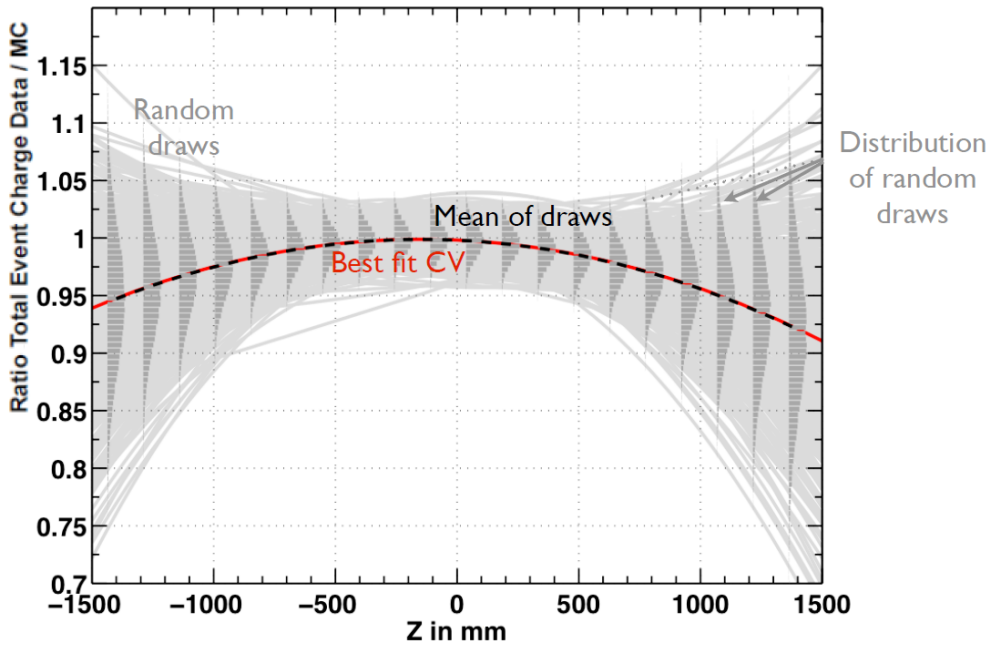

(b)

Figure 5.3: Randoms draws of the Double Chooz energy correction function parameters. In both figures the dashed black line is the connection of the means of all distributions derived as described in the text. The solid red line is the fitted function according to either equation 5.4 or 5.5. Figure (a) corresponds to the energy dependent correction function. The energy is measured in PE [67, p. 4]. Figure (b) shows the same situation for the position dependent correction function [67, p. 5].

The modified parameter covariance matrix is then [64, p. 10]

$$M_{Par}^{Det} = \begin{pmatrix} 1.03 \cdot 10^{-5} & & & & & \\ & 4.06 \cdot 10^{2} & & & & \\ & & 4.40 \cdot 10^{-4} & & & \\ & & & 1.65 \cdot 10^{-4} & & \\ & & & & 3.65 \cdot 10^{-10} & \\ & & & & & 9.50 \cdot 10^{-16} \end{pmatrix}. \tag{5.7}$$

This matrix is used directly in the pulls approach χ^2 statistics. For the covariance approach χ^2 statistic, the MultiSim method is used to generate the final covariance matrix. The input parameters are the six detector correction parameters with their uncertainties given by matrix 5.7 and the dependent variable is the number of selected neutrino events. To gain this number, for each drawn set of correction parameters a full neutrino selection from the Monte Carlo sample of all neutrino candidates is performed. The entries of the final covariance matrix are then computed as the scatter matrix entries [64, p. 12]

$$M_{ij}^{detector} = \frac{1}{N} \sum_{n=1}^{N} (\nu_i^n - \bar{\nu}_i)(\nu_j^n - \bar{\nu}_j) \tag{5.8}$$

wherein $1 \leq i \leq 18$ ($1 \leq j \leq 18$) denote the i^{th} (j^{th}) energy bin, ν_i^n the number of selected events in the i^{th} energy bin with the n^{th} set of parameters and N denotes the total number of randomly drawn parameter sets in the MultiSim method. In this case $N = 590$.

5.1.2 Reactor Covariance Matrix

The reactor covariance matrix accounts for uncertainties in the primary neutrino flux measurement based on the reactor thermal data. The expected neutrino rate in the far detector $N_{i,t}^{exp}$ in the i^{th} energy bin and at time t is calculated from different variables of the reactors as [68, p. 11]

$$N_{i,t}^{exp} = \frac{\epsilon N_p}{4\pi} \sum_{R=1}^{2} \frac{P_{th}^R(t)}{L_R^2 \langle E_f \rangle_R} \frac{\langle \sigma_f \rangle_R}{\left(\sum_k \alpha_k^R \langle \sigma_f \rangle_k\right)} \sum_k \alpha_k^R \langle \sigma_f \rangle_k^i, \tag{5.9}$$

wherein N_p is the number of protons in the detector and ϵ is the detection efficiency of the far detector. Furthermore, for each reactor R, for each isotope k and for each energy bin i, L_R denotes the baseline to the reactor, P_{th}^R the reactor thermal power, $\langle E_f \rangle_R$ the mean energy released per fission, $\langle \sigma_f \rangle_k^i$ the mean cross section per fission and α_k^R the ratio between fissions of isotope k and total fissions.

The unbinned variables are given by the weighted sums of the associated binned variables, e.g.

$$\langle \sigma_f \rangle_R = \sum_{k \in K} \alpha_k^R \sum_i \langle \sigma_f \rangle_k^i. \tag{5.10}$$

In this equation, the set $K = \{^{235}\text{U}, ^{239}\text{Pu}, ^{238}\text{U}, ^{241}\text{Pu}\}$ contains the isotopes present in the reactor cores (cf. section 3.1.1).

Since the number in each energy bin $N_{i,t}^{exp}$ is given in an analytical form, the final reactor covariance matrix $M_{ij}^{reactor}$ is rendered by the Jacobian formalism and therefore by linear uncertainty propagation. The specific parameters are treated uncorrelated such that the

final reactor covariance matrix is calculated as the sum of the covariance matrices of each uncertainty parameter U [68, p. 12]:

$$M_{ij}^{reactor} = \sum_{U} M_{ij}^{U}. \tag{5.11}$$

In the Jacobian formalism, the matrices M_{ij}^{U} are given as

$$M_{ij}^{U} = J_i^U (\sigma_U)^2 J_j^U \tag{5.12}$$

with the Jacobian

$$J_i^U = \frac{\partial N_i^{exp}}{\partial U}. \tag{5.13}$$

Some of the parameters are constant in time such that no cross terms have to be considered. An example is the number of target protons N_p. Here, the matrix is given as

$$M_{ij}^{N_p} = \left(\sum_{t,R} N_{i,t}^{R} \right) \frac{{\sigma_{N_p}}^2}{N_p} \left(\sum_{t,R} N_{j,t}^{R} \right), \tag{5.14}$$

wherein $\sigma_{N_p}^2$ represents the variance in the number of free target protons. When correlations between parameters are present, the covariance matrix of these parameters is required and the sum over all correlated parameters is used. Thus the single covariance matrix for the set of the parameters $\mathcal{U}$ is given as

$$M_{ij}^{\mathcal{U}} = \sum_{\beta,\gamma} J_i^{U_\beta} m_{\beta\gamma}^{\mathcal{U}} J_j^{U_\gamma}. \tag{5.15}$$

Herein, $m_{\beta\gamma}^{\mathcal{U}}$ is the covariance matrix of the parameters $U_\beta \in \mathcal{U}$. (In contrary, $M_{ij}^{\mathcal{U}}$ is the covariance matrix of the number of neutrinos in each energy bin, due to the set of parameters $\mathcal{U}$.) In the case of the fuel inventory numbers α_k^R, the covariance matrix $m_{\beta\gamma}^{\mathcal{A}_k^R}$ is calculated by simulating the conversion of the fuel components over time. More details on the calculations can be found elsewhere [68; 69; 70]. After calculating the covariance matrix $M_{ij}^{reactor}$ in the described way, this matrix has to be modified before it can be used in equation 5.1, since it was calculated in terms of true neutrino energy, while the measurement in the detector takes place in terms of reconstructed positron energy. The conversation is made by the MultiSim method (cf. section 4.2). The input are the numbers of events in each energy bin with respect to the true neutrino energy and the outputs are the numbers of events in each energy bin with respect to the reconstructed positron energy. The number of random draws is 180000 for this simulation. Details on the simulations can be found elsewhere [71].

5.1.3 Accidental Background Matrix

The accidental background in the Double Chooz experiment are delayed coincidences which are not caused by correlated event pairs, e.g. a radioactive decay followed by a single neutron capture is an accidental background event. The number of events is measured by using the off-time method. In this method, the number of inverse β decay signals in a series of shifted time windows is counted. While for a correct inverse β decay the on-time window is the interval $[0.002; 0.1]ms$ after the prompt signal (cf. section 3.1.3), the off-time windows are the

intervals $[n \cdot 0.5 + 0.002; n \cdot 0.5 + 0.1]ms$ with $1 < n < 200$. The remaining selection criteria for on-time selection are applied unchanged to the off-time selection. The uncertainties in this measurement are dominated by the amount of Boron contamination in the off-time windows [64, p. 20]. Due to the measured character of the accidental background, the uncertainties are treated as uncorrelated and added binwise in a diagonal matrix to the total covariance matrix.

5.1.4 ^{9}Li Background Matrix

Since the decay signals of Lithium-9 are very similar to the neutrino induced inverse β decays, Lithium-9 decays are a major contribution to the final uncertainty of the Double Chooz measurement. For the same reason, the spectrum of the Lithium-9 decays cannot be measured from the data. The spectrum is therefore simulated. The binwise uncertainties are dominated by the uncertainties in the breakup scenarios of the daughter nucleus. The uncertainties are propagated in the covariance matrix by the MultiSim method.

5.1.5 Fast Neutron and Stopped Muon Background Matrix

The amount of background events due to fast neutrons and stopping muons is determined by extrapolation. The rate of these events is determined in the energy region between 12 MeV and 30 MeV and a flat distribution is assumed. This distribution is then used in the relevant region between 0.7 MeV and 12.2 MeV. The uncertainties enter the total covariance matrix by the usage of the MultiSim method.

5.1.6 Statistical Uncertainty Matrix

The statistical uncertainties in the measurement are incorporated in the final covariance matrix in terms of a diagonal matrix. For the distribution of the statistical uncertainties, the assumption of a Poisson distribution is made. This is motivated by the counting experiment character of the Double Chooz experiment, which respects the Poisson postulates [53, p. 36]. The entries of the diagonal are thus the number of measured neutrinos. When calculating the result in equation 5.3 by enlarging the measured ensemble by a factor of 100 as described in the text before equation 5.3, the only affected matrix is the statistical uncertainty matrix. By enlarging the ensemble, the relative uncertainties in this matrix decrease by the inverse square root.

5.1.7 Computation of the Confidence Intervals

For the computation of the confidence intervals, the confidence belt approach and the ordering principle of Feldman-Cousins (cf. subsections 4.4.2 and 4.4.2.1, respectively) is used. The ordering principle is applied in terms of the $\Delta\chi^2$ criterion. The analysis uses the covariance approach statistic χ^2_{cov} defined in equation 5.1 for the computation of this variable. $\Delta\chi^2$ is given as

$$\Delta\chi^2(n|\theta_{13}^{assu}) = \chi^2_{cov}(n|\theta_{13}^{assu}) - \chi^2_{cov}(n|\theta_{13}^{best}) \tag{5.16}$$

wherein n denotes the realisation of the random variable N of measured neutrino events and θ_{13} denotes the neutrino mixing angle. Since neutrino events are counted in 18 energy bins, the random variable N is strictly speaking a vector of 18 random variables and n the vector of all 18 realisations.

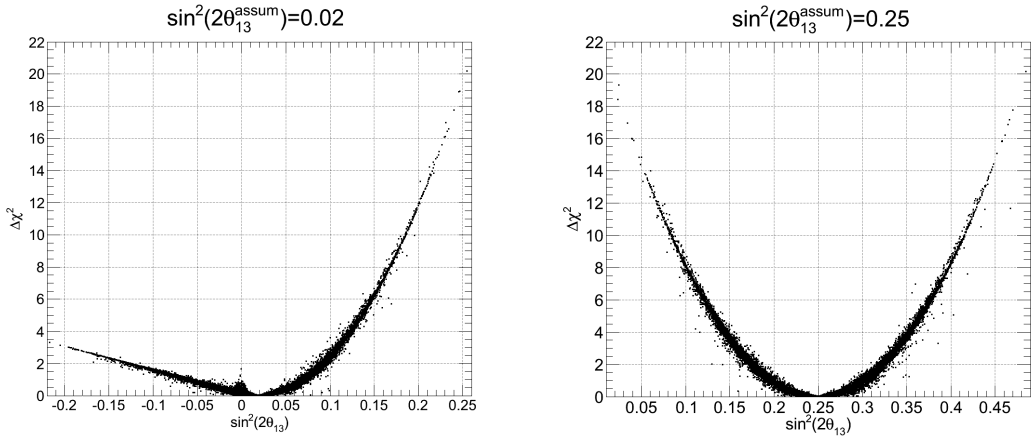

(a) (b)

Figure 5.4: Pseudo experiments in the Double Chooz confidence belt approach for (a) an assumed value of $\sin^2(2\theta_{13}^{assu}) = 0.02$ and (b) an assumed value of $\sin^2(2\theta_{13}^{assu}) = 0.25$.

For the first step of the FC confidence belt computation, a value of θ_{13} is fixed. This value will be called θ_{13}^{assu}. With this value, a high statistics sample of the expected neutrino prompt energy spectrum is generated. This sample gives the central values for the number of neutrino events in each bin. The numbers are arranged in an 18 dimensional vector $n^{assu}(\theta_{13}^{assu})$. Then the MultiSim method is applied to the spectrum: For each energy bin a random draw of the number of neutrino events is done from a standard normal distribution. Thereby a 18 dimensional vector is gained. The vector is multiplied with the total covariance matrix and added to the central value vector. The result is a modified prompt energy spectrum n with respect to the generated high statistics sample $n^{assu}(\theta_{13}^{assu})$. This modified spectrum is called a pseudo experiment. Then $\Delta\chi^2(n|\theta_{13}^{assu})$ is calculated for this pseudo experiment n. For the analysis, approximately 10^4 pseudo experiments are performed within the MultiSim method. This is done at each value of θ_{13}^{assu} considered in the analysis. The considered values are listed in table 5.1. To calculate the confidence interval for an assumed value of θ_{13}, for each pseudo experiment, performed at this assumed value, its $\Delta\chi^2$ is plotted over its $\sin^2(2\theta_{13}^{best})$. Two of this plots, generated for different θ_{13}^{assu} are given in figure 5.4. In the official analysis, a critical value $\Delta\chi^2_{crit}$ is computed such that the number of pseudo experiments with a $\Delta\chi^2$ below the critical value equals the confidence level $1-\alpha$. For numerical reasons, small overcoverage is allowed, hence:

$$\Delta\chi^2_{crit}(\theta_{13}^{assu}) = \min_{\{\widetilde{c}\in\mathbb{R}:\#\{n|\Delta\chi^2(n|\theta_{13}^{assu})\leq\widetilde{c}\}\geq 1-\alpha\}} \widetilde{c}. \tag{5.17}$$

This critical value is then translated into an interval in the $\sin^2(2\theta_{13})$ range. The lower (upper) bound of this interval is the maximal (minimal) value of all $\sin^2(2\theta_{13}^{best})$ of all pseudo experiments with its $\Delta\chi^2$ above the critical value and its $\sin^2(2\theta_{13}^{best})$ below (above) the

$\sin^2(2\theta_{13}^{assu})$												
0.00	0.03	0.05	0.08	0.10	0.12	0.15	0.17	0.19	0.20	0.21	0.22	0.25

Table 5.1: Assumed values of $\sin^2(2\theta_{13})$ in the Double Chooz confidence belt analysis.

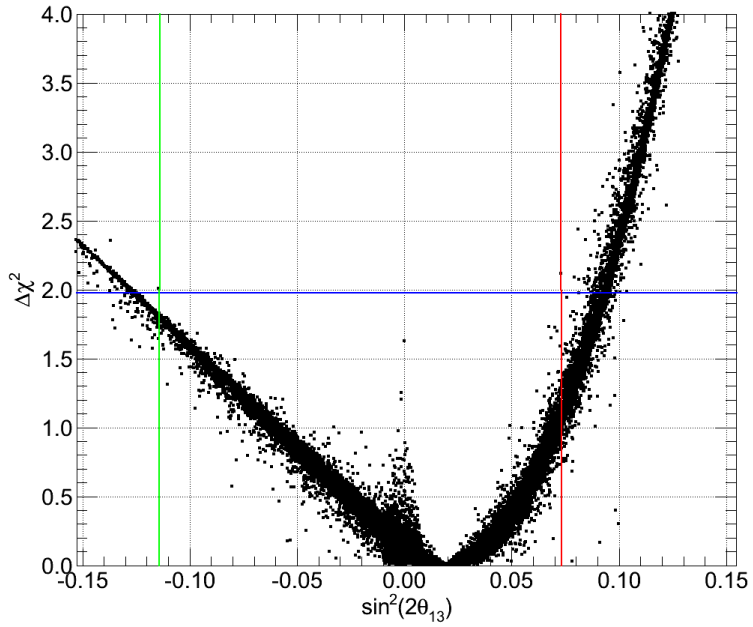

(a)

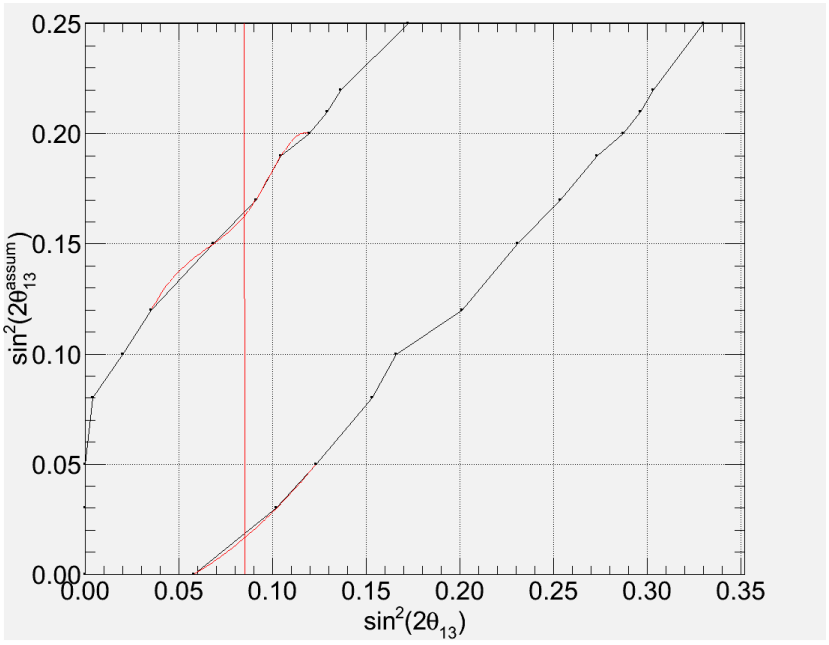

(b)

Figure 5.5: Confidence belt construction in the Double Chooz analysis. Figure (a) shows the graphical construction of the confidence interval for $\sin^2(2\theta_{13}^{assu}) = 0.02$. Figure (b) shows the official confidence belt (black) along with the official interpolation graph (red) and the measured result $\sin^2(2\theta_{13}^{meas}) = 0.086$ (vertical line).

assumed value. More precisely the interval is given as:

$$\left[\max_{\left\{\substack{n|\Delta\chi^2(n|\theta_{13}^{assu})\geq\Delta\chi^2_{crit}(\theta_{13}^{assu})\\ \wedge\sin^2(2\theta_{13}^{best})(n)\leq\sin^2(2\theta_{13}^{assu})}\right\}}\sin^2(2\theta_{13}^{best})(n);\min_{\left\{\substack{n|\Delta\chi^2(n|\theta_{13}^{assu})\geq\Delta\chi^2_{crit}(\theta_{13}^{assu})\\ \wedge\sin^2(2\theta_{13}^{best})(n)\geq\sin^2(2\theta_{13}^{assu})}\right\}}\sin^2(2\theta_{13}^{best})(n)\right] \tag{5.18}$$

In figure 5.5a the interval construction is executed graphically. This construction is executed at every value of $\sin^2(2\theta_{13}^{assu})$ listed in table 5.1. The final confidence set is then determined by interpolation between the constructed interval boundaries and finding the intersections of the interpolation functions and the measured value of $\sin^2(2\theta_{13})$ as described in subsection 4.4.2. This is graphically executed in figure 5.5b. As interpolation function a cubic spline is used [58, p. 166]. As end condition for this spline, the not-a-knot condition is used [58, p. 171]. The 90% confidence level belt is plotted in figure 5.5b along with the line representing the measured value of $\sin^2(2\theta_{13})$. Since the official belt in this figure is drawn from a linear spline interpolation, the used cubic spline interpolation function is superimposed for comparison. The resulting 90% confidence level interval is

$$\sin^2(2\theta_{13}) \in [0.017; 0.16] \quad (90\%\text{C.L.}). \tag{5.19}$$

5.1.8 Improvement of the Confidence Interval Computation

The official confidence belt construction of the Double Chooz analysis described in subsection 5.1.7 suffers from a few issues. These shall be pointed out in this subsection and possible solutions will be discussed.

A first issue is given by the choice of the interpolation method. As visible in figure 5.5b, a minor discrepancy between the two interpolation lines exist. This is especially the case for the abscissa region around the measured value of $\sin^2(2\theta_{13})$. The discrepancy is in fact significant as the confidence set, when constructed form the linear spline interpolation, reads

$$\sin^2(2\theta_{13}) \in [0.019; 0.16] \quad (90\%\text{C.L.}). \tag{5.20}$$

This issue can on the one hand be solved by choosing a different end condition. The not-a-knot condition together with the small number of interpolation points effectively neutralises the advantage of splines. Especially for the lower bound, the spline interpolation with only three points is identically to a polynomial interpolation. On the other hand, the issue can more efficiently be solved by increasing the number or better the density of $\sin^2(2\theta_{13}^{assu})$ values in this particular region. Thereby the dependencies on the interpolation method and their possible end conditions are decreased.

A different issue arises from the chosen construction method of the individual boundaries. As shown in figure 5.5a, the boundaries for the interval are depending only on the $\sin^2(2\theta_{13}^{best})$ value of two pseudo experiments. The two pseudo experiments are the outermost outliers of all the pseudo experiments with a $\Delta\chi^2$ larger than the critical one. This method is prone to statistical fluctuations on the one hand and divergent on the other hand: in a repetition of the pseudo experiment generation it is likely to have an outlier at a different position; moreover, for increasing the number of generated pseudo experiments, the probability to get an extreme outlier increases. Hence, as the number of pseudo experiments increases towards infinity, the boundaries diverge towards infinity, as well. The resulting interval is thus $[+\infty; -\infty] = \emptyset$. This issue can be solved by choosing either the average $\sin^2(2\theta_{13}^{best})$

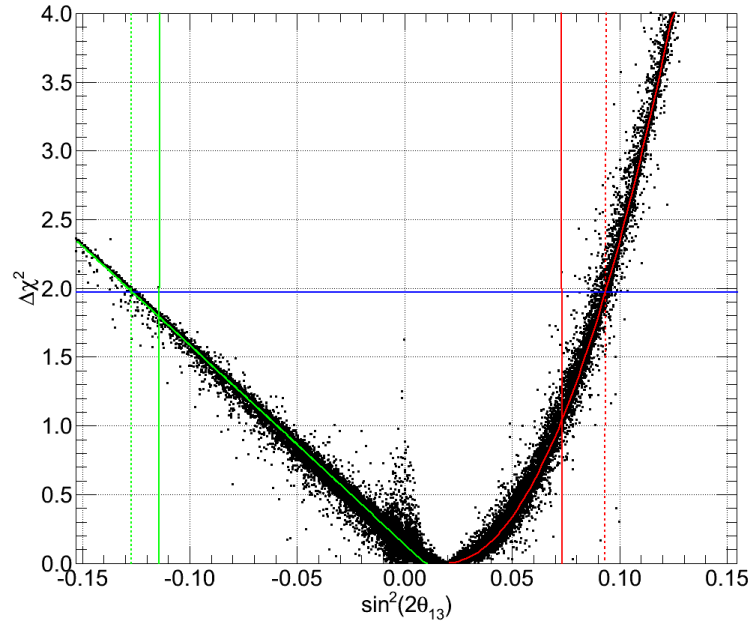

(a)

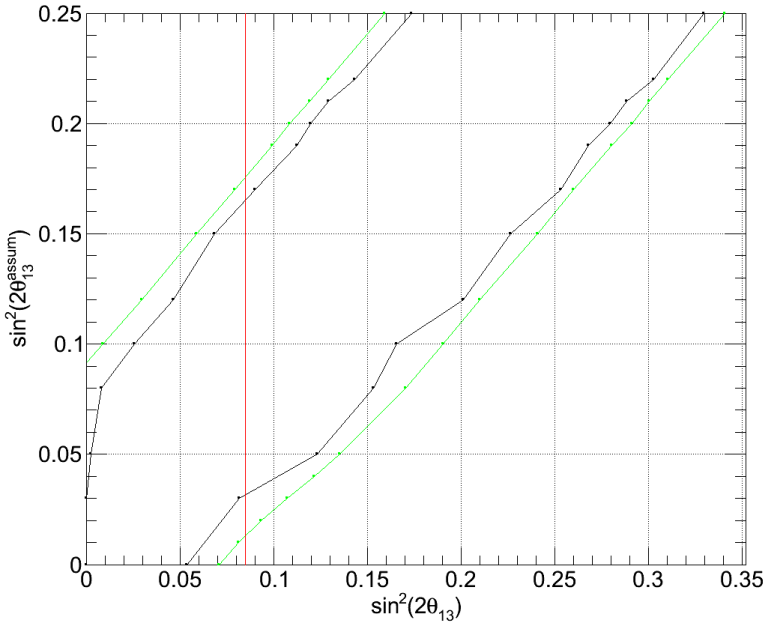

(b)

Figure 5.6: Improved confidence belt construction in the Double Chooz analysis. Figure (a) shows the graphical construction of the confidence interval for $\sin^2(2\theta_{13}^{assu}) = 0.02$. The dashed line corresponds to the fitting method as described in the text. The solid coloured graphs are the fitted functions. The official lines are copied from figure 5.5a. Figure (b) shows the confidence belt by the fitting method (green) along with the official belt (black) and the measured result $\sin^2(2\theta_{13}^{meas}) = 0.086$ (vertical line).

	left			right		
$sin^2(2\theta_{13}^{assu})$	official	average	fitting	official	average	fitting
0.00	0.000	$-\infty$[1]	$-\infty$[1]	0.058	0.071	0.071
0.01	[3]	[2]	-0.241	[3]	0.082	0.082
0.02	[3]	-0.126	-0.125	[3]	0.094	0.094
0.03	0.000	-0.086	-0.086	0.102	0.107	0.107
0.04	[3]	-0.064	-0.065	[3]	0.122	0.122
0.05	0.000	-0.048	-0.049	0.123	0.136	0.135
0.08	0.004	-0.011	-0.013	0.153	0.170	0.170
0.10	0.020	0.008	0.009	0.166	0.190	0.191
0.12	0.035	0.030	0.030	0.201	0.210	0.210
0.15	0.068	0.059	0.059	0.231	0.241	0.241
0.17	0.091	0.079	0.080	0.254	0.260	0.260
0.19	0.105	0.099	0.099	0.273	0.280	0.281
0.20	0.120	0.108	0.109	0.287	0.291	0.291
0.21	0.129	0.119	0.119	0.296	0.301	0.300
0.22	0.136	0.129	0.130	0.303	0.310	0.310
0.25	0.172	0.159	0.160	0.330	0.340	0.341
final	0.017	0.013	0.013	0.163	0.177	0.177

[1] not calculated
[2] too less data
[3] not included in official analysis

Table 5.2: Comparison of the confidence interval boundaries for the official, the average and the fitting method as described in the text.

value of all pseudo experiments around the critical $\Delta\chi^2$ value or by fitting a function to the point cluster. This is graphically executed in figure 5.6a. Two parabolic functions were chosen to approximate the χ^2 difference as a function of the $\sin^2(2\theta_{13}^{best})$ value. The support of the first function is the range above $\sin^2(2\theta_{13}^{assu})$, the support of the second function is the range below. The parabolic function is motivated by the fact that the pseudo experiments were generated according to a Gaussian distribution. The resulting horizontal confidence intervals and final vertical confidence intervals are listed in table 5.2. The average value method and the fitting method are in good agreement, while the official method is systematically off. This is also true for the final interval. For the computation of the average method and the computation of the fitting method values, a 13 times larger statistical ensemble of pseudo experiments was used and the density of simulated $\sin^2(2\theta_{13}^{assu})$ was increased around the critical lower bound region of the final interval. This can be seen in figure 5.6b and table 5.2. The result for the improved 90% confidence interval is thus

$$\sin^2(2\theta_{13}) \in [0.013; 0.177] \quad (90\%\text{C.L.}). \tag{5.21}$$

With respect to the critical lower bound of this interval, the difference between the official and the improved method is 24%.

Another method to calculate the confidence set avoids the conversation of the χ^2 difference into a $\sin^2(2\theta_{13})$ value. It compares at every $\sin^2(2\theta_{13}^{assu})$ directly the $\Delta\chi^2$ of the real data under the assumption of $\sin^2(2\theta_{13}^{assu})$ with the critical $\Delta\chi^2$ value at this $\sin^2(2\theta_{13}^{assu})$. The

results are also in agreement with this improved method.

A last issue in the pseudo experiment generation is due to some pseudo experiments having $\sin^2(2\theta_{13}^{best}) = 0$ and widely spread $\Delta\chi^2$. These experiments are visible in figure 5.6b as a dense point cluster around $\sin^2(2\theta_{13}) = 0$. They affect the official belt construction by forcing the lower bound of every horizontal interval to be at least zero (cf. figure 5.6b). This effect is not possible in the improved methods as they are no longer dependent on only one pseudo experiment. Nevertheless, these pseudo experiments can be understood as evidence for a in general not perfectly converging χ^2 minimisation. Further investigation of the numerical methods are needed to solve this issue.

5.2 The Analysis of the T2K Experiment

The T2K experiment measures the electron neutrino flux in a muon neutrino beam at two positions from the source. The details of this experiment setup were given in section 3.2. The analysis of the oscillation is performed as a pure rate analysis. This means, only one energy bin is considered. The T2K analysis relies entirely on the Feldman-Cousins confidence belt approach. The best fit value is given as the parameter configuration that explains the measured number of events in the only considered bin and no χ^2 minimisation is used.

The central variable in the confidence belt construction is the number of measured neutrinos. The belt is constructed by an augmented MultiSim method. This augmented MultiSim method starts with a default execution of the normal MultiSim process (cf. section 4.2). The output of this MultiSim is the number of expected neutrinos. The inputs are the parameters relevant for the overall T2K measurement and their uncertainties, respectively. The number of expected events in the T2K far detector $\hat{N}_{exp}$ is given as [72, p. 5]

$$\hat{N}_{exp} = \left(\frac{N^{data}_{ND280,1\mu}}{N^{MC}_{ND280,1\mu}}\right) \cdot \sum_{i \in E_{MC}} \left(\Theta_i^{cuts} \cdot \gamma_{norm}(\nu) \cdot P_{osc}(\theta_{13}, \Delta m^2, \delta_{CP}, E_\nu, \nu) \cdot \omega(E_\nu, \nu)\right) \quad (5.22)$$

with the neutrino species $\nu = \nu_\mu, \bar{\nu}_\mu, \nu_e$, the Monte Carlo normalisation factor $\gamma_{norm}(\nu)$, the oscillation probabilities $P_{osc}(\theta_{13}, \Delta m^2, \delta_{CP}, E_\nu, \nu)$, the beam tuning reweighting factor $\omega(E_\nu, \nu)$, the binary physics selection factor Θ_i^{cuts} and the near detector single muon event rates of the Monte Carlo $N^{MC}_{ND280,1\mu}$ and the data $N^{data}_{ND280,1\mu}$, respectively. The ratio of these last two rates is used for scaling purposes. The set E_{MC} is the set of all Monte Carlo events considered in the simulation of the T2K experiment. Equation 5.22 is the central equation in the MultiSim method to which random shifts are added. With these added random shifts, the equation expressing the realisation n_{exp} of the random variable of the expected number of events N_{exp} is given as [72, p.6]

$$n_{exp} = \left(1 + \delta_{near/far}(\theta_{13}, \Delta m^2, \delta_{CP})\right) \cdot \left(\frac{N^{data}_{ND280,1\mu}}{\sum_{\{m,\nu,E_\nu\}} \left(N^{MC}_{ND280,1\mu}(m, \nu, E_\nu) \cdot \prod_{j \in J}(1 + \delta_j)\right)}\right)$$
$$\cdot \sum_{i \in E_{MC}} \left(\Theta_i^{cuts} \cdot \gamma_{norm}(\nu) \cdot P_{osc}(\theta_{13}, \Delta m^2, \delta_{CP}, E_\nu, \nu) \cdot \omega(E_\nu, \nu) \cdot \prod_{k \in K}(1 + \delta_k)\right), \quad (5.23)$$

where J and K are the sets of systematic uncertainty sources of the subdetectors and the δ are random shifts in parameters of this equation. The uncertainties in the oscillation parameters

are expressed in $\delta_{near/far}$ as they directly effect the extrapolation between the two detectors. The uncertainties in the far detector parameters are given in the δ_k and the uncertainties in the near detector are given in the δ_j. A further modification between equation 5.22 and equation 5.23 has been made by binning the events of the near detector in classes of interaction mode m, neutrino type ν and energy E_ν. Hence, the uncertainty shifts are applied bin-wise to the near detector events and event-wise to the far detector events. The remaining variables are defined as for equation 5.22.

When performing the MultiSim random draws according to this equation, all errors are treated uncorrelated except the cross section uncertainties for both detectors. These are treated 100% correlated. All uncertainties are drawn from a symmetric Gaussian distribution. When an asymmetric distribution is given for an uncertainty, it is conservatively expanded to a symmetric distribution. An exception is present for the statistical uncertainties. These are drawn from a Poisson distribution. If a random shift within the MultiSim method is smaller than -100%, i.e. the parameter becomes unphysical, the shift is set to exactly -100%.

After the normal MultiSim, the gained distribution of N_{exp} is transferred into a distribution of observable neutrinos N_{obs}. This is done by taking the n_{exp} as the parameters of Poisson distributions and integrating over all n_{exp} by respecting the distribution. Hence, [72, p.9]

$$\mathcal{L}_{N_{obs}}(N) = \int_0^\infty P_{N'}(N)\mathcal{L}_{N_{exp}}(N')dN' \tag{5.24}$$

describes the probability density function of N_{obs}, wherein $P_{N'}(N)$ is the Poisson probability of observing N events when N' are expected and $\mathcal{L}_{N_{exp}}$ is the probability density function of the expected number of events N_{exp}, i.e. the output of the MultiSim.

According to the ordering principle of FC (cf. subsection 4.4.2.1) a confidence region is computed utilising the probability density function in equation 5.24. For this, a grid of 325×325 is spanned across the $\delta_{CP} - \sin^2(2\theta_{13})$ oscillation parameter plane. At each grid point the above described augmented MultiSim method is performed with an ensemble size of 5000 parameter set draws. Let N denote the random variable that expresses the number of neutrino events in such a pseudo experiment. The FC ordering ratio in the T2K analysis is given as

$$R(N|\sin^2(2\theta_{13}), \delta_{CP}) = \frac{\mathcal{L}_{N_{obs}}(N|\sin^2(2\theta_{13}), \delta_{CP})}{\mathcal{L}_{N_{obs}}(N|\sin^2(2\theta_{13}^{best}), \delta_{CP})}. \tag{5.25}$$

The value of δ_{CP} is fixed in this ratio, so only $\sin^2(2\theta_{13})$ is allowed to vary in the determination of the maximal probability. This is indicated in the denominator of equation 5.25 by the usage of the superscript "best" in analogy to equation 4.46. This approach is called the raster scan approach contrarily to the global scan approach, in which all parameters are allowed to vary. The raster scan effectively reduces the two dimensional problem to 325 one dimensional problems; one problem for each of the 325 values of δ_{CP} considered in the original grid. This approach is chosen since the T2K experiment has no real sensitivity to δ_{CP} as explained in section 2.2.

In each one dimensional problem and for each assumed value of $\sin^2(2\theta_{13})$, a confidence interval in terms of N_{obs} is calculated according to the FC ordering ratio in equation 5.25 (cf. subsection 4.4.2.1). The final one dimensional confidence interval is then gained as the union of all assumed values of $\sin^2(2\theta_{13})$ for which the according confidence intervals contain the number of measured neutrinos. This number is 6 [7]. The final confidence set of the two dimensional problem is given as the union of all final confidence intervals of the one

dimensional problems. This set is shown in figure 5.7. Two such sets are computed due to the neutrino mass hierarchy ambiguity (cf. section 2.2).

The best point estimate of $\sin^2(2\theta_{13})$ for an assumed value of δ_{CP} is derived directly from equation 5.22. The best point estimate is given as the set of oscillation parameters $(\delta_{CP}; \sin^2(2\theta_{13}))$ for which equation 5.22 becomes exactly 6. Due to the neutrino mass hierarchy ambiguity, two such sets exist. They are plotted in figure 5.7 as solid black graphs. For an assumed value of $\delta_{CP} = 0$ this value is [7]

$$\sin^2(2\theta_{13}) = 0.11 \ (0.14) \tag{5.26}$$

for normal (inverse) mass hierarchy.

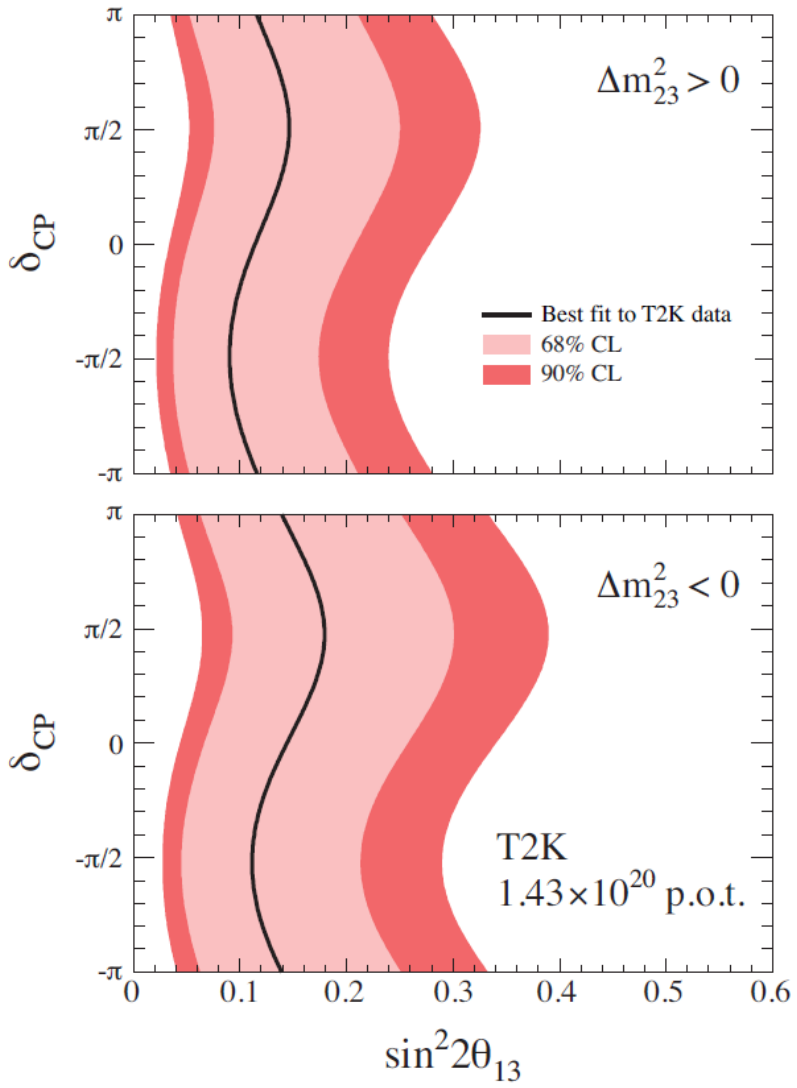

Figure 5.7: Confidence sets of the T2K experiment. The 68% (pink) and 90% (red) C.L. regions together with the best fit graph (black) is shown for normal (top) and inverted (bottom) mass hierarchy. [7, p. 7]

Chapter 6

A Joint Analysis

The combination of a reactor and an accelerator neutrino experiment offer the opportunity to gain sensitivity to oscillation parameters to which the single experiments are not sensitive. This is due to the different oscillation processes which are measured by the experiments. Both experiments are dependent on θ_{13}, but T2K has, in addition to DC, a dependency on δ_{CP} and the neutrino mass hierarchy. While T2K as a single experiment can only measure the combination of δ_{CP}, θ_{13} and the mass hierarchy, a joint analysis with a reactor experiment like DC can cancel the θ_{13} dependency in the T2K result. Thereby the joint analysis has for instance sensitivity on δ_{CP} for a fixed hierarchy scenario.

6.1 Statistical Method for a δ_{CP} Measurement

One of the parameters, which a joint analysis is sensitive to, is the charge-parity violating phase δ_{CP}. The determination is possible, since the δ_{CP} independent measurement of θ_{13} with a reactor experiment can exclude certain regions of the confidence set of an accelerator experiment at a certain confidence level. This idea is illustrated in figure 6.1. If the excluded region at this confidence level contains some values of δ_{CP} for all values of θ_{13}, a non trivial confidence set for δ_{CP} is rendered. This set will not necessarily be an interval. Assume that $\delta_{CP} = 0$, then a value of δ_{CP} around π will be equally likely. This can be seen from figure 5.7. Assuming normal hierarchy, $\delta_{CP} = 0$ yields $\sin^2(2\theta_{13}) = 0.11$, but the solid black best fit graph yields also $\delta_{CP} \approx \pi$. The second intersection point is not exactly $\delta_{CP} = \pi$, since the interference term in equation 2.12 causes the probability graphs for $\delta_{CP} = 0$ (solid black) and $\delta_{CP} = \pi$ (dotted orange) in figure 2.3a to be shifted. Nevertheless, for $\delta_{CP} = \frac{1}{2}\pi$ or $\delta_{CP} = \frac{3}{2}\pi$ only one value of $\sin^2(2\theta_{13})$ corresponds to these δ_{CP} values. Thus, an interval can be gained. The recent results of Double Chooz and T2K in figure 6.1 let the second case seem more likely.

An crucial question in the combined oscillation analysis towards the δ_{CP} measurement is the compatibility of the official Double Chooz and T2K analysis. As pointed out in chapter 5, both experiments compute their confidence sets by the confidence belt method and the ordering principle of Feldman-Cousins. Thus, the analyses are in principle compatible. Moreover, the method of FC can be adopted for a joint analysis, as will be pointed out in the following. Nevertheless, some modifications need to be made, since the exact implementation differ between both experiments.

[1] For Double Chooz, the corrected values from subsection 5.1.8 are used.

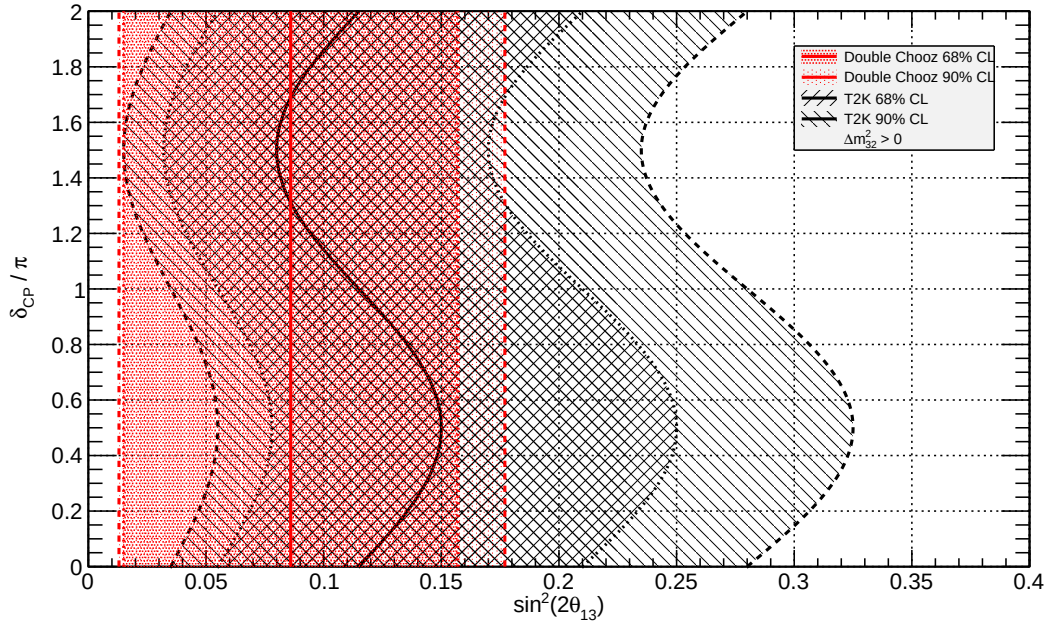

(a)

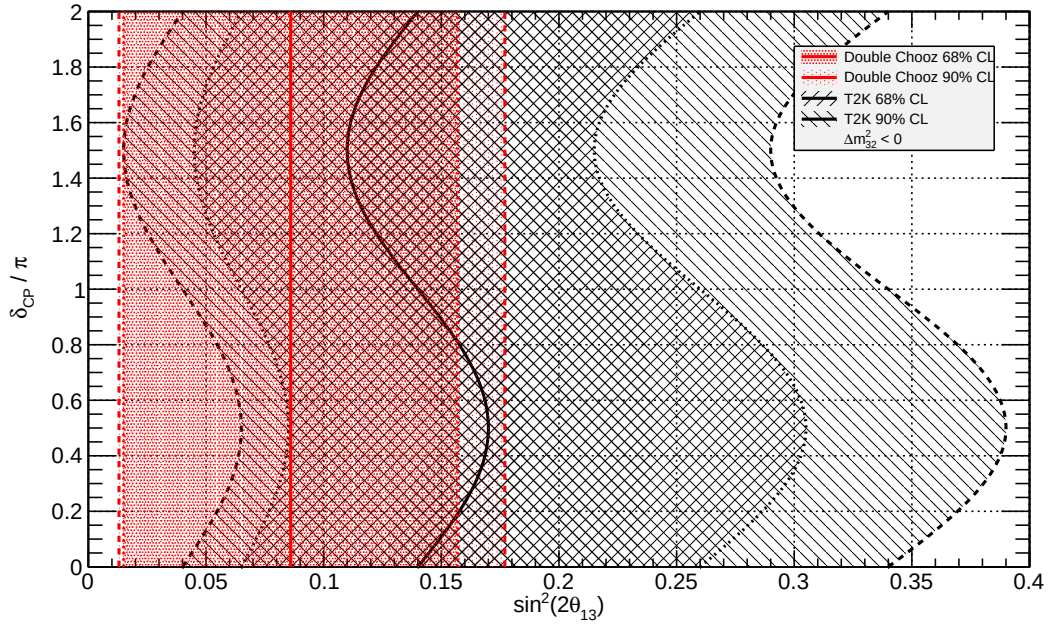

(b)

Figure 6.1: 68% (dotted) and 90% (dashed)[1] confidence sets and best fit line (solid) of the DC and T2K experiment. Double Chooz is depicted in red [8, p. 5] and T2K in black [7, p. 7]. All graphs are reproduced approximatively from the respective publications. Figure (a) shows normal neutrino mass hierarchy, figure (b) inverted hierarchy.

A possible joint analysis method is given by considering the measurement of both experiments as a single experiment. This experiment adds up the 18 energy bins of DC and the one energy bin of T2K to a 19 energy bin combined experiment. The enlarged experiment has then a 19×19 covariance matrix similar to the official Double Chooz analysis. This matrix can be added up from several covariance matrices, as done in the Double Chooz analysis. Assuming that DC and T2K are uncorrelated, this matrix would decompose into a block diagonal matrix with two submatrices. However, small correlations between the experiments are given, since e.g. neutrino cross sections are considered in both analyses. Thus, the covariance matrix is not a pure block diagonal matrix. Furthermore, the experiments use the same oscillation parameters and are located in a similar $\frac{L}{E}$ region, as visible in figure 2.2. Hence, additional correlations are present. The covariance matrix can be gained like in the DC analysis framework in MultiSims, where for the first bins the DC equations have to be used and for the 19^{th} bin the T2K equations have to be used. The same random shifts have to be used for the common parameters in both sets of equations to account for the correlation correctly.

As in the official analyses, parameters that a drawn to be out of the physical region have to be handled specially. Instead of the standard methods of the DC and T2K analyses, the alternative method developed in section 4.3 can be used. An a posteriori comparison of the different methods could give information on the uncertainty introduced by the physical boundary issue.

After the computation of the covariance matrix, a χ^2 minimisation can be used to determine the δ_{CP}–$\sin^2(2\theta_{13})$ tuple that explains the measured number of events of both experiments best. This is analogue to the DC method. The simple T2K method of optimising the parameter set cannot be used any more, since more than one energy class has to be considered in the joint analysis. The χ^2 statistic in this fit is analog to the DC covariance approach χ^2 statistic (cf. equation 5.1), but with the new 19×19 covariance matrix instead. This has to be performed assuming normal and inverted neutrino mass hierarchy, respectively.

The confidence set computation is performed on a grid in the δ_{CP}–$\sin^2(2\theta_{13})$ parameter space plane. At each point, a MultiSim of the neutrino events in each bin is performed. This is similar to the T2K approach. Nevertheless, the MultiSim has to adopt the DC method as it has to deal with correlated random draws from the covariance matrix. The 18 DC bins are in fact unaffected by the value of δ_{CP}. Nevertheless, the full simulation has to be performed at every grid point, since some of the parameters of both experiments can turn out to be significantly correlated. After performing the MultiSim at a parameter space grid point, a confidence set at this point can be gained from the produced ensemble of pseudo experiments. For this, the ordering principle of Feldman-Cousins can be utilised. A $\Delta\chi^2$ criterion as used in the Double Chooz analysis has to be used for the joint experiment, as a multi-bin measurement is present. This criterion reads as

$$\Delta\chi^2(n|\theta_{13}^{assu}, \delta_{CP}^{assu}) = \chi^2(n|\theta_{13}^{assu}, \delta_{CP}^{assu}) - \chi^2(n|\theta_{13}^{best}, \delta_{CP}^{best}) \tag{6.1}$$

This means that for each pseudo experiment the χ^2 under the condition of the assumed parameter tuple $(\theta_{13}^{assu}, \delta_{CP}^{assu})$ and the χ^2 of the tuple with highest likelihood $(\theta_{13}^{best}, \delta_{CP}^{best})$ has to be computed. The last χ^2 computation coincides with the χ^2 minimisation for the best point estimate method. The T2K analysis used a so called raster scan to find the physical boundaries for $\sin^2(\theta_{13})$ for each fixed value of δ_{CP}. This means that only θ_{13} was optimised, while δ_{CP}^{best} is replaced by the fixed δ_{CP}^{assu} (cf. equation 5.25). This was done since the T2K

experiment has no sensitivity on δ_{CP}. The joint experiment has sensitivity on δ_{CP}, thus a global scan has to be done. This means, the ordering principle of Feldman-Cousins is given precisely as equation 6.1. Evaluating equation 6.1 for every pseudo experiment performed at a certain parameter space grid point $(\theta_{13}^{assu}, \delta_{CP}^{assu})$ yields a distribution of $\Delta\chi^2(n|\theta_{13}^{assu}, \delta_{CP}^{assu})$. From this distribution, a critical $\Delta\chi^2(\theta_{13}^{assu}, \delta_{CP}^{assu})$ can be computed as

$$\Delta\chi^2_{crit}(\theta_{13}^{assu}, \delta_{CP}^{assu}) = \min_{\{\widetilde{c}\in\mathbb{R}:\#\{n|\Delta\chi^2(n|\theta_{13}^{assu},\delta_{CP}^{assu})\leq\widetilde{c}\}\geq 1-\alpha\}} \widetilde{c}. \tag{6.2}$$

in analogy to equation 5.17. Equation 6.2 therefore defines the value that separates the worst α pseudo experiments (with respect to their $\Delta\chi^2$) from the best $1-\alpha$. Now, for the real data the $\Delta\chi^2(n_{meas}|\theta_{13}^{assu}, \delta_{CP}^{assu})$ has to be computed at every parameter grid point. The final confidence set is then rendered as the set of all grid points where this value is less or equal to the critical value. Hence, the final set is given as

$$C(n_{meas}) = \left\{(\theta_{13}^{assu}, \delta_{CP}^{assu})|\Delta\chi^2(n_{meas}|\theta_{13}^{assu}, \delta_{CP}^{assu}) \leq \Delta\chi^2_{crit}(\theta_{13}^{assu}, \delta_{CP}^{assu})\right\}. \tag{6.3}$$

The usage of this criterion avoids issues discussed in section 5.1.8. If the set reaches a physical boundary, the remarks in paragraph 4.4.2.1.3 have to be considered. However, this can only happen with respect to θ_{13}, since the parameter space for δ_{CP} is periodical (cf. equation 2.12). This analysis has to be performed under the assumption of normal and inverted hierarchy. As the confidence sets of both experiments are similar for normal and inverted hierarchy, it is nevertheless possible to exclude some values of δ_{CP} in both hierarchy scenarios. By this, a hierarchy independent confidence set for δ_{CP} might be established.

6.2 Statistical Method for a Mass Hierarchy Measurement

Apart from δ_{CP}, it is further possible to infer to some extend on the neutrino mass hierarchy. For a fixed δ_{CP}, a similar method to the one in section 6.1 can in principle be used for this purpose. Problematic is the fact that only two neutrino mass hierarchies exist. Hence, the discrete set of neutrino mass hierarchies is likely too coarse for a numerical method as the above, thus it is likely to always get the trivial confidence set regardless of the δ_{CP}.

Alternatively, the neutrino mass hierarchy can be addressed with a different method. On the one hand, it is possible to test how likely it is that the gained best fit parameter tuple $(\theta_{13}, \delta_{CP})$ from section 6.1 assuming **n**ormal **h**ierarchy (NH) really proves NH. This is also possible for **i**nverted **h**ierarchy (IH). On the other hand, a test on the likelihood of the complete parameter set $(H, \theta_{13}, \delta_{CP})$ is possible. Herein, H stands for the hierarchy. Let for the rest of this chapter $(\theta_{13}^{NH}, \delta_{CP}^{NH})$ denote the best fit parameters in the NH scenario and $(\theta_{13}^{IH}, \delta_{CP}^{IH})$ denote the best fit parameters in the IH scenario. Both questions can be addressed with a likelihood ratio test (cf. appendix B).

6.2.1 Test on the hierarchy assuming a best fit parameter tuple

In the first case, we choose the parameter tuple $(\theta_{13}^{NH}, \delta_{CP}^{NH})$ and generate an ensemble of pseudo experiments additionally assuming NH and a second ensemble of pseudo experiments additionally assuming IH. In principle the ensembles generated in section 6.1 can be reused. A common random variable, which can be compared without assuming a certain hierarchy scenario, is needed for the implementation of the test. Such a variable is for example the best

fit parameter tuple $(\theta_{13}^{best}(n), \delta_{CP}^{best}(n))$. For each pseudo experiment n, the best fit parameter tuple is determined as for the real data. This was also done in section 6.1 and the result can again be reused. By this, two distributions of parameter tuples are rendered. It is now possible to address the question: "How significant does the parameter set $(\theta_{13}^{NH}, \delta_{CP}^{NH})$ prove that NH is the true hierarchy?" For this, the likelihood ratio

$$\Lambda_{NH}((\theta_{13}, \delta_{CP})) := \frac{\mathcal{L}(NH|(\theta_{13}, \delta_{CP}), \theta_{13}^{NH}, \delta_{CP}^{NH})}{\sup_{\eta\in\{NH,IH\}} \mathcal{L}(\eta|(\theta_{13}, \delta_{CP}), \theta_{13}^{NH}, \delta_{CP}^{NH})} \tag{6.4}$$

has to be considered. This is the standard likelihood ratio of a likelihood ratio test. The likelihood function $\mathcal{L}$ can be computed from the pseudo experiment ensembles. Additionally, the probability function of $\Lambda((\theta_{13}, \delta_{CP}))$ can be computed from the ensembles. Now

$$P_{NH}(\Lambda_{NH}((\theta_{13}, \delta_{CP})) < \Lambda_{NH}((\theta_{13}^{NH}, \delta_{CP}^{NH}))) \tag{6.5}$$

is the requested significance[2]. If this would turn out to be sufficiently insignificant, the NH scenario can be rejected. Similarly the IH scenario can be rejected by repeating the above test with IH instead of NH.

6.2.2 Test on the entire parameter set

In the second case, the question to address is: "How significant does the measured oscillation probability of the T2K experiment prove that $(NH, \theta_{13}^{NH}, \delta_{CP}^{NH})$ is the true parameter set?" Analog to the above test, two pseudo experiment ensembles have to be generated. The first ensemble is generated assuming $(NH, \theta_{13}^{NH}, \delta_{CP}^{NH})$ and the second ensemble is generated assuming $(IH, \theta_{13}^{IH}, \delta_{CP}^{IH})$. For each ensemble, the electron neutrino appearance probability has to be calculated. This is the same probability that was measured by the T2K experiment. This probability is measurable without assuming a certain hierarchy scenario, thus very sufficient for the purposes of this test. Although the pseudo experiments are generated for the joint experiment, only the T2K relevant probability is chosen as random variable. This is due to the fact that the DC oscillation probability, i.e. the electron antineutrino survival probability, is nearly unaffected by the mass hierarchy. This was visualised in figure 2.3b. Similar to the likelihood ratio 6.4 in the above test, the likelihood ratio in this test is defined as

$$\Lambda_{NH}(P_{osc}) := \frac{\mathcal{L}((NH, \theta_{13}^{NH}, \delta_{CP}^{NH})|P_{osc})}{\sup_{\eta\in\{NH,IH\}} \mathcal{L}((\eta, \theta_{13}^{\eta}, \delta_{CP}^{\eta})|P_{osc})} \tag{6.6}$$

and the requested significance is

$$P_{NH}(\Lambda_{NH}(P_{osc}) < \Lambda_{NH}(P_{osc}^{T2K})), \tag{6.7}$$

where P_{osc}^{T2K} is the electron neutrino appearance probability measured in the real T2K experiment. A low significance in this test allows to reject the NH scenario. Similar the IH scenario can be investigated by replacing NH by IH in the above equations. This test checks in principle if one of the P_{osc} distribution is very flat compared to the other distribution, since both distributions are centered around P_{osc}^{T2K}. The likelihood functions can again be computed from the ensemble distributions.

[2]While θ_{13}^{NH} and δ_{CP}^{NH} were parameters of the model in equation 6.4, they are to be understood as the measured data in equation 6.5. In the notation of appendix B is holds that $\Psi = z^{\star}$.

6.3 Combined Analysis with Imperfect Information

Apart from the Double Chooz and T2K experiments, further experiments have recently measured or constrained θ_{13} or a combination of θ_{13}, δ_{CP}, the neutrino mass hierarchy and other oscillation parameters [9; 10; 73]. Their results are summarised in appendix C. The statistical method described in section 6.1 can be utilised to incorporate those experiments by simply expanding the number of analysis bins in the above described manner. However, the method of section 6.1 obtains its major advantage from the detailed information of the individual uncertainty treatments and statistical methods utilised in the experiments. This allows a unification of all considered experiments to a joint experiment. Moreover, a unified simulation and evaluation of this joint experiment allows correlations between the experiments to enter the simulation in an early stage. Since this information is not necessary available for all the experiments listed in table C.1 or will not necessarily be for future experiments, a method for a combined analysis with imperfect information is needed.

Necessary for this is more information than normally provided in a common publication. The minimum data set includes the expected number of events at each parameter space point; furthermore, the number of data events is needed. The expected numbers have to be provided in every bin considered in the individual analyses. Additionally, the covariance matrix is needed. From this information, it is possible to construct a combined covariance matrix by adding up the existing matrices to a block diagonal matrix. Using this matrix, an analysis similar to the one described in section 6.1 is realisable. However, this method suffers from unsimulated correlations between experiments, since the covariance matrix in its representation as block diagonal matrix considers only experiment-internal correlations. Moreover, it is not possible to correct for possible compound measurands, e.g. $2\sin^2(2\theta_{13})\sin^2(\theta_{23})$ in the case of MINOS, and for different assumptions in the oscillation parameters, cross sections &c.

Chapter 7

Conclusion and Outlook

Aiming for the development of measurement strategies for δ_{CP} and the neutrino mass hierarchy, the analysis methods of the reactor experiment Double Chooz and the accelerator experiment T2K were investigated thoroughly. The statistical methods for the computation of best point estimates and confidence sets of both experiments were analysed. Furthermore, the underlying mathematical concepts of these methods were examined. Issues in these methods and in the implementation of these methods in the individual experiment analyses were pointed out and improvements suggested. Utilising the distinct dependencies on the oscillation parameters of both experiments, a joint analysis strategy with sensitivity on the aimed-at parameter δ_{CP} was pointed out. The joint analysis method takes up the statistical analyses of the Double Chooz and the T2K experiment. Modifications of these individual analyses, which are necessary for a joint analysis, were pointed out and discussed. It was shown that the joint analysis is capable to incorporate experiment-internal and cross-experiment correlations to a high degree. Moreover, statistical tests for the probing of the neutrino mass hierarchy were developed. These tests use the results of the joint analysis.

Finally, it was shown that the developed joint analysis can incorporate further experiments. This is also possible even if not the entire individual analysis method is known, though less powerful. Such incorporations can be made with current experiments like the MINOS experiment as an accelerator experiment on the one hand and Daya Bay and RENO as reactor experiments on the other hand. In addition, future experiments will be combineable.

Appendices

A Additional Proofs Concerning the Feldman-Cousins Approach

Lemma: (A.1)

Using the notation in subsection 4.4.2.1 and assuming that $\zeta \sim N(\mu, \sigma^2)$ or $\zeta \sim Pois(\mu)$ it holds that

$$C_{FC}(\zeta_{meas}) \neq \emptyset \quad \forall \zeta_{meas} \in \mathbb{R} \tag{A.2}$$

PROOF:
The proposition holds if

$$\forall \zeta_{meas} \in \mathbb{R} \quad \exists \zeta_{assu} \text{ such that } \zeta_{meas} \in c_{FC}(\zeta_{assu}) \tag{A.3}$$

by definition of c_{FC} or equivalently iff

$$\forall \zeta_{meas} \quad \exists \zeta_{assu} \text{ such that } \forall \zeta : \; R(\zeta_{meas}|\zeta_{assu}) \geq R(\zeta|\zeta_{assu}) \tag{A.4}$$

Case 1: $\zeta_{meas} \in Z_{p.a.}$
Claim: $\zeta_{assu} = \zeta_{meas}$
Clearly $R(\zeta_{meas}|\zeta_{assu}) = 1$ if $\zeta_{assu} = \zeta_{meas}$
Case a: $\zeta \sim Pois(\mu)$. To show:

$$\forall \zeta : \; 1 \geq R(\zeta|\zeta_{meas}) \tag{A.5}$$

$$\Leftrightarrow \forall \zeta : \; \frac{\frac{(\zeta_{meas})^{\zeta}}{\zeta!} \exp(-\zeta_{meas})}{\frac{(\zeta)^{\zeta}}{\zeta!} \exp(-\zeta)} \leq 1 \tag{A.6}$$

$$\Leftrightarrow \forall \zeta : \; \left(\frac{\zeta_{meas}}{\zeta}\right)^{\zeta} \exp(\zeta - \zeta_{meas}) \leq 1 \tag{A.7}$$

This inequality is easily to verify by elementary derivation.
Case b: $\zeta \sim N(\mu, \sigma^2)$
Again it holds that $R(\zeta_{meas}|\zeta_{assu}) = 1$ if $\zeta_{assu} = \zeta_{meas}$
Moreover, it generally follows that

$$p(\zeta_1|\zeta_{best}) = p(\zeta_1|\zeta_1) = p(\zeta_2|\zeta_2) \; \forall \zeta_1, \zeta_2 \in Z_{p.a.} \tag{A.8}$$

and

$$p(\zeta_1|\zeta_1) \geq p(\zeta_2|\zeta_1) \; \forall \zeta_2 \neq \zeta_1 \tag{A.9}$$

from the definition of the probability density functions. Again, it is to show that

$$\forall \zeta : \; R(\zeta_{meas}|\zeta_{meas}) \geq R(\zeta|\zeta_{meas}) \tag{A.10}$$

$$\Leftrightarrow \forall \zeta : \; \frac{p(\zeta_{meas}|\zeta_{meas})}{p(\zeta_{meas}|\zeta_{meas})} \geq \frac{p(\zeta|\zeta_{meas})}{p(\zeta|\zeta)} \tag{A.11}$$

$$\overset{A.8}{\Leftrightarrow} \forall \zeta : \; p(\zeta_{meas}|\zeta_{meas}) \geq p(\zeta|\zeta_{meas}) \tag{A.12}$$

$$\Leftrightarrow A.9 \tag{A.13}$$

Case 2: $\zeta_{meas} \notin Z_{p.a.}$
W.l.o.g. assume that $Z_{p.a.} = [\zeta_{lim}; \infty)$. The case is obviously proven if a ζ^* exist such that

$$\forall \zeta : \; R(\zeta_{meas}|\zeta^*) \geq R(\zeta|\zeta^*) \tag{A.14}$$

Claim: $\zeta_* = \zeta_{lim}$
For $\zeta \notin [\zeta_{lim}; \infty)$ it obviously holds that

$$\zeta_{best} = \zeta_{lim} \tag{A.15}$$

as the probability density functions have their only maximum at their respective medians. It is to show that

$$\forall \zeta : \; R(\zeta_{meas}|\zeta_{lim}) \geq R(\zeta|\zeta_{lim}) \tag{A.16}$$

$$\overset{A.15}{\underset{A.8}{\Leftrightarrow}} \forall \zeta \in Z_{p.a.} : \; \frac{p(\zeta_{meas}|\zeta_{lim})}{p(\zeta_{meas}|\zeta_{lim})} \geq \frac{p(\zeta|\zeta_{lim})}{p(\zeta|\zeta)} \wedge \forall \zeta \notin Z_{p.a.} : \; \frac{p(\zeta_{meas}|\zeta_{lim})}{p(\zeta_{meas}|\zeta_{lim})} \geq \frac{p(\zeta|\zeta_{lim})}{p(\zeta|\zeta_{lim})} \tag{A.17}$$

$$\Leftrightarrow \forall \zeta \in Z_{p.a.} : \; 1 \geq \frac{p(\zeta|\zeta_{lim})}{p(\zeta|\zeta)} \tag{A.18}$$

$$\Leftrightarrow A.9 \tag{A.19}$$

□

B The Likelihood Ratio Test

The likelihood-ratio test is a hypothesis test. Its purpose is the test of a hypothesis H_0 of the type

$$H_0 : \eta \in \Upsilon_0 \tag{B.1}$$

against

$$H_1 : \eta \in \Upsilon_1, \tag{B.2}$$

where $\Upsilon_0 \dot{\cup} \Upsilon_1 = \Upsilon$ are parameter sets. This hypothesis is tested under consideration of a given realisation

$$z^\star = (x_1, x_2, ..., x_n) \tag{B.3}$$

of $n \in \mathbb{N}$ realisations x_i $1 \leq i \leq n$ of an n-dimensional random variable

$$Z = (X_1, X_2, ..., X_n) \tag{B.4}$$

with n random variables X_i, $1 \leq i \leq n$. The distributions of these random variables depend on an element of the parameter set Υ and possibly additionally fixed parameters

$\Psi = \{\psi_1, ..., \psi_m\}$, with $m \in \mathbb{N}$. The test itself gives a statement about which of the parameters or which subset of Υ is the likeliest considering the given realisation $z^\star$. If $f^Z(z|\eta, \Psi)$ denotes the density function of Z, then let

$$\mathcal{L}^Z(\eta|z, \Psi) = f^Z(z|\eta, \Psi) \tag{B.5}$$

denote the likelihood function of η. Now consider the likelihood-ratio test statistic

$$\Lambda(Z) = \frac{\sup_{\eta\in\Upsilon_0} \mathcal{L}^Z(\eta|Z, \Psi)}{\sup_{\eta\in\Upsilon} \mathcal{L}^Z(\eta|Z, \Psi)}. \tag{B.6}$$

It compares the likelihood of the tested parameter set with the entire parameter set and can be understood as the relative likelihood. It exist a critical value λ_{crit} for which

$$\alpha = \sup_{\eta\in\Upsilon_0} P(\Lambda(Z) < \lambda_{crit}|\eta) \tag{B.7}$$

holds.

Given the realisation $z^\star$, the hypothesis H_0 would be rejected if the corresponding likelihood ratio

$$\Lambda(z^\star) = \frac{\sup_{\eta\in\Upsilon_0} \mathcal{L}^Z(\eta|z^\star, \Psi)}{\sup_{\eta\in\Upsilon} \mathcal{L}^Z(\eta|z^\star, \Psi)} \tag{B.8}$$

yields a too low significance

$$\alpha = \alpha(z^\star) = \sup_{\eta\in\Upsilon_0} P(\Lambda(Z) < \Lambda(z^\star)|\eta). \tag{B.9}$$

In the case of section 6.2, the parameter sets are one-element sets containing the unit and its inverse:

$$\Upsilon = \{+1; -1\}. \tag{B.10}$$

These are the possible signs of Δm^2_{32}. For convenience reasons Υ is denoted as $\{NH; IH\}$ in section 6.2. The n-dimensional realisation $z^\star$ in both tests is given as the tuple $(\theta^{NH}_{13}, \delta^{NH}_{CP})$ and P^{T2K}_{osc}, respectively.

For a more thorough introduction in the topic of likelihood ratio tests cf. [52, p. 580] and [59, p. 291].

C Comparison of Recent Neutrino Experiment Results

	normal hierarchy			inverted hierarchy[1]			
	left	centre	right	left	centre	right	
Daya Bay	0.071	0.092	0.113				[10]
RENO	0.081	0.113	0.145				[9]
Double Chooz	0.015	0.086	0.157				[8]
T2K[2]	0.05	0.11	0.21	0.07	0.14	0.26	[72]
MINOS[2,3]	0.010	0.041	0.088	0.026	0.079	0.150	[73]

[1] for reactor experiments same as normal hierarchy
[2] for $\delta_{CP} = 0$
[3] for $2\sin^2(\theta_{23}) = 1$

Table C.1: 68% confidence sets of all neutrino experiments sensitive on θ_{13} that have published their results between January 2011 and July 2012.

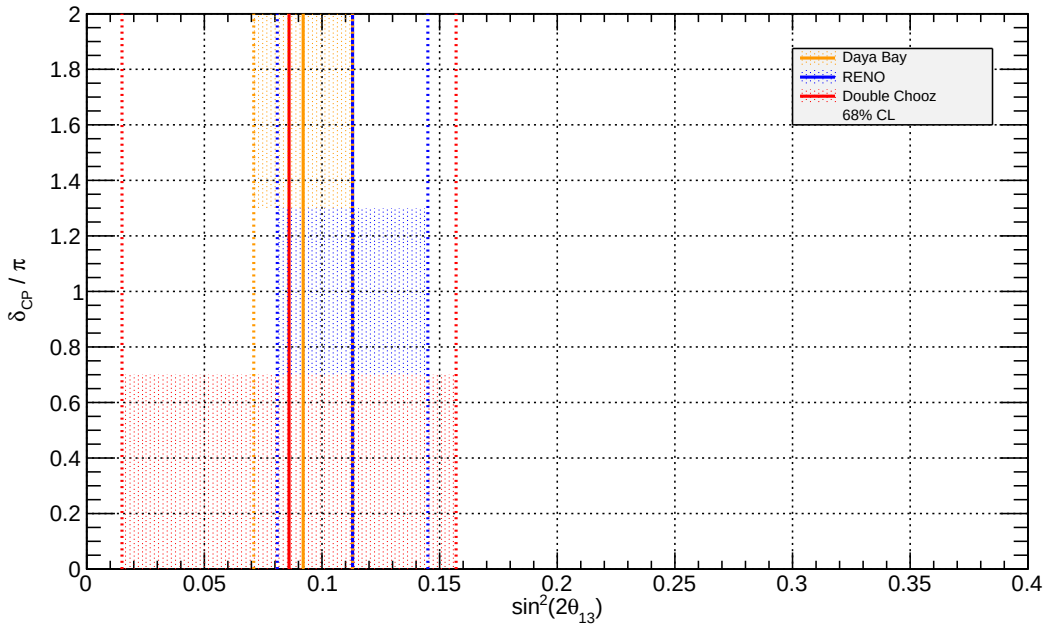

Figure C.1: Extract from figure C.2. See there for explanation.

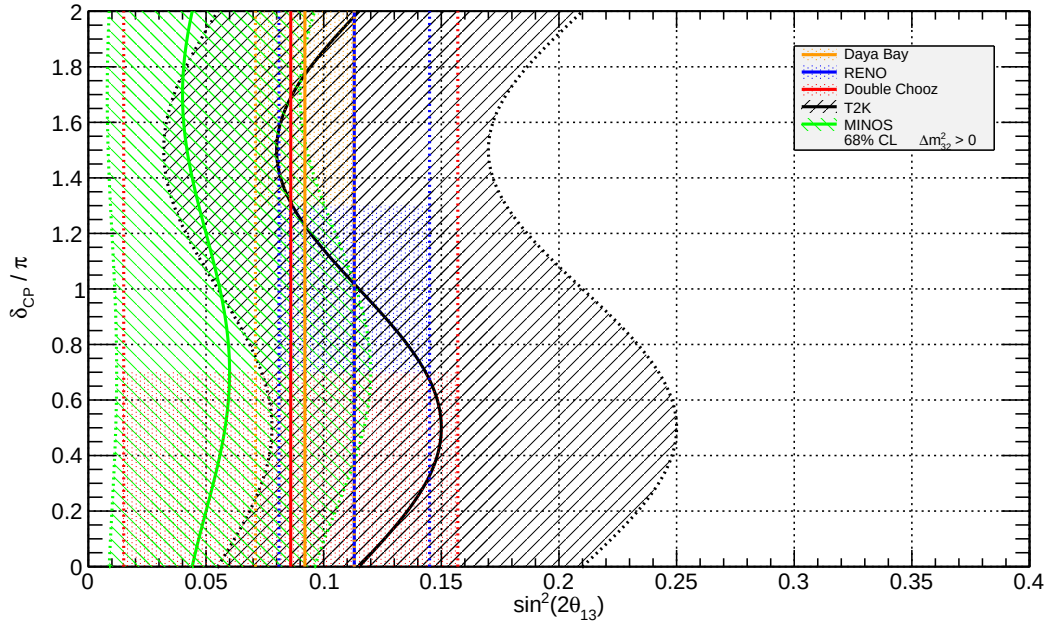

(a)

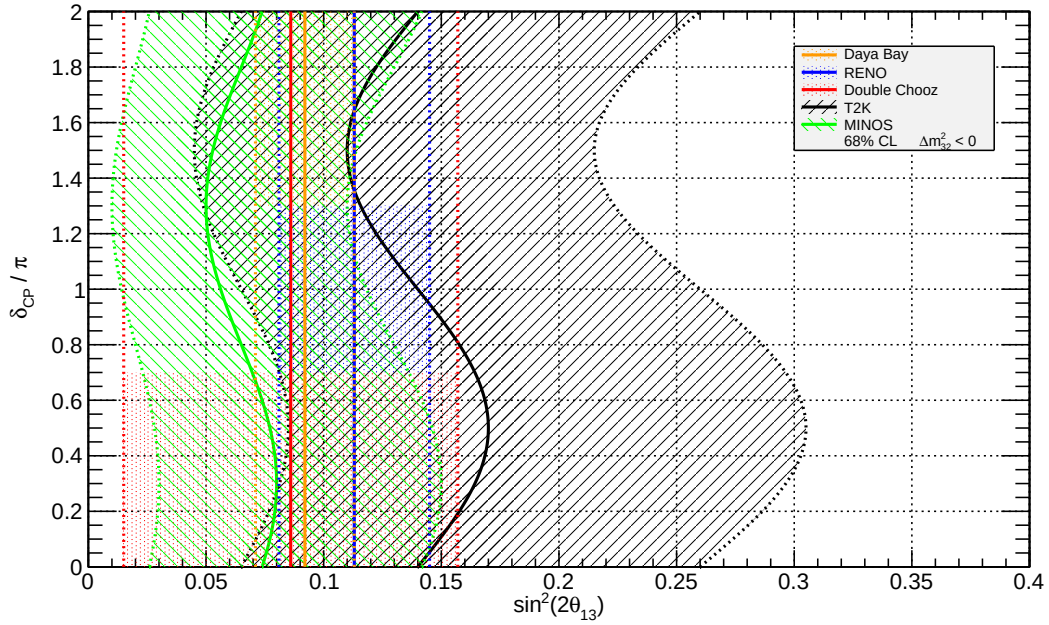

(b)

Figure C.2: 68% confidence sets for (a) normal and (b) inverted hierarchy of T2K (black), Double Chooz (red), RENO (blue), Daya Bay (orange) and MINOS (green). The solid lines refer to the respective best fit values. All graphs are reproduced approximatively from the respective publications. Values and annotations cf. table C.1.

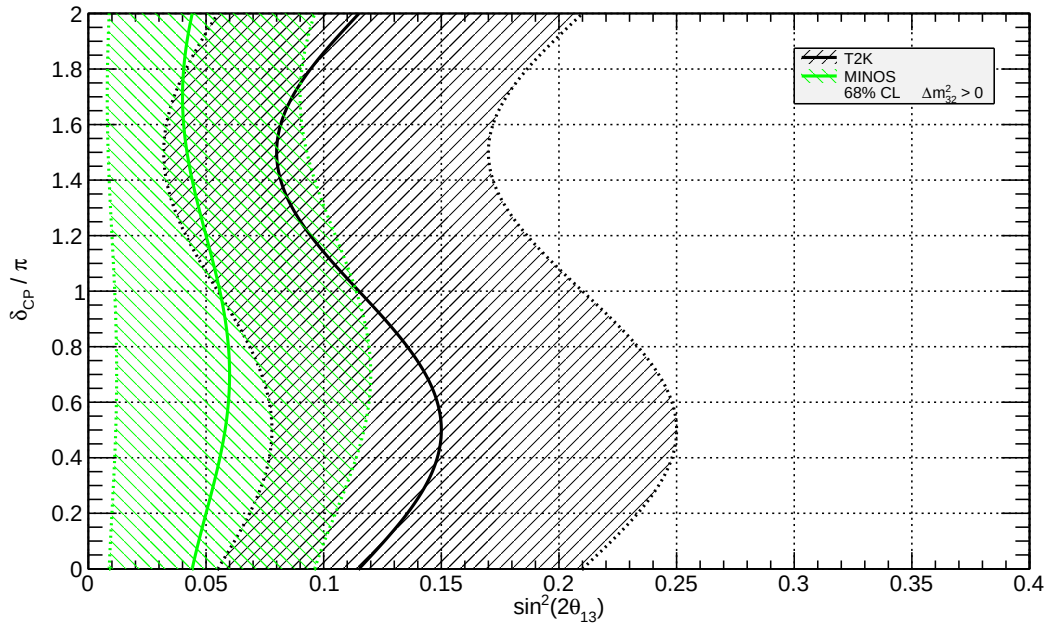

(a)

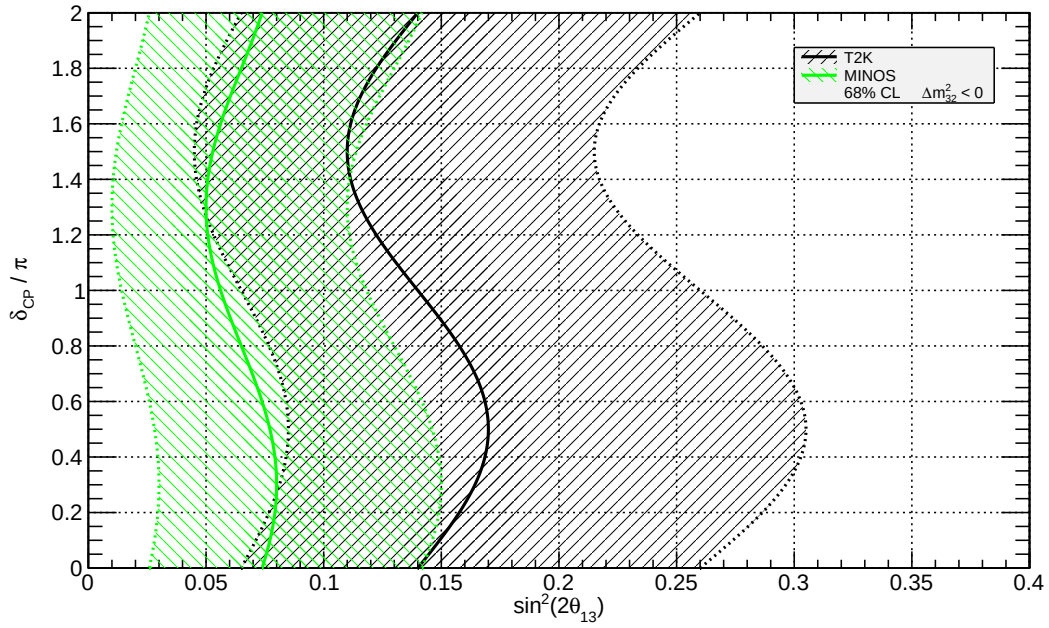

(b)

Figure C.3: Extract from figure C.2. See there for explanation.

Glossary

AGS: **A**lternating **G**radient **S**ynchrotron
CCQE: **c**harged **c**urrent **q**uasi **e**lastic
cdf: **c**ummulative **d**ensity **f**unction
C.L.: **c**onfidence **l**evel
Co: **co**balt
Cs: **c**ea**s**um
CT: **C**ommon **T**runk
DC: **D**ouble **C**hooz
DOGS: **D**ouble Chooz **O**ffline **G**roup **S**oftware
ECal: **e**lectromagnetic **cal**orimeters
EDF: **É**lectricité **d**e **F**rance
FC: **F**eldman-**C**ousins
FD: **F**ar **D**etector
FGD: **f**ine **g**rained **d**etectors
GC: γ-**C**atcher
GLG4sim: "**G**eneric**L**AND" **G**eant**4** **sim**ulation
ID: **I**nner **D**etector
IH: **i**nverted neutrino mass **h**ierarchy
INGRID: **i**nteractive **n**eutrino **grid**
IV: **I**nner **V**eto
J-PARC: **J**apan **P**roton **A**ccelerator **R**esearch **C**omplex
LAND: **L**iquid-scintillator **A**nti-**N**eutrino **D**etector
LEP: **L**arge **E**lectron-**P**ositron Collider
MC: **M**onte **C**arlo
MultiSim: **multi**ple **sim**ulation
m.w.e.: **m**eter **w**ater **e**quivalent
ND: **N**ear **D**etector
ND280: T2K off-axis **N**ear **D**etector **280** meter
n.d.f.: **n**umber of **d**egrees of **f**reedom
NT: **N**eutrino **T**arget
OD: **O**uter **D**etector
OV: **O**uter **V**eto
P0D: π^0 **d**etector
p.a.: **p**hysically **a**llowed
PE: **p**hoto **e**lectron
pdf: **p**robability **d**ensity **f**unction
pmf: **p**robability **m**ass **f**unction

PMNS: Pontecorvo-**M**aki-**N**akagawa-**S**akata-Matrix
PMT: Photo**m**ultiplier **t**ubes
POD: cf. P0D
RoSS: Read**o**ut **S**imulation **S**oftware
NH: normal neutrino mass **h**ierarchy
SK: Super-**K**amikoande detector
SMRD: side **m**uon **r**ange **d**etector
T2K: Tokai-**to**-**K**amioka experiment
TPC: time **p**rojection **c**hambers
UA1: Underground **A**rea **1**

List of Figures

List of Tables

References

[1] Y. Ashie et al. (Super-Kamiokande Collaboration), Measurement of atmospheric neutrino oscillation parameters by Super-Kamiokande I, *Physical Review D* **71**(11): 112005 (2005).

[2] M. H. Ahn et al. (K2K Collaboration), Measurement of neutrino oscillation by the K2K experiment, *Physical Review D* **74**(7): 072003 (2006).

[3] S. Abe et al. (The KamLAND Collaboration), Precision Measurement of Neutrino Oscillation Parameters with KamLAND, *Physical Review Letters* **100**(22): 221803 (2008).

[4] M. Altmann et al. (GNO Collaboration), Complete results for five years of GNO solar neutrino observations, *Physics Letters B* **616**(3–4): 174–190 (2005).

[5] Q. R. Ahmad et al. (SNO Collaboration), Direct Evidence for Neutrino Flavor Transformation from Neutral-Current Interactions in the Sudbury Neutrino Observatory, *Physical Review Letters* **89**(1): 011301 (2002).

[6] P. Adamson et al. (MINOS Collaboration), Measurement of Neutrino Oscillations with the MINOS Detectors in the NuMI Beam, *Physical Review Letters* **101**(13): 131802 (2008).

[7] K. Abe et al. (T2K Collaboration), Indication of Electron Neutrino Appearance from an Accelerator-Produced Off-Axis Muon Neutrino Beam, *Physical Review Letters* **107**(4): 041801 (2011).

[8] Y. Abe et al. (Double Chooz Collaboration), Indication of Reactor $\bar{\nu}_e$ Disappearance in the Double Chooz Experiment, *Physical Review Letters* **108**(13): 131801 (2012).

[9] J. K. Ahn et al. (RENO Collaboration), Observation of Reactor Electron Antineutrinos Disappearance in the RENO Experiment, *Physical Review Letters* **108**(19): 191802 (2012).

[10] F. P. An et al. (The Daya Bay Collaboration), Observation of electron-antineutrino disappearance at Daya Bay, *arXiv:1203.1669v2* (2012).

[11] R. Halleux, J. Vandersmissen, A. Despy-Mayer and G. Vanpaemel, *Histoire des Sciences en Belgique, 1815-2000*, La Renaissance du Livre, Bruxelles, 2 edition, 2001, 109–121.

[12] C. L. Cowan Jr., F. Reines, F. B. Harrison, H. W. Kruse and A. D. McGuire, Detection of the Free Neutrino: a Confirmation, *SCIENCE* **124**: 103–104 (1956).

[13] K. Nakamura et al. (Particle Data Group), Review of Particle Physics, *Journal of Physics G: Nuclear and Particle Physics* **37**(7 A): 075021 (2010).

[14] G. Danby, J.-M. Gaillard, K. Goulianos, L. M. Lederman, N. Mistry, M. Schwartz and J. Steinberger, Observation of High-Energy Neutrino Reactions and the Existence of Two Kinds of Neutrinos, *Physical Review Letters* **9**(1): 36–44 (1962).

[15] K. Kodama et al. (DONUT Collaboration), Observation of tau neutrino interactions, *Physics Letters B* **504**: 218–224 (2001).

[16] B. Pontecorvo, *J. Exptl. Theoret. Phys.* **33**: 549 (1957).

[17] Z. Maki, M. Nakagawa and S. Sakata, Remarks on the Unified Model of Elementary Particles, *Progress of Theoretical Physics* **28**(5) (1962).

[18] S. Gasiorowicz, *quantum physics*, volume 1, John Wiley and Sons, Inc., 1974.

[19] D. H. Perkins, *Introduction to High Energy Physics*, volume 3, Addison-Wesley Publishing Company, Inc., 1987.

[20] J. A. Thomas and P. L. Vahle, editors, *Neutrino Oscillations - Present Status and Future Plans*, World Scientific Publishing, 2008.

[21] B. Reinhold, Development of a Level-1 Trigger and Timing System for the Double Chooz Neutrino Experiment, *PhD thesis*, Rheinisch-Westfälische Technische Hochschule Aachen, 2009.

[22] H. Nunokawa, S. Parke and J. W. F. Valle, CP Violation and Neutrino Oscillation, *arXiv:hep-ph/0710.0554v2* (2007).

[23] S.T. Petcov and M. Piai, The LMA MSW solution of the solar neutrino problem, inverted neutrino mass hierarchy and reactor neutrino experiments, *Physics Letters B* **533**(1–2): 94–106 (2002).

[24] O. Mena and S. Parke, Unified Graphical Summary of Neutrino Mixing Parameters, *Physical Review D* **69**(11): 117301 (2004).

[25] F. Ardellier et al., Double Chooz: A Search for the Neutrino Mixing Angle θ_{13}, *arXiv:hep-ex/0606025v4* (2006).

[26] Central Intelligence Agency, The World Factbook 2012, https://www.cia.gov/library/publications/the-world-factbook/index.html, 2012.

[27] M. Mezzetto and T. Schwetz, θ_{13}: phenomenology, present status and prospect, *Journal of Physics G: Nuclear and Particle Physics* **37**: 103001 (2010).

[28] F. Ardellier et al., Letter of Intent for Double-CHOOZ: a Search for the Mixing Angle θ_{13}, *arXiv:hep-ex/0405032v1* (2004).

[29] H. de Kerret, First results from the Double Chooz experiment, in *6th International Workshop on Low Energy Neutrino Physics*, 2011.

[30] C. Bauer et al., Qualification tests of 474 photomultiplier tubes for the inner detector of the Double Chooz experiment, *Journal of Instrumentation* **6**: P06008 (2011).

[31] S. Wagner, Ionization Quenching by Low Energy Electrons in the Double Chooz Scintillators, *Master's thesis*, Ruprecht-Karls Universität Heidelberg – Max-Planck-Institut für Kernphysik, 2010.

[32] E. Blucher, L. L. Camilleri, E. Conover, M. Dierckxsens, A. Franke, C. Mariani, A. Norrick, M. Toups and L. A. Winslow, OV electronics and test, http://www.dchooz.org/DocDB/cgi-bin/private/DocumentDatabase, 2011, Double Chooz Document 1400-v3.

[33] Double Chooz Collaboration, Double Chooz Detector, http://www.dchooz.org/DocDB/cgi-bin/private/DocumentDatabase, 2009, Double Chooz Document 1041-v1.

[34] A. Cucoanes, Design Studies for the Double Chooz Trigger, *PhD thesis*, Rheinisch-Westfälische Technische Hochschule Aachen, 2009.

[35] P. Novella Garijo, Double Chooz: Searching for θ_{13} with reactor neutrinos, in *Rencontres de Moriond - Electroweak Interactions and Unified Theories*, 2011.

[36] I. Antcheva et al., ROOT – A C++ framework for petabyte data storage, statistical analysis and visualization, *Computer Physics Communications* **180**(12): 2499–2512 (2009).

[37] R. Brun and F. Rademakers, ROOT – An object oriented data analysis framework, *Nuclear Instruments and Methods in Physics Research A* **389**(1–2): 81–86 (1997).

[38] K. Amako et al., Geant4 developments and applications, *IEEE Transactions on Nuclear Science* **53**(1): 270–278 (2006).

[39] S. Dazeley et al., Generic Liquid-scintillator Anti-Neutrino Detector (GenericLAND) Geant4 simulation, http://neutrino.phys.ksu.edu/~GLG4sim/.

[40] K. Abe et al. (The T2K Collaboration), The T2K Experiment, *arXiv:1106.1238v2* (2011).

[41] The T2K Collaboration - The Public Website Committee, The T2K Experiment, http://t2k-experiment.org/, 2011.

[42] Y. Itow et al., The JHF-Kamioka neutrino project, *arXiv:hep-ex/0106019v1* (2001).

[43] IOP Publishing, UA1 magnet sets off for a second new life, *CERN Courier* **48**(3) (2008).

[44] K. Amako et al., The Super-Kamiokande detector, *Nuclear Instruments and Methods in Physics Research A* **501**(2–3): 418–462 (2003).

[45] A. Ferrari, P.R. Sala, A. Fassò and J. Ranft, FLUKA: a multi-particle transport code, CERN-2005-10 (2005), INFN/TC_05/11, SLAC-R-773, 2005.

[46] R. Brun, F. Bruyant, M. Maire, A. C. McPherson and P. Zanarini, GEANT 3, CERN DD/EE/84-1, 1987.

[47] C. Andreopoulos et al., The GENIE neutrino Monte Carlo generator, *Nuclear Instruments and Methods in Physics Research A* **614**(1): 87–104 (2010).

[48] Y. Hayato, A Neutrino Interaction Simulation Program Library NEUT, *Acta Physica Polonica B* **40**(9): 2477–2489 (2009).

[49] W. R. Pestman, *Mathematical Statistics - An Introduction*, Walter de Gruyter Textbook, 1998.

[50] S. Baker and R. D. Cousins, Clarification of the use of CHI-square and likelihood functions in fits to histograms, *Nuclear Instruments and Methods in Physics Research* **221**(2): 437–442 (1984).

[51] T. Hauschild and M. Jentschel, Comparison of maximum likelihood estimation and chi-square statistics applied to counting experiments, *Nuclear Instruments and Methods in Physics Research A* **457**(1–2): 384–401 (2001).

[52] M. Fisz, *Probability Theory and Mathematical Statistics*, volume 3, John Wiley & Sons, Inc., 1963.

[53] B. P. Roe, *Probability and Statistics in Experimental Physics*, volume 9, Springer-Verlag, 1992.

[54] F. James and M. Roos, Minuit – a system for function minimization and analysis of the parameter errors and correlation, *Computer Physics Communications* **10**(6): 343–367 (1975).

[55] R. Fletcher, A new approach to variable metric algorithms, *The Computer Journal* **13**(3): 317–322 (1970).

[56] R. Fletcher and M. J. D. Powell, A Rapidly Convergent Descent Method for Minimization, *The Computer Journal* **6**(2): 163–168 (1963).

[57] N. Metropolis and S. Ulam, The Monte Carlo Method, *Journal of the American Statistical Association* **44**(247): 335–341 (1949).

[58] K. E. Atkinson, *An Introduction to Numerical Analysis*, volume 10, John Wiley & Sons, 1989.

[59] Z. W. Birnbaum, *Introduction to Probability and Mathematical Statistics*, volume 1, Harper & Brothers, 1962.

[60] A. O'Hagan and T. Leonard, Bayes estimation subject to uncertainty about parameter constraints, *Biometrika* **63**(1): 201–203 (1976).

[61] G. J. Feldman and R. D. Cousins, Unified approach to the classical analysis of small signals, *Physical Review D* **57**(7): 3873–3889 (1998).

[62] J. Conrad, O. Botner, A. Hallgren and C. Pérez de los Heros, Including systematic uncertainties in confidence interval construction for Poisson statistics, *Physical Review D* **67**: 012002 (2003).

[63] J. Bouchez, Confidence belts on bounded parameters, *arXiv:hep-ex/0001036v1* (2000).

[64] Double Chooz Final Fit Group, The DC Final Fit: A Sensitivity Study Framework, http://www.dchooz.org/DocDB/cgi-bin/private/DocumentDatabase, 2012, Double Chooz Document 3519-v15.

[65] G. L. Fogli, E. Lisi, A. Marrone, D. Montanino and A. Palazzo, Getting the most from the statistical analysis of solar neutrino oscillations, *Physical Review D* **66**(5): 053010 (2002).

[66] I. Ostrovskiy, Finding the error on the energy scale and detector response and including it in the final fit, http://www.dchooz.org/DocDB/cgi-bin/private/DocumentDatabase, 2011, Double Chooz Document 3270-v1.

[67] G. Mention, Energy scale & basic ingredient checks, http://www.dchooz.org/DocDB/cgi-bin/private/DocumentDatabase, 2011, Double Chooz Document 3478-v1.

[68] A. J. Franke, D. Lhuillier, C. Mariani and M. Shaevitz, Event Generation & Uncertainty Propagation in DCRxtrTools using the Bugey4 Anchor Point, http://www.dchooz.org/DocDB/cgi-bin/private/DocumentDatabase, 2011, Double Chooz Document 3221-v3.

[69] Z. Djurcic and C. Jones, Initial Fission Rate Systematic Studies and Comments, http://www.dchooz.org/DocDB/cgi-bin/private/DocumentDatabase, 2011, Double Chooz Document 2303-v1.

[70] A. Onillon, First Core Fission Rate Error estimates of the reactor group, http://www.dchooz.org/DocDB/cgi-bin/private/DocumentDatabase, 2011, Double Chooz Document 3277-v1.

[71] A. Collin and A. Franke, Propagating Antineutrino Spectrum Uncertainties to Reconstructed Positron Energy, http://www.dchooz.org/DocDB/cgi-bin/private/DocumentDatabase, 2011, Double Chooz Document 3274-v2.

[72] J. Albert and K. Okumura, Updated ν oscillation analysis with RUN1+2 data, http://www.t2k.org/docs/technotes, 2011, T2K Technical Note 052-v1.1.

[73] P. Adamson et al. (MINOS Collaboration), Improved Search for Muon-Neutrino to Electron-Neutrino Oscillations in MINOS, *Physical Review Letters* **107**(18): 181802 (2011).

Acknowledgment

I would like to thank in the first place Prof. Dr. rer. nat. Erhard Cramer and Prof. Dr. rer. nat. Achim Stahl for their willingness to supervise me in this rather uncommon interdisciplinary thesis.

I would like to thank Dr. rer. nat. Stefan Roth and Prof. Dr. rer. nat. Christopher Wiebusch for their additional advisory.

Many thanks go to other members of the Aachen Double Chooz and T2K groups for answering many questions and participating in many fruitful discussions: Ruth Herbertz, Dipl.-Phys. Sebastian Lucht, Marcel Rosenthal BSc, Manuel Schuman BSc, Dipl.-Phys. Jochen Steinmann, Dipl.-Phys. Anselm Stüken and Dipl.-Phys. Dennis Terhorst.

I thank Matthew Toups PhD and Joshua Albert PhD for their expertise of the Double Chooz and T2K final analyses.

Further thanks and my apologies go to many other members of both collaborations whose help I am not aware of during the writing of these lines and I hence forgot to mention.

Special thanks go to my parents who, without hesitation, supported me during this second study.

Additional thanks go to my girlfriend Katja for supporting me in the non-academical troubles of this thesis.

I dedicate this thesis to my grandmother Luise Magdalene Beinke to whom mathematics always meant more than physics.

Danksagung

Ich möchte an erster Stelle Herrn Prof. Dr. rer. nat. Erhard Cramer und Herrn Prof. Dr. rer. nat. Achim Stahl für ihre Bereitschaft mich in dieser eher ungewöhnlichen interdisziplinären Diplomarbeit zu betreuen.

Ich danke Herrn Dr. rer. nat. Stefan Roth und Herrn Prof. Dr. rer. nat. Christopher Wiebusch für ihre zusätzliche Betreuung bei dieser Arbeit.

Zusätzlicher Dank geht an weitere Mitglieder der Aachener Double Chooz und T2K Arbeitsgruppen für die Beantwortung viele Fragen und die Teilnahme an vielen wertvollen Diskussionen: Ruth Herbertz, Dipl.-Phys. Sebastian Lucht, Marcel Rosenthal BSc, Manuel Schuman BSc, Dipl.-Phys. Jochen Steinmann, Dipl.-Phys. Anselm Stüken und Dipl.-Phys. Dennis Terhorst.

Ich danke Matthew Toups PhD und Joshua Albert PhD für ihre Expertisen zu den Double Chooz und T2K Analysen.

Weiterer Dank und meine Bitte um Verzeihung geht an viele weitere Mitglieder beider Kollaborationen, deren Hilfe ich mir während des Schreibens dieser Zeilen nicht bewusst bin und die ich daher vergaß zu erwähnen.

Besonderer Dank geht an meine Eltern, die mich ohne Zögern auch in diesem zweiten Studium unterstützt haben.

Meiner Freundin Katja danke ich für die Unterstützung bei allen nicht-akademischen Problemen dieser Diplomarbeit.

Ich widme diese Diplomarbeit meiner Großmutter Luise Magdalene Beinke, die mit Mathematik stets mehr anfangen konnte als mit Physik.

Erklärung:
Hiermit versichere ich gemäß §19 Abs. 5 DPO Mathematik, dass ich diese Diplomarbeit selbständig verfasst und keine anderen als die angegebenen Quellen und Hilfsmittel benutzt, sowie Zitate kenntlich gemacht habe.

Aachen, den 12. September 2012

Unterschrift